SYNTHESIS AND CHARACTERIZATION OF SPARK DISCHARGE GENERATED AEROSOL NANOPARTICLES, FOCUSING ON THEIR DEPOSITION ON VARIOUS SUBSTRATES

Nafsica Maria Mouti

School of Applied Mathematical and Physical Sciences

National Technical University of Athens

A thesis submitted for the degree of

Master of Science in Microsystems and Nanodevices

February 2022

ACKNOWLEDGEMENTS

LIST OF ABBREVIATIONS

ACC	Activated Carbon Cloth
BSF	Borosilicate filter
C	Capacitor
CPC	Condensation Particle Counter
DMA	Differential Mobility Analyzer
EDS	Energy Dispersive X-ray Spectroscopy
ENP	Engineered Nanoparticle
$\mathbf{F_{in}}$	Input Carrier Gas Flow Rate
FSP	Flame Spray Pyrolysis
NP	Nanoparticle
PP	Polypropylene
$\mathbf{R_{ch}}$	Charge Resistance
$\mathbf{R_{dis}}$	Discharge Resistance
SDG	Spark Discharge Generator
SEM	Scanning Electron Microscope
SERS	Surface-Enhanced Raman Scattering
SMPS	Scanning Mobility Particle Sizer
SPR	Surface Plasmon Resonance
SRR	Spark Repetition Rate (f)
TEM	Transmittance Electron Microscope
$\mathbf{V_d}$	Discharge Voltage
$\mathbf{V_{in}}$	Input Voltage

ΠΕΡΙΛΗΨΗ

Τα μεταλλικά νανοσωματίδια έχουν βρει πολλές χρήσεις την τελευταία δεκαετία σε διάφορους τομείς, όπως , η φωτονική, η κατάλυση, η ανανεώσιμη ενέργεια, η ηλεκτρονική, η ιατρική, ακόμη και τα καλλυντικά. Η περαιτέρω ανάπτυξη αυτών των εφαρμογών θα απαιτήσει ισχυρές τεχνολογίες σύνθεσης νανοσωματιδίων ικανές να παράγουν σημαντική ποσότητα υλικού με τα επιθυμητά χαρακτηριστικά. Οι τεχνολογίες που βασίζονται στο πλάσμα, όπως οι εκκενώσεις σπινθήρα, είναι ιδιαίτερα ελπιδοφόρες επειδή επιτρέπουν σημαντικές αυξήσεις στους ρυθμούς παραγωγής και μειώσεις κόστους. Ο έλεγχος αυτών των διαδικασιών, ωστόσο, παραμένει ένα δύσκολο έργο που χρειάζεται έρευνα, τόσο πειραματική όσο και θεωρητική. Η εκκένωση σπινθήρα ερευνάται διεξοδικά στην παρούσα εργασία. Ο πρωταρχικός στόχος είναι η κατανόηση της θεμελιώδους μηχανικής πίσω από τις εκκενώσεις σπινθήρα με μεταλλικά ηλεκτρόδια, που απέχουν μικρή απόσταση μεταξύ τους, σε ατμοσφαιρική πίεση. Στη συνέχεια, χρησιμοποιώντας τα αντίστοιχα πειραματικά δεδομένα, μελετάται ο αριθμός των νανοσωματιδίων που παράγονται, η κατανομή των μεγεθών τους και η εναπόθεσή τους σε ποικίλα υποστρώματα. Η παρούσα εργασία εξετάζει την επίδραση της μεταβολής πολλαπλών παραμέτρων στην παραγωγή σωματιδίων μέσω του Spark Discharge Generator (SDG). Επιπλέον, διερευνάται ο τρόπος με τον οποίο τα νανοσωματίδια αλληλεπιδρούν και εναποτίθενται σε ποικίλα ινώδη υποστρώματα. Τέλος, κάποιες από τις δομές υποστρώματος - σωματιδίων αξιολογούνται για πιθανές εφαρμογές για 3D ανίχνευση μακρομορίων μέσω Surface-enhanced Raman spectroscopy (SERS), για αντιβακτηριακή και για αντιική δράση.

ABSTRACT

Metallic nanoparticles have found several uses over the past decade in a variety of fields, including optics, photonics, catalysis, material manufacture, renewable energy, electronics, medicine, and even cosmetics. Further development of these applications will need robust nanoparticle synthesis technologies capable of producing a significant quantity of nanoparticles with the desired characteristics. Plasma-based technologies, such as spark and arc discharges, are particularly promising because they enable significant increases in production rates and cost reductions. Controlling these processes, however, remains a difficult task that needs research, both experimental and theoretical. Spark discharge is thoroughly researched in this thesis. The primary goal is to get a better understanding of the fundamental mechanics behind spark discharges between electrodes that are a small distance apart, at atmospheric pressure. Then, using the corresponding experimental data, the number of nanoparticles generated, their size distribution, and their deposition on diverse surfaces are studied. The current thesis examines the effect of varying several parameters on Spark Discharge Generation. Furthermore, the way nanoparticles interact with and deposit on various fibrous substrates is investigated. Finally, some of the particle-substrate structures are evaluated for potential applications for 3D molecule detection via Surface-enhanced Raman spectroscopy (SERS), for antibacterial and antiviral activity.

CONTENTS

1. INTRODUCTION

1.1 Aims and Objectives of the Present Work

- Understanding of how a Spark Discharge Generator works.
- Investigation of how fixed and control parameters affect nanoparticle (NP) production, in terms of concentration and size.
- Comparison between Cu, Au, Pt and Pd electrodes.
- Study of electrode erosion after spark.
- Characterization of size and morphology of the produced nanoparticles.
- Study of how nanoparticles (NPs) are deposited on various substrates.
- Possible applications of produced NPs on the different tested substrates (borosilicate microfiber filters, surgical masks).

1.2 What is Nanotechnology

Engineering and manipulating materials and devices in the nanoscale (dimensional range between 1 and 100 nm) is known as "*nanotechnology*." Research and development of architectures of systems, devices and materials with unique characteristics and functionalities due to their nanoscale components and dimensions are all part of nanotechnology[1]. Nanotechnology is the study of how to make, develop, characterize and use structures at the nanoscale level[2]. One, two, and three-dimensional materials, in macroscale, have all been created using this technology. There is a huge amount of current technological applications based on nanomaterials and nanotechnology. As a result, nanotechnology is by its very nature a multidisciplinary field. Engineers and nanoscientists alike have agreed that nanotechnology focuses on functional materials in the vast area of laboratory and industry applications. This includes the creation of nanoscale materials, the study of these materials' electronic and photonic properties, as well as the development of appropriate devices and circuits for these materials.

1.2.1 SIGNIFICANCE OF THE NANOSCALE

One nanometer is one billionth of a meter. To put this in perspective, a human hair's diameter is 100,000 nm. Human blood cells are between 7500 and 8700 nm in diameter [1]; DNA is 2.5 nm in diameter [2]; and 10 hydrogen atoms in a line span 1 nm in length [3]. For the first time, scientists have the capability to comprehend and arrange matter down to the nanoscale level, allowing them to manipulate life and matter at their most fundamental levels.

---

[1] The National Nanotechnology Initiative at Five Years: Assessment and Recommendations of the National Nanotechnology Advisory Panel, President's Council of Advisors on Science and Technology, Washington D.C., May 2005, p. 7

[2] Nanoscience and Nanotechnologies: Opportunities and Uncertainties, Royal Society and The Royal Academy of Engineering, UK, July 2004, p. 5.

1.2.2 HISTORY OF NANOTECHNOLOGY

Nanoscience and nanotechnology have blossomed over the past three decades. Miniaturization has risen in importance across a wide range of scientific fields over the past thirty years, including biomedical and chemical engineering; computers; electrical/optical sensors; electronics/mechanics; as well as nanotechnology. While there have been significant improvements in materials science, nanoscience is mostly dependent on the capability to make nanodevices from a variety of materials in smaller and more complicated forms, including sphere-shaped particles and wire-and-rod-and-sphere nanoprism structures. Currently, the production of nanoparticles and nanostructures is established and the manipulation of materials with submicron or nanoscale dimensions has been going on for far longer than anybody could have thought.

1.3 Nanoscale Structures and Functions

The primary benefit of the nanoscale regime is that nanomaterials have a high surface area to volume ratio. As a result, nanomaterials' surfaces exhibit very high surface reactivity, making them excellent for catalytic and sensing applications [4]. Additionally, the systematic structuring of nanomaterials containing biosystem-like proteins enables the development of materials that may be used as artificial components to treat illnesses, combat diseases, viruses, and superficial deficiencies (e.g., artificial muscles) [5]. Furthermore, the capacity to alter basic characteristics of nanomaterials, such as optical and magnetic properties, melting point, and hardness, without modifying their chemical composition is a significant advantage of the nanoscale regime [4]. Nanotechnologists and chemists have mostly concentrated on "bottom-up" techniques for the creation of self-assembling nanomaterials. At the same time, attempts have been undertaken both in theory and in practice to fabricate nanoscale devices and building blocks by "top-down" methods by material engineers using improved etching, lithography, and ablation techniques [4]. To this end, nanoscale entities may be considered "meso atomic" or "meso molecular," that is, aggregates of smaller atomic/molecular components. There are two primary kinds of nanoscale building blocks utilized in the manufacture and implementation of nanodevices: a) zero-dimensional (e.g., nanocrystals, nanoparticles, nanoclusters, quantum dots); and b) one-dimensional (e.g. nanowires, nanotubes, nanofibers). Additionally, these nanostructures may be directly integrated into current devices/materials to impart enhanced capabilities, a process referred to as incremental nanotechnology. Additionally, self-assembly of these nanoscale structures into 2D and 3D building blocks may result in the formation of totally new objects and functions; this process is referred to as evolutionary nanotechnology.

1.3.1 ZERO-DIMENSIONAL NANOMATERIALS

It is widely perceived that a "zero-dimensional" (0D) structure is the most elementary building block in the design and fabrication of nanomaterials [6], [7]. In contradiction, Mori et al. (2005) said that nanoclusters are suitably defined as semi-crystalline or amorphous nanostructures with diameters less than 10 nm (i.e. 1-10 nm) with a comparably narrow size distribution [8]. This distinction is a straightforward extension of the term "cluster," which is typically used in organometallic/inorganic

chemistry to refer to tiny molecular cages of constant size. As with bulk materials, nanocrystalline nanostructural subunit aggregations are readily expressed as nanopowders [8].

The term nanoparticles/nanoclusters should not be confused with conventional colloid structures which date to the early 1860s. As is well known, the word colloid refers to solid/liquid or solid/gas suspensions such as paints, milk, butter, smog, and smoke, among others. While both types of substances have nanoscale sizes, the ability to control the structure and composition of the matter is the key difference. As several researchers have noted, stabilizing chemicals must be used to prevent the agglomeration of nanoscale metal formations into larger scale powders [9]. Additionally, colloids may include eight polydisperse organic polymers and other ionic species that cling to the colloid's surface. The type of the stabilizing agents determines the overall shape and other features of colloids [9]. To create nanostructures by "bottom-up" design, the production process and resulting attributes must be repeatable. This is done by encapsulating compounds with well-established structures that do not react with surfaces but deactivate entrained nanoscale regime organization (e.g. dendrites and fractals). This discussion has thus far concentrated on the terminology for amorphous 0D nanostructures [8]. As with bulk materials, any crystalline nanoscale item should be referred to as a nanocrystal. The phrase is applied to substances that are only partially crystalline; if a particle exhibits just patches of crystallinity, it is best described as a nanocluster or nanoparticles supported by its dimensions. Any nanoscale material's crystallinity may be determined easily using a transmitting electron microscope (TEM) equipped with parallel electron diffraction. Mori et al. (2004) coined the term "quantum dots'' to refer to semiconductor nanocrystals. In concept, these nanoscale objects have architectures ranging from 1 to 30 nm in diameter [8]. These quantum dots have found uses as light emitting diodes (LEDs), lasers, and sensors during the last few decades. Additionally, established high-density disc formats, such as HD-DVD or blu-ray DVD, are created using quantum dots. Solar cells with high efficiency and optical computing devices are examples of materials with lasting nanostructures as well. In general, the word "nanocluster" should be used to refer to zero-dimensional nanostructures with a uniform size distribution [8], [10]. Conversely, those nanostructures which exhibit relatively larger size distribution should be described as nanoparticles [11][12]. Nanocrystals should be categorized by the existence of well-ordered lattice arrays of constituent subunits, as exemplified by single nanocrystals of cadmium selenide [13], [14]. In contrast to nanocrystal, a nanosized regime structure is characterized as nanopowder when it is composed of microscopic grains, each consisting of nanoscale amorphous units [15]. Material structures and devices with intermediate sizes between the nano- and micro-regimes (10^{-9}-10^{-6} m) are better expressed as submicron. However, the bulk powder scale is generally referred to as 200 μm and above [10].

1.3.2 ONE-DIMENSIONAL NANOSTRUCTURES

Another class of nanoscale building blocks is referred to as 1D nanoscale architectures, which are structures with nanoscale dimensions comparable in all directions except one. As previously stated, 0D structures have a length equal to their width, but 1D structures have a length greater than their breadth.

The phrases nanorods, nanowires, nanotubes, and nanofibers are considered to be synonymous with 1D nanostructures in the literature due to their imprecise application to a variety of nanostructures without proper explanations. With similar bulk materials (without the suffix "nano"), there is no misunderstanding in the application of this terminology. However, a frequent criterion for "nano" descriptors is that the diameters of the particles/structures stay in the nanoscale range (i.e. 1-100 nm), although the lengths are often in the micro (or greater) size range. A nanotube is a one-dimensional structure with a hollow core, whereas the other three nano-architectures are completely solid. The word "nanofiber" refers to amorphous and often nonconductive one-dimensional nanostructures made of polymers and other non-graphitized carbonaceous materials. In comparison, a nanowire is a crystalline one-dimensional nanostructure with either metallic or semiconducting electrical characteristics. A nanorod is a crystalline one-dimensional nanostructure with a width of 1–100 nm and aspect ratios greater than 1/1 but less than 20/1. The crystalline nanorods appear to take on the overall form of needle-like bulk crystals. Additionally, the name "nanocrystal" or more conceivably "rod-like nanocrystals" may be more accurate for these nanostructures. These nanofibers, nanotubes, and nanowires can be used to define an interwoven array; nanorods have a full linear shape. Indeed, nanorods can stack on top of one another to form intriguing 2D and 3D structures, however this is not always easy to do with "spaghetti-like" morphologies of some 1D nanostructure materials [10].

1.3.3 SOME SPECIFIC TYPES OF NANOSCALE STRUCTURES AND THEIR USES

It is well acknowledged that nanoparticle synthesis does not require merely a tiny size of precursors. Controlling the processing conditions is necessary for any practical application to ensure that the resultant nanoparticles exhibit the following characteristics: (i) identical particle size, i.e. monosized or with a uniform size distribution; (ii) identical morphology or shape; (iii) identical crystalline structure and chemical composition (surface and core compositions should remain identical); and (iv) particles must remain monodispersed or individually dispersed, i.e. without agglomeration. In the following table (Table 1) some typical applications of various nanostructured materials are presented.

Table 1. Nanostructured materials and their usual applications in nanoscience and nanotechnology

Nanostructure materials	Applications
Nanoparticles/Nanoclusters	Catalysis
Quantum dots	Sensors
Nano films/ Ultra-thin layers	Adhesives and coatings
Nanostructure interfaces and layers	Paints, dyes and cosmetics
DNA or any biological structures	Medicines/Drug delivery systems
Nanocomposite hybrid materials	Materials ceramics
Nanoactuators	Optics

Nano/Meso porous materials	Information storage
Nanowires	Magnetic, electrical, optical devices and switches and electronics (quantum computers)
Nanoreactors	Energy (batteries, fuel cells, solar cells)
Nanotubes	Separation technologies

1.4 Nanoparticle Synthesis

Nanotechnology is without a doubt one of the most vital sectors of science and technology in the modern era. The majority of people have seen "nano" as one of those odd technologies that will both save and destroy humanity. As is customary, reality resides somewhere in the middle of these two extremes. The ability to manipulate materials on the nanoscale undoubtedly enabled the development of such machines in a plethora of sectors of life that were unthinkable just a few decades ago. The potential for focused on conveyance and controlled discharge of drugs inside the human body [16], the storage of hydrogen [17], the enhance of vitality, nutrition, and water supply [18], the development of biosensors [19] and antiviral surfaces [20], the fabrication of lightweight yet durable materials [21], or the efficiency-increase of solar-based cells and batteries [22] are fair some cases that nanotechnology can offer.

Although several advancements in nanotechnology and nanoscience have already reached the industrial level and have become a part of everyday life, numerous ground-breaking applications continue to exist solely inside the confines of research institutions. A few requirements must be satisfied before a new technology may emerge from the laboratory, including the availability of appropriate base material. The essential building blocks of nanotechnology are nanostructures, which can be layers, nanorods, or nanowires, or nanoparticles, which are together referred to as 2D, 1D, and 0D nanostructures [23]. The natural and inexpensive mass manufacturing of such nanostructures may be a critical technical hurdle if nanotechnology-based product innovation is to continue. The present thesis is focused on a few of the elemental angles of the spark discharge nanoparticle era, one of the foremost promising strategies which are capable of creating nanoparticles (NPs) with controlled properties indeed on the industrial level.

When reviewing all of the ways for producing nanoparticles, the most profitable strategy may be to start with those processes that do not produce NPs. Even though this remark is a little exaggerated, it is undeniable that NPs may be made in a variety of ways. In reality, the ambient air is continually surrounded by many forms of aerosol "NP generators" in the form of gasoline engines in automobiles [44], almost any sort of combustion source [45], constructions and demolitions, and even smoking cigarettes [46], to mention a few. Furthermore, regardless of anthropogenic sources, NPs have always existed in the environment due to natural production mechanisms [47]. In the cases shown above, NPs are commonly synthesized inadvertently, uncontrollably, and with little control over the final physical and chemical properties. As a result, they are clearly minor "techniques" in industrial and laboratory applications that frequently demand NPs with well-regulated properties. To avoid ambiguity, NPs that are purposefully

created with the intent of manipulating their composition, shape, size, surface function, and so on, are frequently referred to as engineered nanoparticles (ENPs) [48]. ENPs can be synthesized in a variety of ways, which can be roughly distinguished according to the direction in which they are synthesized (top-down or bottom-up techniques) (Figure 1), the phase in which they are synthesized (gas, liquid, or solid phase processes), or the nature of the underlying mechanisms (physical, chemical, biological synthesis).
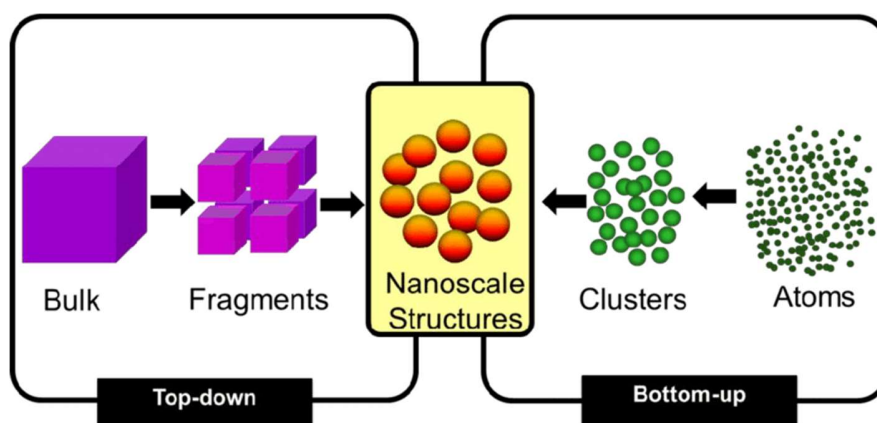

Figure 1. illustration of the top-down and bottom-up approach for making nanoparticles [51].

Chemical production of NPs dates back to the 4th-century Roman glass cage cup (Lycurgus cup) made of a dichroic glass, where the dichroic effect was achieved by making the glass with tiny proportions of nanoparticles of gold and silver dispersed in colloidal form throughout the glass material. After that, during the eighteenth century, Faraday created metal NPs by reducing metal salts with a phosphorous-carbon disulfide combination [49]. Chemical methods, regardless of their composition, invariably involve chemical precursors, reagents, and frequently large amounts of solvents, all of which inherently increase the possibility of contamination, which can act as a diversion executor at the nanoscale, as impurities can significantly alter the properties of nanostructures [26]. Physical approaches are a viable alternative to chemical means since they demonstrate inherent advantages over competing tactics, such as nonstop generation, high NP quality, lower waste, and more obvious flexibility [27]. The most well known among physical production methods is Flame Spray Pyrolysis (FSP) (Figure 2). FSP is an established and attainable strategy for mechanical scale generation of metal-oxide particles [28], but unsuitable for the generation of unadulterated metal particles. Metal NPs are often formed by material evaporation in a carrier gas followed by subsequent nucleation and condensation [29]. Evaporation can be achieved in several ways, e.g. using a conventional furnace [30], glowing wires [31], or laser ablation [32]. The most energy efficient and demonstrably up-scalable method for the evaporation of conducting materials is Spark Discharge Generation [33] (Figure 3).
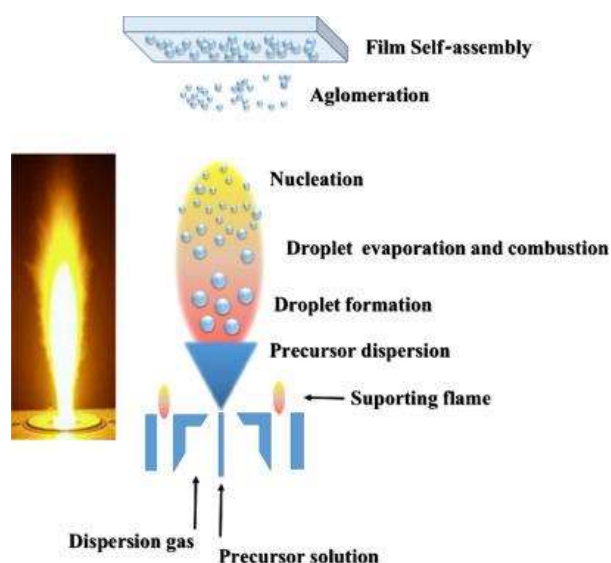
Figure 2. Schematic of flame spray pyrolysis synthesis [34].

The spark discharge generator (SDG) is a simple device that consists of a leak-tight chamber that contains two electrodes separated by a small spacing. To generate a spark between the rods, a self-pulsed circuit is frequently utilized. This circuit consists of a capacitor energized by a high voltage DC control supply connected to the electrode distance. Each spark is initiated when the gaseous ambience between the electrodes decomposes, i.e. when a conducting channel (spark channel) is formed between the two rods. The spark plasma disintegrates the electrode material, resulting in the creation of an aerosol. Due to adiabatic extension and mixing with the carrier gas, the molecules cool down and inevitably frame nanoparticles, aggregates and agglomerates after nucleation, condensation, coalescence and coagulation (Figure 3) [35]. The potential for mass production of NPs using spark discharge is predicated on its relative ease of use. More importantly, the same technique may be easily and precisely scaled up by connecting a few electrode sets in parallel at a low cost and with no environmental impact.
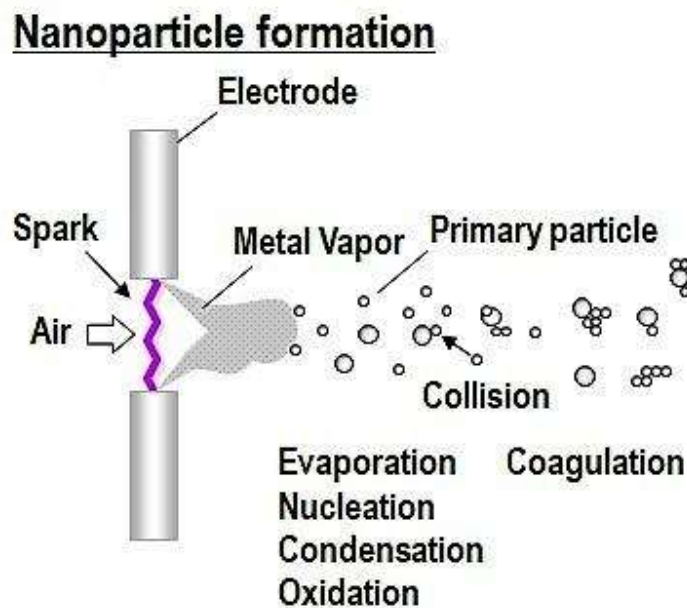
In spite of the fact that the most standards of the SDG have been around us since the innovation of the spark plug of a gasoline motor, the primary use as a NP generator dates back to 1988 [33], when Andreas Schmidt-Ott and his colleagues began to see results. Although SDG is presently commercially accessible and utilized by several groups [37] – [42], its products and their distribution on the depositions is not completely understood. One explanation for this knowledge gap is the difficulty of researching the phases of the inherently multiscale nanoparticle organization process, particularly its early stages. The solution to this has taken two distinct techniques to characterize gas-borne particles. Typically, NP collection (e.g., investigation on various substrates) is followed by off-line electron microscopic analysis. In the alternative technique, aerosol instrumentation capable of performing in-line estimates is used, such as a checking mobility particle sizer (SMPS), a condensation particle counter (CPC), and so on. Another difficulty inherent in the analysis of nanoparticle arrangement on deposited air filters (substrates) is the method's multi-scale character. Particle arrangement occurs at the point at which the agglomerates make contact with the substrate for the first time and is mostly determined by the size of each individual aerosol mass [43]. Each spark, however, exhibits an identifiable temporal evolution characterized by remarkable physical miracles, which affects electrode erosion and hence the synthesis and deposition of NPs [43].

However, the structure of a SDG imposes some constraints on the appropriate test methodologies. The standard SDG design cannot be altered much for the sake of testing on plasma, as this would undoubtedly alter the NP formation handle as well. This prevents possible estimating procedures to those capable of gathering important data, on the forms included inside the SDG, without causing them the least

19

disruption. Keeping these constraints in mind, the research presented in this thesis focuses on non-invasive in situ strategies, specifically temporally changing electrical circuit and control parameters, complemented by persistent estimation of the discharge's electrical signals (i.e. voltage and frequency from an oscilloscope) for data collection when the spark occurs; SMPS is also used to detect and quantify the results. These methodologies enable the examination and prediction of the mean size and concentration of the nanoparticles generated. These techniques are supplemented by the characterization of the generated particles and the ex-situ characterization of the shape of the electrode surfaces, with scanning electron microscope (SEM). These experimental methodologies enabled a close approach to the problem of comprehending the peculiarities of the spark-based NP arrangement from a variety of different angles. Each technique was employed to get knowledge and portray the plasma spark's effect on the electrode material, and the subsequent production and deposition of nanoparticles, aggregates and agglomerates on various substrates (air filters). The careful examination of the data gained enabled the understanding of a deeper knowledge of the spark, and ultimately the acquisition of more control over the nanoparticle creation in SDGs. Finally, nothing is more important than utilizing each experiment and technique. Thus, in trying to put the findings into action, efforts have begun to embody possible applications for both antibacterial and antiviral surfaces as well as aerosol detection biosensors.

1.5 Spark Discharge Fundamentals

One of the first scientific explanations for the observed spark discharges extend back to the 18th century, when B. Franklin established empirically that laboratory spark discharges and lightning originate from the same source. When it was found that short circuiting between the wires of high-voltage transmission lines was caused by sparks, the field expanded rapidly. The event was named the "breakdown" of air insulation [62]. The term "gas discharge" refers to the process by which a capacitor in a circuit with a gas-filled electrode gap is discharged. When the voltage between the electrodes is sufficiently high, the space between them becomes conductive owing to the formation of ions and electrons, thereby shutting the circuit and discharging the capacitor. The term "discharge" refers to any process in which an electric field ionizes a gas and then conducts an electric current through the ionized gas [62].

Cosmic rays or natural radioactivity-generated charge carriers always initiate the gas breakdown process. When an electric field is present, such as when a voltage is applied to electrodes, electrons and ions with opposing polarities are pulled in the direction of the electrodes, and current begins to flow. When the voltage is increased over a certain point, the current rises substantially and visible light emission occurs. These occurrences are caused by the breakdown process. The avalanche of electrons that occurs when they gain enough energy from the electric field to ionize the gas atoms and therefore generate further electrons is the basis for breakdown. The features of the electric circuit and the surrounding gas environment have an effect on how the discharge proceeds following breakdown. The most frequent types of discharges include glow, arc, spark, and corona [62]. Gas discharges produce plasma, which is an ionized gas that is macroscopically neutral [62]. It should be underlined that Langmuir invented the term

plasma, which was initially used for gas discharges. Originally, it was used to refer to the region of a gas discharge that is untouched by the electrodes or discharge tube walls [63].

Glow discharges are frequently generated at low pressure and are characterized by a relatively high voltage, low current, and extremely weakly ionized plasma. Due to the fact that the electron temperature is significantly higher than the gas species' temperature, glow discharge plasmas are not in a thermodynamic equilibrium. The most prevalent form of gas discharge plasma in thermodynamic equilibrium is the arc discharge. Arcs develop when a large current is allowed to pass across a relatively small voltage difference between two electrodes. At atmospheric pressure, the gas temperature is about equal to the electron temperature, showing that the arc plasma is in (local) thermodynamic equilibrium [62]. Arc plasma creates heat as a result of the high current, which may cause the electrodes to melt. In contrast to arcs and glows, which are quasi-steady and self-sustaining discharges, sparks are temporary phenomena. When the voltage between two electrodes reaches the electrode gap's breakdown voltage, a conducting channel forms between the electrodes, resulting in sparking. Due to the high conductivity of the spark plasma, the voltage rapidly decreases and the discharge terminates. The colloquial idiom "a spark leaps" from one electrode to the next is an apt description of this spontaneous, transient action [62]. Spark generation is a complex phenomenon that may be represented by a variety of processes depending on the discharge conditions. At small distances and/or low pressures, the breakdown mechanism can be represented by the multiplication of corona discharges, or the so-called Townsend mechanism (approximately 1 cm at atmospheric pressure) [64].

The characteristics of a spark discharge can be quite variable, depending on the characteristics of the discharge circuit [65]. The existence or absence of thermodynamic equilibrium in the discharge plasma allows for the differentiation of several types of sparks [66]. The spark plasma might be non-thermal or thermal, depending on the type of sparks employed. Transition sparks are a type of discharge that is associated with non-thermal plasmas. By repeatedly discharging a pF capacitance in a high-resistance (megaohms) circuit, transition sparks are generated, culminating in a train of 100 ns long sparks that are far from thermodynamic equilibrium [67]. In contrast to transition sparks, which often have a very small discharge gap and a very short characteristic length, sparks may also be generated over electrodes separated by a great distance (several meters) and with a much longer characteristic duration. On the other hand, these prolonged sparks are believed to be non-thermal, that is, they are not in thermodynamic equilibrium [63]. It is also possible to build spark plasmas capable of achieving local thermodynamic equilibrium. Under atmospheric pressure, such spark discharges can be produced by discharging a capacitor (capacitance typically between 1 and 20 nF) in a discharge loop with a small electrode distance (often on the order of millimeters) and low resistance and inductance. The resulting sparks are several microseconds in duration, carry a large current (in the hundreds of amps range), and have a bipolar, oscillating character [68].

1.6 Spark Discharge Nanoparticle Generator

Since 1907, electrical discharges have been known to produce aerosols [69], and the first source of spark discharge was produced in 1988 [33]. It was initially utilized in magnetic field-based mass spectrometry research and, more recently, for PIV (particle image velocimetry).

1.6.1 PRINCIPLE OF THE METHOD

The technique is based on the generation of plasma between two conducting elements to which a voltage is applied while a carrier gas flows [64]. Metal particles are evaporated in this procedure and then cooled in the carrier gas to form nanoparticles [64]. These initial particles have a diameter of a few nanometers and can form agglomerates with one another depending on their environment and concentration [43].

1.6.2 TYPES OF SPARK DISCHARGE SOURCE

The spark discharge ionization source was one of the earliest ionization sources to be utilized in magnetic field-based mass spectrometry experiments [70]. According to Alfred *et al.* (2015) spark discharge ionization generates periodic discharges by applying a high voltage (> 20 kV) RF sinusoidal waveform at frequencies of 1 MHz or larger between two conductive cells. Both the gas and the conductive substance that is evaporated and enters the gas phase are ionized, and the mass of ions generated is determined using a magnet. Due to the low precision provided by the vast range of starting ion kinetic energy, this type of ionization source was limited in use [70].

There are two types of spark discharge sources: those in which the spark is generated by a carrier gas flow (He, Ar, dry air, N_2) and those in which the spark is generated by a solution of ethanol (CH_3-CH_2-OH) or water (H_2O). In the first case, there are at least five distinct production configurations for nanoparticles, with some of them producing primary particles of varying sizes [71]. There are sources with electrodes that are a) both rods (rod-to-rod), b) and two wires (wire-to-wire), c) one rod and the other wire (rod-to-wire), but also combinations such as d) one end of a rod and the other plate (pin-to-plate) and e) wire-to-plate [71] (Figure 4). Additionally, there are devices with three ionization sources connected in series, which create far more nanoparticles and consume less energy than devices with a single source [72]. In the second case, nanoparticles are synthesized in a solution of ethanol or distilled water, and the resulting particles are either deposited on cloth or settle to the bottom of the container [73].
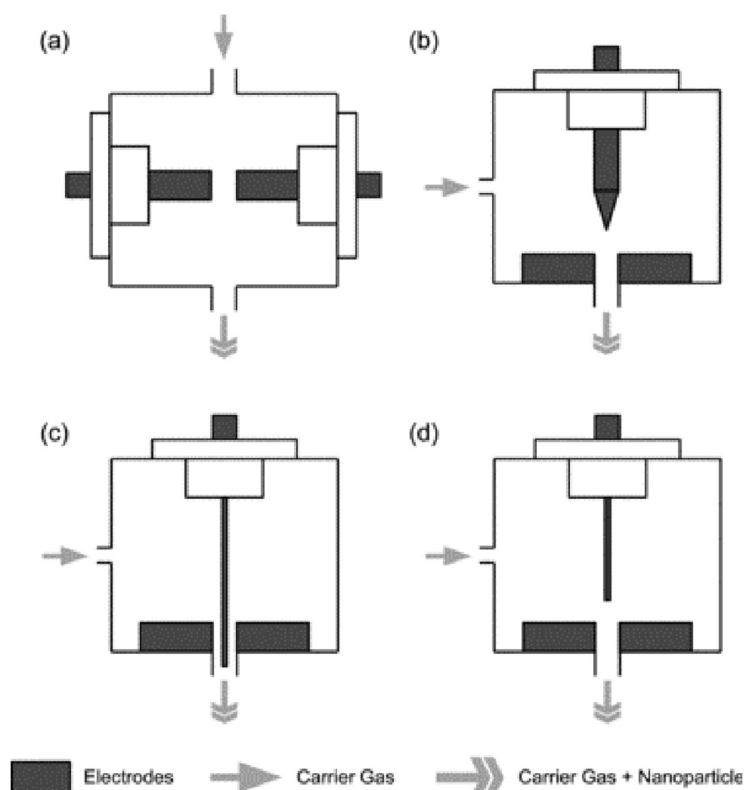
Figure 4. Four types of spark sources with electrodes (a) rod-to-rod (b) pin-to-plate (c) wire-in-hole (d) wire-to-plate [75]**.**

1.6.3 COMPARISON OF OTHER METHODS WITH THE SPARK DISCHARGE SOURCE

In comparison with other nanoparticle manufacturing methods, the spark discharge generator is a straightforward and affordable approach since it does not need sophisticated procedures, expensive consumables (e.g., reagents), or safety equipment. Additionally, the absence of liquid solvents in the reactants, contributes to the purer formed nanoparticles. It is a continuous process, as manufacturing is continuous and not batch-based, and it enables the manufacture of even bimetallic materials, as electrode alloys may be employed. Finally, it is eco-friendly because it generates no waste for decomposition. The deficiencies of this method include the difficulty of depositing particles on surfaces and the inability to utilize non-metallic electrodes to produce a spark.

2. EXPERIMENTAL SETUP

During the present thesis, a rod-to-rod SDG from Fasmatech was used. According to the operating principle, two elongated electrodes are positioned a few millimeters apart in the spark discharge chamber, with the carrier gas flow oriented perpendicular to the electrodes' axis. The electrodes are linked in parallel with a capacitor that is charged continuously by a steady current source, therefore raising the voltage between the two electrodes. When the breakdown voltage is achieved, a spark discharge occurs, causing some of the electrode material to evaporate. The evaporated material, which contains ions, electrons, and neutral elements, is cooled by the carrier gas flow passing through the sample tube, allowing the nanoparticles to aggregate and form. Due to their rapid reaction time and subsequent ability to properly follow complicated flow fields, these so-called nanostructured inert particles flow and deposit on any fibrous substrate the user wishes to. A schematic representation of a spark discharge source is shown in Figure 5.
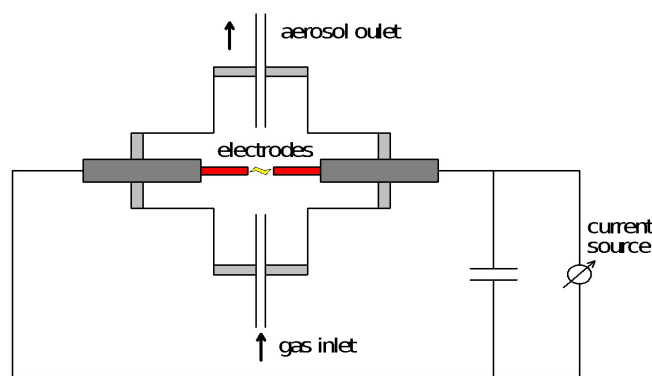

Figure 5. Schematic diagram showing the basic elements of a spark discharge source [76]**.**

2.1 Setup of SDG

Figure 6 depicts the spark discharge chamber made by Fasmatech [76]. The individual source pieces were positioned using a five-fold NW50 cross, which is briefly discussed. A 1/4 1/4 'exterior diameter tube is linked to the bottom of the NW50 flange through a perforated 1/4 NPT screw and brought close to the aluminum electrodes. Nitrogen gas is provided at a flow rate of 2-6 L / min, which is adequate for measurements with a differential mobility analyzer (DMA) and also corresponds to the mass spectrometer's capillary input sampling flow. On opposing ends of the electrodes are attached a 15 kV feedthrough with two pins and a feedthrough with axial displacement capability. A pure Teflon support base (PTFE) has been physically adjusted to screw into one of the high voltage feedthrough's pins and to retain the numerous electrodes used in the tests. The distance between the electrodes is measured using the distance meter attached to the axial displacement unit that contains the second electrode. Between

the discharge region and the outlet port, an extra Teflon section is inserted to guide the gas and improve the efficiency of sampling the nanoparticles from the output pipe.
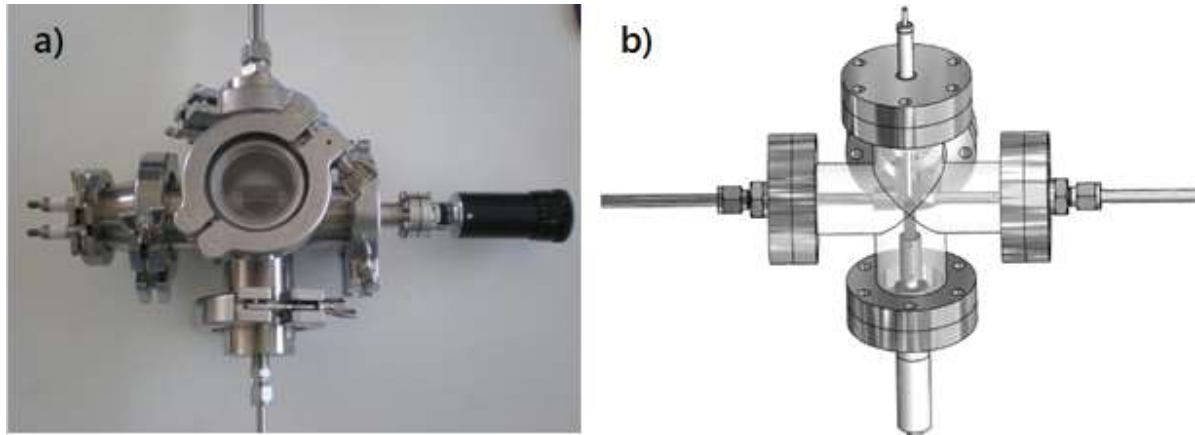

Figure 6. a) Photo of the spark discharge source highlighting the optical access door available through a plexiglass window and b) Overview graphical representation of the assembled spark discharge source (chamber) [76].

2.1.1 ELECTRICAL CIRCUIT
2.1.1.1 Initial circuit

Two subcircuits are required to charge and discharge the capacitor, as well as a DC voltage source, a capacitor, a resistor, and a coil (Figure 7). The procedure for creating a spark discharge was as follows: the source charges the capacitor (left circuit-charge circuit), and when the voltage reaches the breakdown voltage, a spark occurs, which discharges the capacitor. The process is then repeated.
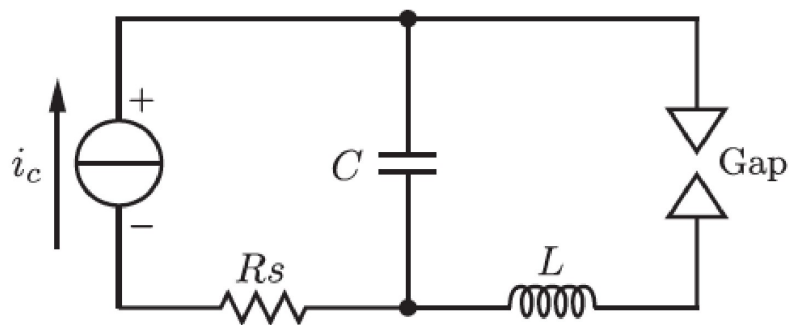

Figure 7. Schematic diagram of the electrical circuit for spark discharge [35].

However, as a result of the foregoing, the breakdown voltage V_{dis} is uneven (Figure 8), resulting in an irregular energy per spark. Thus, the use of a power source eliminates fluctuations in the decay voltage and spark repetition rate (SRR) and maintains the uniformity of the nanoparticles' characteristics.
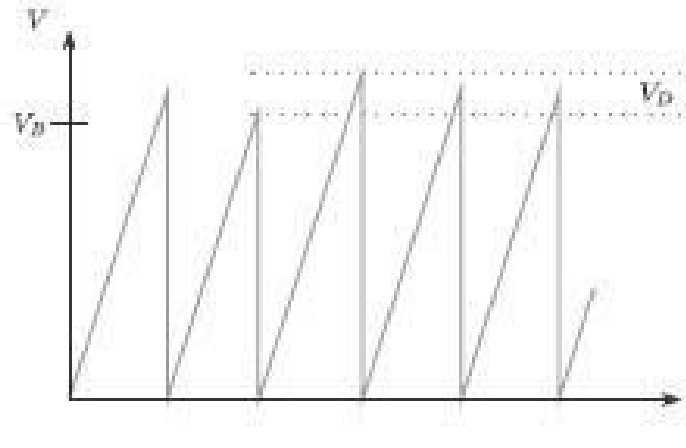

Figure 8. Schematic diagram of changes in breakdown voltage V_{dis} [35].

2.1.1.2 Breakdown Voltage

As previously stated, a large electric field is required to ionize the gas molecules caused by the speeding electrons and ions, therefore creating the conductive plasma between the electrodes. Additionally, this process creates X-rays with energy less than 10 keV, referred to as soft X-rays [77]. These X-rays are not powerful enough to penetrate the chamber walls, and no radiation has been reported from any of the setups tested [77]. The breakdown of the isolating gas is governed by Paschen's law. The breakdown voltage V_b is given by Equation (1):

$$V_b = \frac{Bpd}{\ln\left[\ln\left(1+\frac{1}{\gamma}\right)\right]} \quad (1)$$

where p is the pressure in pascals, d is the gap distance in meters, γ is the secondary-electron-emission coefficient (the number of secondary electrons produced per incident positive ion), A is the saturation ionization in the gas at a particular E/p (electric field/pressure), and B is related to the excitation and ionization energies [43].

2.1.1.3 Capacity, frequency (SRR) and energy

The capacitor's capacitance has a significant effect on both the spark frequency and the discharge energy. This device is capable of selecting capacities of 0.47 nF, 0.94 nF, 1.47 nF, and 1.94 nF. The following equation (2) calculates the spark frequency (SRR):

26

$$f = \frac{I}{C * V_d} \quad (2)$$

where C is the capacitance, V_d is the discharge voltage and I is the charging current [43]. V_d is not equal to V_b and there is a voltage V_o for which $V_d = V_b + V_o$ applies. Since V_o is unpredictable, the frequency (SRR) is often easier to measure than to calculate [78]. The energy of the capacitor and the discharge is given by Equation (3):

$$E = \frac{1}{2} * C * V_d^2 \quad (3)$$

Increasing the concentration of nanoparticles is possible by increasing the frequency of electrical discharges (SRR) and by placing the electrodes further apart, thereby increasing the breakdown voltage and thus the energy released during the discharge, which results in a greater amount of material in the gaseous phase [43].

2.1.2 CARRIER GAS

The type and flow rate of the carrier gas have a significant effect on the number and size of nanoparticles produced. For instance, the presence of electronegative molecules enhances the breakdown voltage, since they bind electrons that would otherwise flow between the electrodes, thus creating a current flow. As seen above, the breakdown voltage is proportional to the breakdown energy and hence to the amount of material created. Additionally, the gas flow has an effect on both the aggregation of the nanoparticles and the initial cooling.

2.1.3 PARAMETERS THAT AFFECT THE SIZE AND MASS OF THE PRODUCED NPS

The particle mobility size d_m as determined using a SMPS is the diameter of a sphere with the same mobility as the actual particles. The particles coming from the spark generator are not spherical, however. Due to the high concentration of particles in the spark generator, small primary particles agglomerate to form so-called fractal-like agglomerates. A fractal-like agglomerate with a mobility particle size d_m made up of primary particles with size d_{pp} can be characterized by the following scaling law [79], [80]

$$n_{pp} = A_1 \left(\frac{d_m}{d_{pp}} \right)^{D_f} \quad (4)$$

where n_{pp} is the total number of primary particles making up the agglomerate, and A_1 is a constant of the order of unity [80], [81], here it is assumed to be 1. D_f is the so-called fractal-like dimension. The mass of the agglomerate m_{agg} is given by the sum of the mass of the primary particles making up the agglomerate. The total mass concentration M_{agg} is then simply the sum over all agglomerates in the aerosol

$$M_{agg} = \int_0^\infty n_{agg}(d_m) n_{pp}(d_m) m_{pp} dd_m \quad (5)$$

27

where $n_{agg}(d_m)$ is the concentration of agglomerates with a given mobility size, which follows directly from the particle size distribution. If the primary particle size is the same over the entire size distribution, then it can be shown that

$$M_{agg} = \frac{m_{pp}}{d_{pp}^{D_f}} \int_0^{\infty} n_{agg} d_m^{D_f} dd_m \quad (6)$$

According to Vons (2010), without knowledge of the primary particle size d_{pp}, as a general trend, it is safe to say that information about the quantity and behavior of type i NPs can still be obtained by the SMPS data [82].

According to Vons (2010), when the vapor generated by the spark cools, initially liquid particles are formed. When two liquid particles collide, they sinter through viscous flow. In the case that the electrodes consist of a metal that oxidizes there are several additional parameters that should be considered. For the case of Cu electrodes, for example, the melting point of pure metallic copper is 1085 °C, whereas copper oxide on the other hand has a higher melting point of 1326 °C. This means that as the particles cool due to contact with the surrounding gas, non-oxidized particles exhibit viscous flow for much longer and thus show higher coalescence rates (i.e. larger particles). Even when the temperature drops below the melting point of the material, the coalescence rate of metallic material, such as copper, is still likely to be orders of magnitude higher than that of its oxide. It is well known that the presence of a surface oxide has a pronounced effect on the surface diffusion rate [82]. Nanoparticles of noble metals like gold [83], which do not acquire appreciable amounts of surface oxide, have low activation energies for sintering.

Therefore, as long as a copper particle does not acquire any surface oxide, it can continue to grow, perhaps even at room temperature. However, as soon as a continuous oxide layer is formed, coalescence is hampered greatly and the domain size is practically frozen. The only growth of the particle is then through agglomeration. A (simplified) schematic illustrating the influence of oxidation on coalescence and the resulting particle morphology is given in Figure 9.
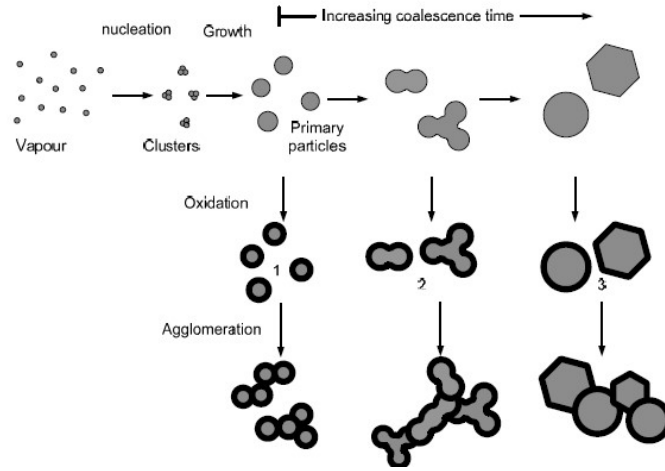
According to Tabrizi et. al. (2009), in the end, the production of material (and therefore the erosion of the electrode) depends mainly on the physical characteristics of each material. In general, in terms of electrode erosion and mass production, the spark strikes the electrode, converting electrical energy into heat energy and causes local evaporation of the electrodes. Thus, the thermal parameters of the electrode material, such as the boiling point and evaporation enthalpy, undoubtedly influence particle production. Assuming that the effective area for energy transfer is the area of the hot spots A (m^2) on the electrodes [112], the energy balance around the hot spots can be estimated by the following equation, which relates the eroded mass due to the evaporation, to the physical properties of the electrode material [113][114]:

$$m = \frac{\frac{1}{2}c_e V^2 - bT_b^4 - gk(T_b - T)}{c_{ps}(T_m - T) - \Delta H_m + c_{pl}(T_b - T_m) + \Delta H_v} \quad (7)$$

The first term in the numerator represents the effective spark energy, with c_e (F) representing the effective gap capacitance and V the breakdown voltage (V). The second term denotes the heat loss from the hot spots by radiation in which T_b(k) is the boiling point and b=Aσt (Jk^{-4}) with σ depending on the blackness of the metal (for black bodies σ is Stefan-Boltzmann constant 5.67×10-8 Js^{-1}m^{-2}K^{-4}). The time for energy transfer is t. The third term indicates the heat transfer from the hot spots by conduction, in which k is the thermal conductivity (Wm^{-1}K^{-1}) and g=2(πA)$^{0.5}$ t (ms) if (r^2 /Kt)$^{0.5}$ <<1, in which K is the thermal diffusivity (m^{2}s^{-1}) and r the radius (m) corresponding to A. T is the steady state temperature (K) far from the hot spot (i.e. ambient temperature). The first and second terms in the denominator represent the energy required to heat the electrode material to the melting point T_m (K), with C_{ps} (Jg^{-1} K^{-1}) the average heat capacity of the solid, and ΔH_m (Jg^{-1}) the enthalpy of melting. The third term in the denominator is the energy needed to heat the liquid to the boiling point, with C_{pl} (Jg^{-1}k^{-1}), the average heat capacity of the liquid, and ΔH_v (Jg^{-1}) the enthalpy of evaporation. The evaporated produced mass is denoted by m (g). The model excludes any chemical reaction and ignores material transfer between the electrodes. The material constants in

the equation are known. The constants c_e, b and g are assumed independent of the electrode material. Making the further simplifying assumption that the electrodes are black bodies gives us the values r~0.5 mm and t~16 ms. Both values are in the expected range. In general, materials with higher thermal conductivity show less evaporation, because they are cooled more effectively [115].

2.2 Final Setup

The final experimental setup for the nanoparticle production (Figure 10) consists of a gas bottle (N_2), two flowmeters, (one for the carrier N_2 gas and the other for dilution regulation that goes into the SMPS), the electrode chamber (Figure 11), the power supply, the sample holder (where the various substrates for deposition are placed) (Figure 12), HEPA filters (to release excess gas into the environment and to ensure the integrity of the experimental device) and the pump (which also draws air from the environment through a HEPA filter).
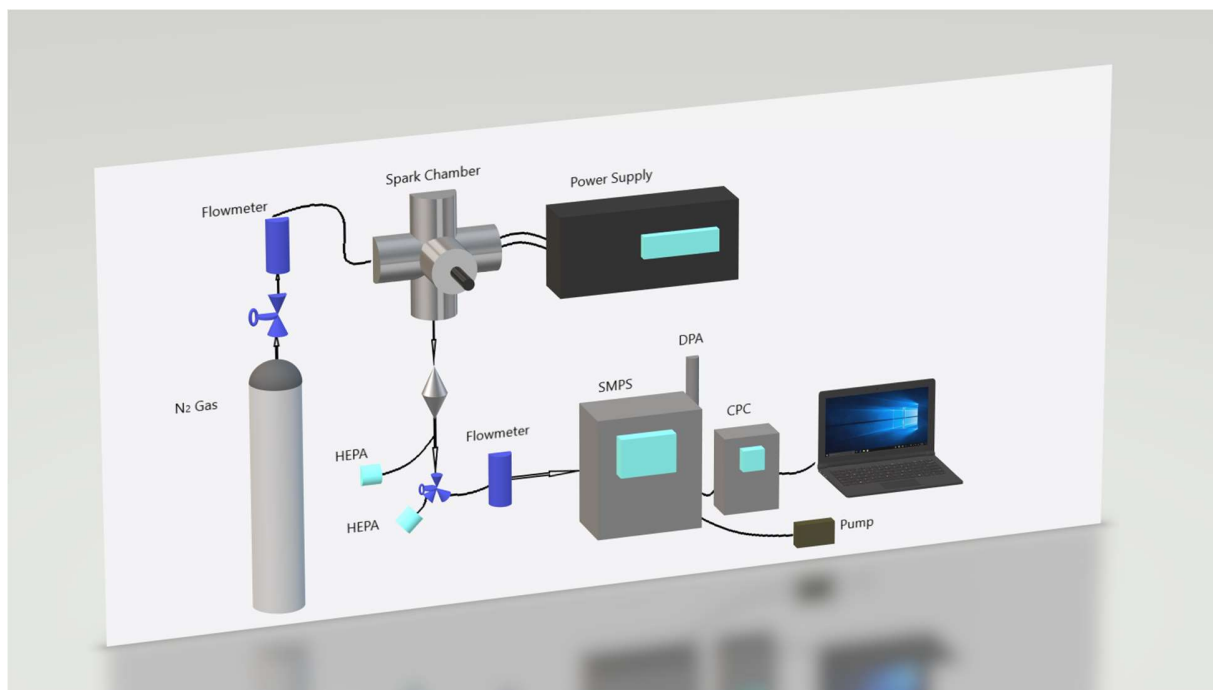

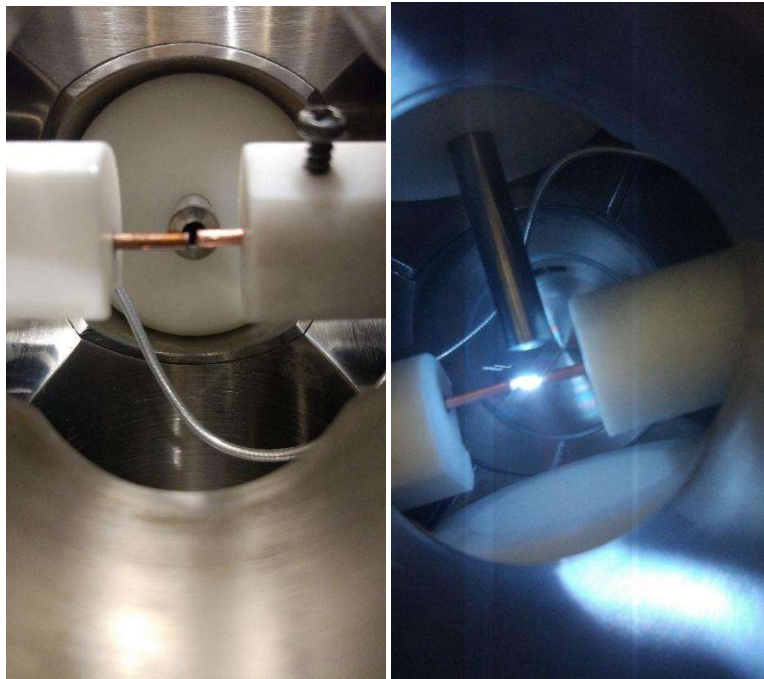Figure 10. 3D model of Spark Discharge Generator Experimental Setup.

Figure 11. Spark Chamber with Cu electrodes without (left) and during (right) spark.
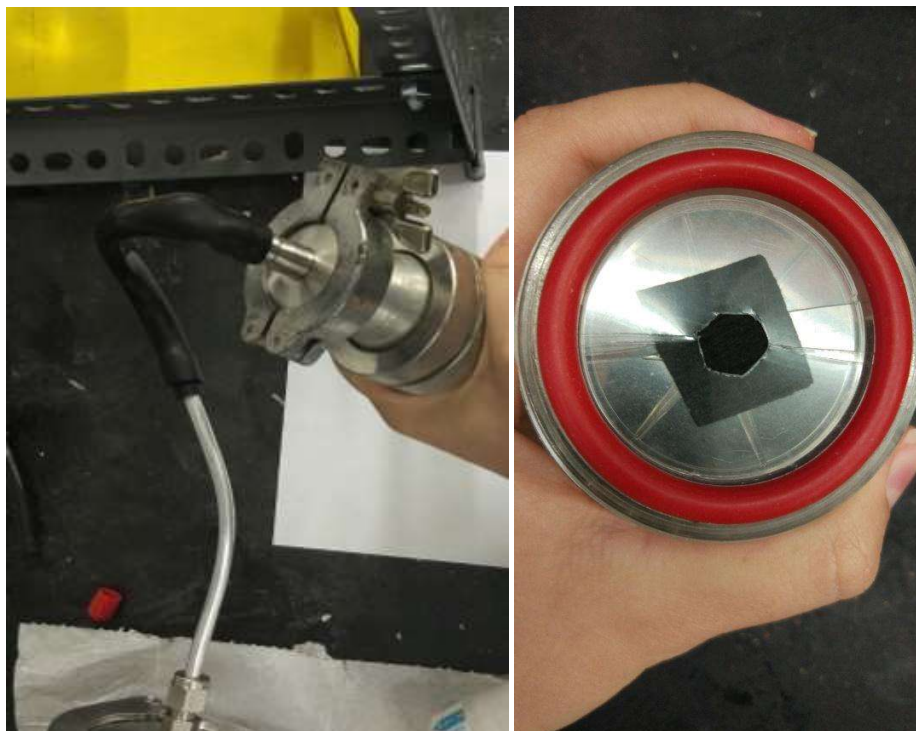

Figure 12. Sample Holder.

3. Characterization Techniques

3.1 Scanning Mobility Particle Sizer (SMPS)

Three subsystems comprise the Scanning Mobility Particle Sizer Model 3936 by TSI (size range 2.5 nm – 1 μm, concentration range up to 10^7 particles/cm^3): an intake impactor, an electrostatic classifier, and a condensation particle counter (CPC). The aerosol enters the impactor (which eliminates particles larger than a predetermined particle size by inertial impaction) before entering the electrostatic classifier, which separates a predetermined size fraction from the incoming polydisperse aerosol. The resultant monodisperse aerosol is then counted at the CPC. Figure 13 illustrates the flow scheme for the intake impactor and electrostatic classifier, whereas Figure 14 illustrates the flow scheme for the CPC.

The aerosol enters a Krypton-85 bipolar charger (or neutralizer) in the electrostatic classifier, where it is exposed to high concentrations of both positively and negatively charged ions. The particles swiftly establish charge equilibrium as a result of many collisions with the bipolar ions. The charged aerosol then enters the long-column Differential Mobility Analyzer (DMA), where a user-defined electric field induces particles with a certain electrical mobility to escape the column and enter the particle detector, which is a Model 3772 CPC in this particular SMPS [84].

The particle detector enlarges the sampled particles into bigger droplets that are optically detected. The intake sampler collects laminar aerosol flow and directs it to the saturator, where evaporated butanol liquid saturates the aerosol flow with butanol vapor. After entering the condenser, the combined flow of aerosol and butanol vapor is cooled using a thermoelectric device. The butanol vapor becomes supersaturated at this point and condenses on the aerosol particles, forming bigger droplets. These butanol droplets are directed through a nozzle into an optical detector that consists of a laser diode, different focusing and collecting lenses, and a photodiode detector. However, as butanol droplets travel over the laser, they scatter light, which is detected by the photodiode and transformed into electrical

pulses that are counted and, in the case of high particle concentrations, compensated for particle coincidence [84].
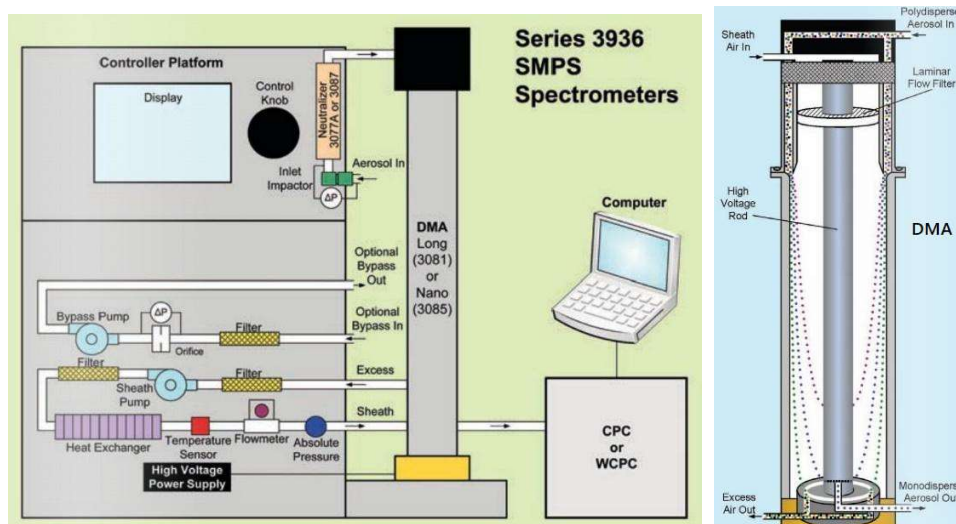

Figure 13. Flow schematic for the inlet impactor and electrostatic classifier with a long-column DMA[84].

Aerosol flow is accelerated in the impactor by directing it through a nozzle toward a flat plate. The impaction plate deflects the flow, resulting in a 90° bend in the streamlines of the flow. Particles having a considerable inertia cannot follow the streamlines and, as a result, collide with the plate. However, smaller particles with less inertia follow the streamlines, avoid colliding with the plate, and escape the impactor through the electrostatic classifier [85].

The data inversion technique used to get the ambient size distribution from raw particle count and diameter measurements makes the assumption that the polydisperse aerosol entering the DMA has reached charge equilibrium prior to electrical mobility categorization. Charge equilibrium is achieved using a Krypton-85 bipolar charger (neutralizer). The measured aerosol collides often with bipolar ions in the charger and rapidly establishes an equilibrium charge state, with a distribution of particles carrying no charge, a single charge, or charges of both positive and negative polarity. Ion charging theory accurately predicts this charge distribution [86][87].

The charged particles are then introduced into the DMA, where they come into contact with an electric field, which generates an electrical force that pushes them into the gas in which they are suspended. Electrical mobility is a measure of a charged particle's capacity to move inside an electrical field; it is a function of the particle's charge state, diameter, and drag force encountered [88]. After exiting the DMA, charged particles are classified according to their electrical mobility; determined based on derived relationships between particle electrical mobility and DMA operating parameters (e.g., applied voltage) [89].
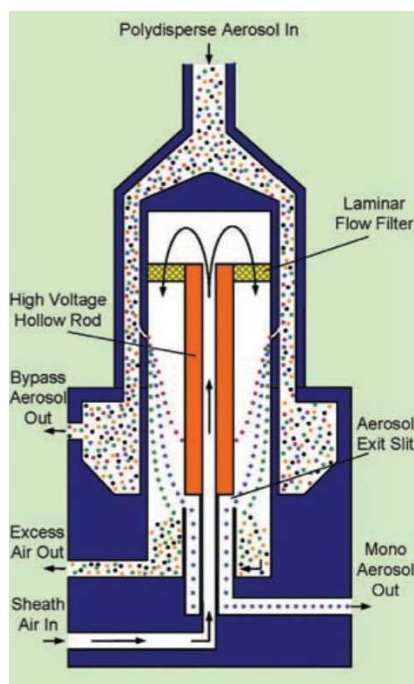
Figure 14. Flow schematic of the Model 3772 CPC [84].

As the instrument's name implies, the CPC's primary capability is to develop sampling particles by working fluid condensation prior to optically counting them. When the vapor around particles reaches a specific saturation point, the vapor begins to condense on the particles; this is referred to as heterogeneous nucleation. However, if supersaturation levels are excessively high, vapor condensation can occur even in the absence of sampling particles; this is referred to as homogeneous nucleation. Working fluid vapor molecules clash and form clusters during homogeneous nucleation. Counting particles in homogeneous nucleation droplets will introduce instrument noise and should be avoided. To obtain optimal CPC performance, a supersaturation level slightly below the homogeneous nucleation limit must be used. The particle size detection limit is a strong function of the operational super-saturation ratio and may be determined using theoretical relationships between particle diameter and vapor supersaturation ratio [90].

3.2 Scanning Electron Microscope (SEM)

During this work Quanta™ Inspect Scanning Electron Microscope by FEI Company equipped with an EDAX EDS system is used. The Quanta Inspect Scanning Electron Microscope is a versatile, high-performance instrument with two modes (high vacuum and low vacuum) to accommodate the widest range of samples of any SEM system [91]. It has resolution up to 10 nm in high vacuum and up to 12 nm in low vacuum with maximum voltage of 3 kV [91]. The SEM works by focusing a narrow beam of electrons on the sample surface. As a result of the impact of the incoming beam, materials emit photons and electrons; the emitted photons can be either X-rays or luminescence. The examination of X-ray photons

created in this manner is referred to as EDS. The electrons emitted are utilized for imaging. The image taken, represents a surface with contrast differences which are derived from the difference energies of the emitted electrons from the material. SEM imaging is classified into two main modalities based on the type of electrons emitted from the sample: (a) secondary electron imaging (SE) and (b) backscattered electron imaging (BSE) [92]. The process of SE and BSE creation is depicted in Figure 15. Thus, when an incoming electron bounces back from the surface and returns towards the electron source, this is referred to as BSE [92]. BSEs may be identical in energy to the entering beam (elastic scattering) or may have lost some of their initial energy (inelastic scattering). On the other side, the incident beam may collide with and dislodge an electron from a material atom, which is then emitted from the surface. The probability of this emission depends on the angle of the surface plane to the incident beam; the smaller the angle, the more electrons are emitted. These electrons are referred to as SE [92]. The incoming beam scatters inelastically in this scenario.
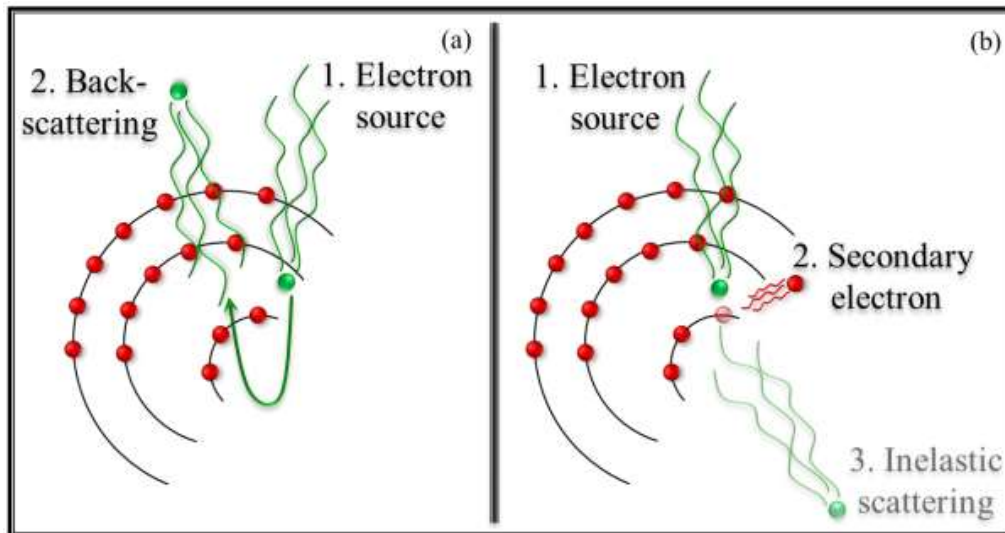

Figure 15. Schematic illustration of (a) BSE and (b) SE generation.

The interaction volume between the incoming beam and the substance matter dictates the depth of emission of electrons (especially BSEs) and photons [92]. The interaction volume is pear-shaped and is proportional to the accelerating voltage and inversely proportional to the sample density [92]. The picture in Figure 16 depicts a typical interaction volume for metals at accelerating voltages of less than 20 kV. As can be shown, whereas BSEs are emitted from portions as deep as 1 μm, SEs are created exclusively in a narrow subsurface zone (1- 50 nm deep). Additionally, Figure 16 demonstrates that Auger electrons can be also generated 0.5-3 nm from the top surface.
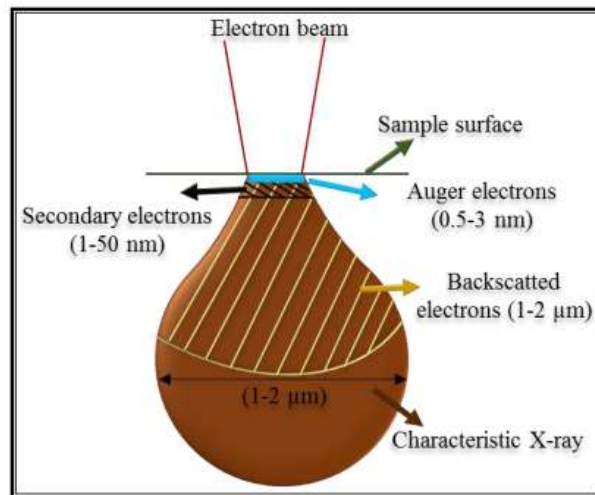
Figure 16. Schematic of the interaction volume excited by a primary electron beam with 20 kV energy.

Due to the fact that SEs are created at a modest depth under the surface, SE imaging provides more detailed topography information than conventional BSE imaging [92]. So, edges and sharp corners produce more SEs than horizontal surfaces, and thus appear brighter in SE micrographs. SE emission from a steep vs a level surface is seen in Figure 17. In comparison to the smooth surface, a bigger proportion of the stimulated volume resides along the sample surface of the steep surface. As a result, more SEs can evade detection at the steep surface. By contrast, BSE emission is sensitive to the density of the immediate sample and causes a chemical composition disparity [92]. In general, the contrast described above is known as Z-contrast [92]. Thus, a material that is heavier (denser) is predicted to produce more BSEs than one that is lighter (less dense) [92].
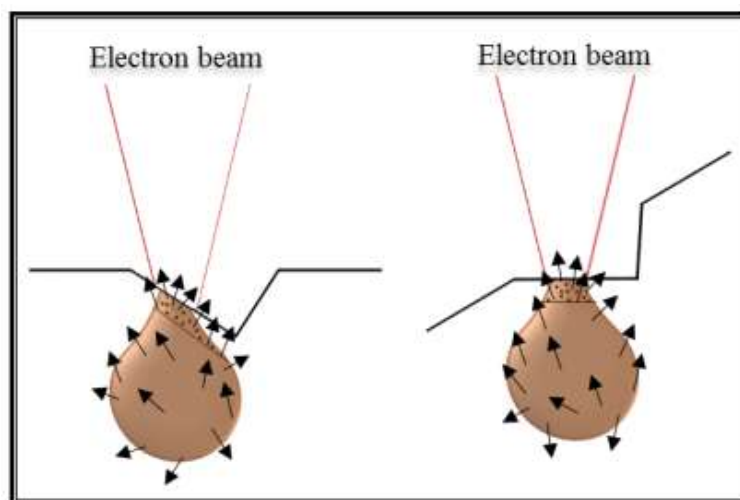

Figure 17. Edge effect on the SE topographical imaging.

36

3.3 Energy Dispersive X-ray Spectroscopy (EDS)

During the current work, an EDS by EDAX detector was integrated into a scanning electron microscope (SEM), allowing for the examination of the local chemical and elemental composition [93]. The specimen was placed at a working distance of 9-12 mm using an electron beam with an accelerating voltage of 15-25 kV [93]. The typical X-ray production caused by electron beam radiation is seen in Figure 18. When one electron is ejected from its position by the beam, another electron from the outer shell migrates to the inner shell to replace the vacancy; in this situation, an Auger electron may be released [94]. Alternatively, X-ray may be generated as depicted in Figure 17 [94]. Characteristic X-rays are emitted from elements when their electrons make transitions between the atomic energy levels [95]. If an electron transitions from a level with energy E_i to one with energy E_j, the emitted X-ray has energy:

$$E_x = E_i - E_j \quad (8)$$

because each element has a unique set of atomic energy levels, it emits a unique set of X-rays which are characteristic of this element [95]. As the atomic number increases the probability of characteristic X-ray emission also increases while that of Auger Electrons decreases [95].
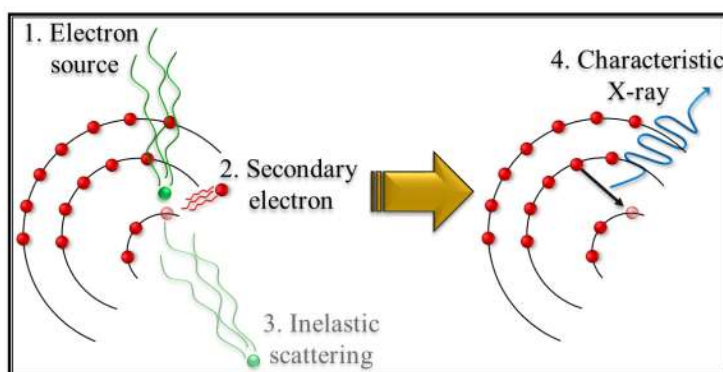

Figure 18. Schematic illustration of characteristic X-ray generation.

3.5 Raman Spectroscopy

Renishaw inVia confocal Raman microscope (6260) (785 nm diode laser, 300mW) was used during present thesis' measurements. Raman spectroscopy is based on the study of the inelastic scattering (Raman scattering) of light from matter, thus detecting characteristic vibrations of its molecules, thus making it possible to identify substances and the content of the individual elements. Advantages of the Raman spectroscopy technique are the examination of samples without any preparation and the direct examination of liquid samples in their containers [96]. A basic principle of Raman spectroscopy is that inelastic scattered light has a different frequency than the original incident radiation. When an incident photon with frequency v_L does not have the necessary energy hv_L, to cause an electron transition, it interacts with a molecule and can be scattered in three different ways: elastic (Rayleigh scattering), in order to retain its original energy and remain at same vibrational level with same frequency v_L or inelastic

with increase or decrease of its initial energy and corresponding new frequency $v_L + v_M$ or $v_L - v_M$. The inelastic scattering with energy loss and corresponding decrease in frequency is called Raman-Stokes scattering, while the one with increasing energy and corresponding increase in frequency is called Raman-AntiStokes. The explanation for the occurrence of the Raman spontaneous phenomenon is presented in the energy diagram of Figure 19 [97]. Initially we consider that the molecular system has two quantum vibrational energy states, the fundamental vibrational state with $n = 0$ and the excited vibrational state with $n = 1$, which differ energetically by hv_M, where v_M is the frequency of the molecular oscillation.

The corresponding transitions to the potential (virtual) states are shown in Figure 19. In Raman-Stokes scattering there is a transition from the fundamental vibrational state to a higher energy vibrational state, while in Raman-AntiStokes we have a transition from a higher energy vibrational state to a lower one. In comparison, the probability of elastic scattering is much higher than the probability of Raman – Stokes and Raman – AntiStokes inelastic scattering occurring, which occur with very small probabilities of one Raman photon per 10^6-10^8 scattered photons [96]. Also, from inelastic scattering, at room temperature, Raman – Stokes scattering is more likely than Raman – AntiStokes, and therefore easier to study. This is because the number of molecules in the fundamental vibrational state is much greater than the number of molecules in some other excited state at room temperature, so that most photons can only excite a normal form of vibration, and therefore they will suffer a reduction in their energy.
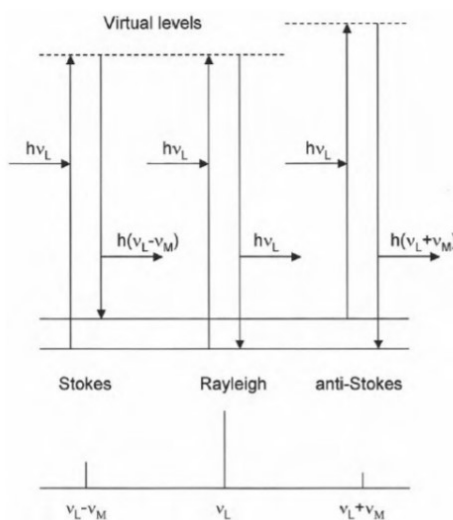

Figure 19. Energy diagram of possible transitions when hv_L energy radiation falls in a two low energy state system [97].

When a molecule of matter interacts with an electromagnetic wave with periodically varying electric field intensities, it is polarized and considered as a vibrating dipole that oscillates like a harmonic oscillator with frequency [98] (Equation (9)):

$$v = \frac{1}{2\pi}\sqrt{\frac{K}{\mu}} \quad (9)$$

where μ is the reduced mass of the system and K, the return constant of the spring, i.e. the vibrating molecule that depends on the characteristics of the bond between the atoms. In quantum mechanics the motion of the molecule is described by Schrödinger's equation [99] for a particle of mass μ at a potential $V = \frac{Kx^2}{2}$:

$$\frac{d^2\psi}{dq^2} + \frac{2\mu}{\hbar^2}\left(E - \frac{Kx^2}{2}\right)\psi = 0 \quad (10)$$

which has solutions

$$E_v = hv\left(n + \frac{1}{2}\right) \quad (11)$$

and vibration frequency [96] given by Equation (9).

The bipolar moment induced in the molecule when it interacts with radiation is equal to Equation (9):

$$p = \alpha E \quad (12)$$

where a is the polarity of the molecule and E is the intensity of the radiation [96]. The polarity tensor of the molecule is written as a function of the positions of the nuclei of the atoms that make it up as a first order approximation as

$$a_{ij} = (a_{ij})_0 + \left(\frac{\partial a_{ij}}{\partial Q}\right)_0 Q_k \quad (13)$$

where Q_k are the k normal vibration variables with corresponding frequencies v_k, while some derivatives are calculated at the equilibrium position [96]. Considering that the electric field of radiation changes periodically as

$$E = E_0 \cos\cos(2\pi v_L t) \quad (14)$$

and that the motion of the nuclei of the molecule is harmonic, we arrive at the following relation for the bipolar moment of the molecule [96]

$$P = a_0 E_0 \cos\cos(2\pi v_L t) + \frac{1}{2}\left(\frac{\partial a}{\partial Q_v}\right)E_0 Q_0\{\cos[2\pi(v_L + v)t] + \cos[2\pi(v_L - v)t]\} \quad (15)$$

The first term describes Rayleigh scattering, the second Raman – AntiStokes scattering and the third Raman-Stokes scattering. From the above relation it is obvious that, in order for a Raman vibration to be active, a necessary condition is

$$\frac{\partial a}{\partial Q_k} \neq 0 \quad (16)$$

that is, there is a change in the polarity of the molecule during the vibration. In fact, according to the above selection rule, intense Raman scattering occurs from vibrations in which there is a greater change in polarization [96].

In a standard Raman measurement (Raman spectrum) the relative intensity of the scattered Raman radiation is recorded as a function of the displacement of the ripple from the excitation frequency. Although radiation is usually characterized by wavelength, in Raman spectroscopy, because the displacement of energy from the original energy of excitation radiation is studied, the waveform (cm^{-1}) is used as the unit of measurement, which is proportional to the energy [96]. A typical Raman spectrum of cyclohexane is shown in Figure 20, where it is observed that the peaks of Raman-AntiStokes scattering are much weaker than those of Raman-Stokes scattering and also that more than one vibration is active in Raman. In general, the number of vibrations possible in a molecule is directly related to the degrees of freedom of the molecule that describe the translational and rotational, if the molecule is not linear, motion. In the general case for a molecule consisting of N atoms the number of possible vibrations will be 3N-6, while for a linear 3N-5. Of these possible vibrations, those that satisfy selection rule (Equation 16) can theoretically be detected [96]. The intensity of the peaks in the Raman spectrum depends on the nature of the vibration but also on the characteristics of the device. If the target sample is a crystalline solid, Raman scattering is associated with lattice vibrations instead of molecular vibrations. For a phonon to be active in Raman, condition (Equation 16) must apply and it depends on the symmetry of the crystal.
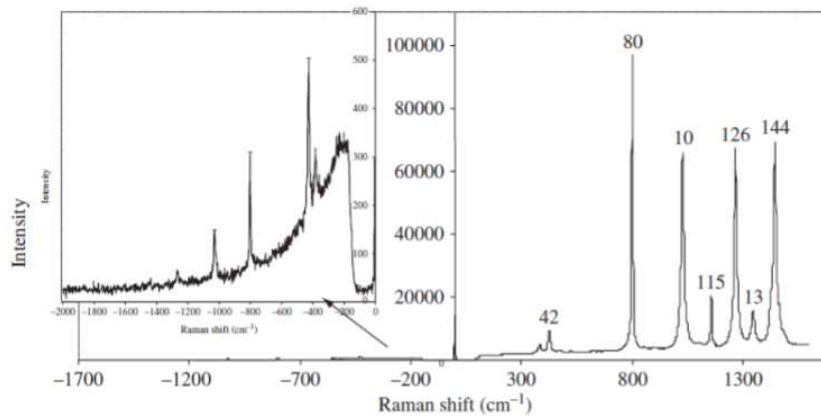

Figure 20. Range of Raman-AntiStokes (left) and Raman-Stokes (right) scatterings of cyclohexane [96].

A typical Raman spectroscopy device is shown in Figure 21 and consists of the following parts: Relatively high power monochrome laser source, optical guides (mirrors) and focus beam (focus lenses), an edge filter before input of Raman scattering radiation in the monochromator, which eliminates Rayleigh scattering radiation in the laser wavelength and allows only Raman scattering to pass through and detect, optical fiber for collecting and transmitting scattered radiation to the monochromator inlet, the

monochromator, detector (usually CCD) and, finally, a computer to control the measurements, display and process the spectra [100].
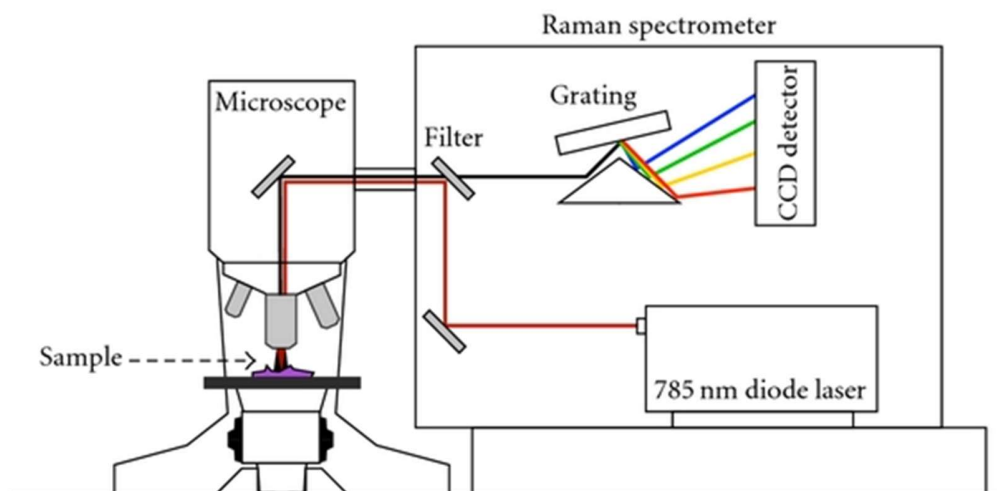

Figure 21. A typical Raman spectroscopy device setup[100].

3.4.1 SURFACE-ENHANCED RAMAN SCATTERING (SERS)

In 1974, during Raman scattering measurements, Fleischmann et al. pioneered surface-enhanced Raman scattering (SERS), initially attributing the increased signal to an increased number of adsorbed molecules due to the increased surface area. Jeanmaire & Van Duyne and Albrecht & Creighton separately identified this phenomenon in 1977 [101]. They both recognized that the extraordinarily strong surface Raman signals could not be explained solely by increased surface area and demonstrated that the increased signals were caused by a true enhancement of Raman scattering efficiency, thereby establishing a new field of Raman spectroscopy, namely SERS. SERS now is one of the most powerful analytical techniques available because it overcomes the inherent limitation of weak signals in standard Raman scattering by magnifying them more than one million times.

The mechanism through which SERS works is by the activation of localized surface plasmons (Figure 22). Surface plasmons (SPs) are coherent delocalized electron oscillations that occur at the interface of any two materials where the sign of the real component of the dielectric function changes (e.g. a metal-dielectric interface, such as a metal sheet in air). Plasmonic materials actively have dimensions smaller than the wavelength of light, leading to a confined oscillation of the electrons in the nanoparticle. Surface Plasmon Resonance (SPR) is the resonant oscillation of conduction electrons at the interface of materials with negative and positive permittivity that is induced by incoming light [102]. SPR is the basis for a large number of industry-standard techniques for determining the adsorption of material onto planar metal surfaces (usually gold or silver) or the surface of metal nanoparticles. This is the essential concept behind a large number of color-based biosensor applications [102].
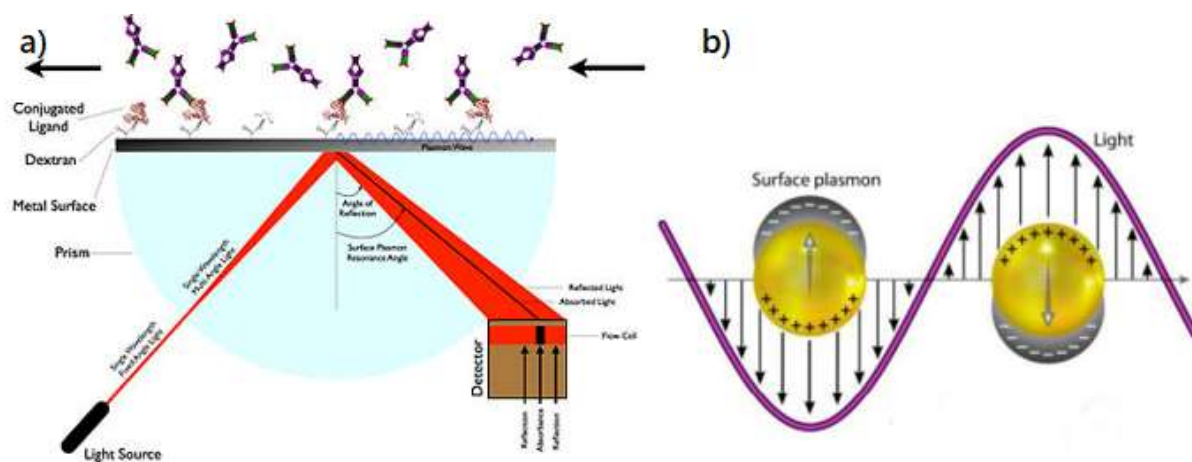
41

Figure 22. a) surface plasmon resonance (SPR), b) Representation of the localized surface plasmon on nanoparticles [102]**.**

4. RESULTS AND DISCUSSION

From previous thesis works [103], [104] it is known that the SDG from Fasmatech produces three types of particles in aerosols. Type i: the small "primary" nanoparticles of diameter <10 nm. Type ii: clusters of the primary particles with particle electrical mobility diameters that range between 10 and 100 nm (reaching a maximum in the range of 15-30 nm); these clusters have a fractal morphology, as has also been evidenced in the TEM. Type iii: larger spherical particles with sizes over 100 nm. The results presented in the current thesis confirmed the previous observations and helped to explain their various details that appeared there. Figure 23 shows TEM images of all these types of particles, as captured on TEM lacey carbon (fibrous support films). Type i and iii particles do not appear in any of our SMPS size distributions due to the limited resolution of the specific setup of our instrument, using the 1 Lt DMA column. They were seen only with Electron Microscopy techniques. We believe that below the SMPS's resolution of 10 nm, the distributions reach a new maximum, because in our TEM data we see far more type i particles than any other type, even though particles accumulate on our TEM fibers; this can be confirmed by others, see eg [43]. It is worth repeating here that all our depositions (incl. those on the TEM samples) are done at a much closer distance to the SDG than the SMPS measurements. This means that the SMPS is expected to measure the clusters when they are slightly larger in size and less in concentration than what we are actually using for our depositions; of course, it still gives us an excellent view of the aerosol's nature on the actual location of our depositions.

The purpose of the experiments that follow, is to analyze and standardize the type, quantity and concentration of the particles produced in order to use the SDG as a stand-alone particle generation device (without the costly SMPS) so that we can make a large number of depositions. Thus, the goal is to calibrate the spark setup and focus on the optimum parameters where the maximum number of primary particles are generated for each material, study the depositions and apply them in applications. Therefore, in this work, the study is not focused on the exact mechanisms of the formation of the various types of particles, as this would require resources that were not available; instead, it is focused on the repeatability of the particle production, aimed to enable us to use, eventually, the SDG as a "black box" that produces certain distributions of aerosol particles.
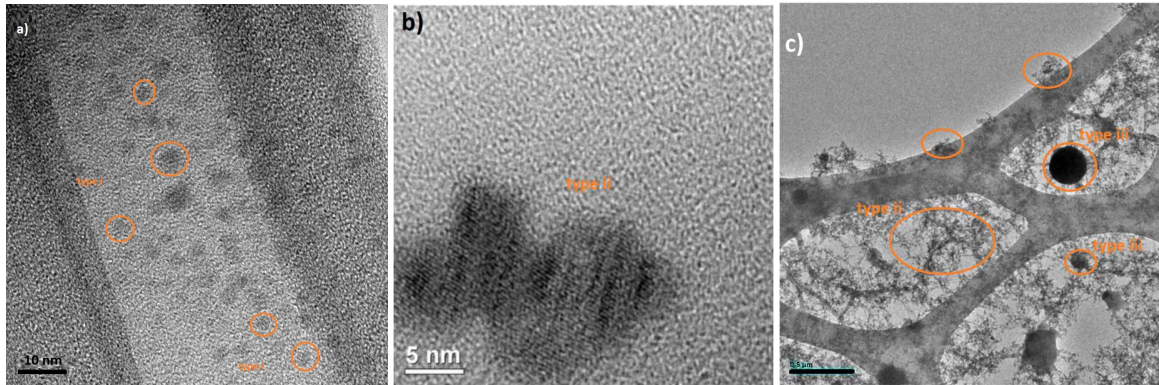
4.1 Spark Properties and Electrode Erosion

In a typical, unregulated or free-running SDG, an oscillatory discharge forms after the breakdown occurs between the electrodes. When spark repetition rate (SRR) (i.e., spark frequency) is increased, at a certain point normal sparks start to be followed by smaller (secondary) sparks, which use the remains of the conductive plasma channel generated by the first big spark. In fact, under these conditions one might actually see different separate spark channels in the spark area between electrodes; usually one large channel at the side of the electrode closest to the incoming gas flow, and further away from that side many thinner sparks, as illustrated in the schematic of Figure 24. As SRR is increased to even larger values, the amount and discharge voltage of the large sparks is expected to be reduced further and further, while the number of secondary sparks increases. Eventually, only very small sparks occur. In the SDG from Fasmatech that was used during this work, the ultimately existence of small secondary sparks caused problems to both SDG's smooth operation and particle generation, as they were neither efficient nor reproducible.
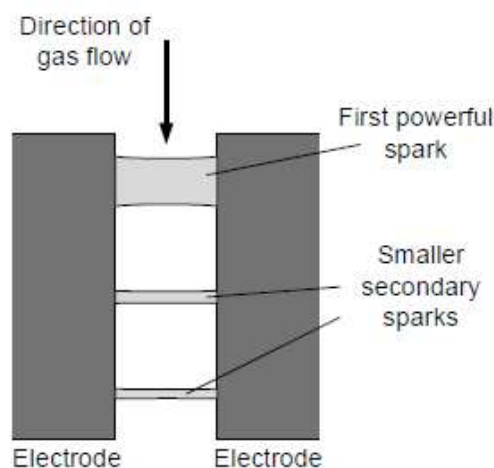

Figure 24. schematic of observed evolution of sparks [82]

44

In order to ensure SDGs efficiency and reproducibility, the powerful discharges should be regulated and stable at all times. A relatively high discharge voltage is the consequence of the high capacitance, low resistivity and low inductance of the circuit, which are essential for the efficient erosion of the electrodes, when NP production is targeted [82]. The spark energy (or energy per spark) and the SRR are the two most essential process parameters of the SDG that are affected by the electric circuit. These values may be efficiently controlled by modifying the R_{ch}, R_{dis}, and C components of the discharge as can be seen in the Figure 25 of the SMPS size distributions; dN/dlogDp is the normalized total particle number concentration shown against the mobility diameter.

By altering the electrical parameters, it is possible to optimize the circuit in the control panel, so that strong and intense sparks are obtained permanently. The best spark performance was found to be for the maximum possible capacitance C=1.94 nF, charge resistance R_{ch}= 100 kOhm and discharge resistance R_{dis}=0 Ohm.

Effect of Changing the Circuit Parameters

Legend:
- R_{dis}=470 Ohm, f=50Hz, C=1nF
- R_{dis}=0 Ohm, f=20Hz, C=1nF
- R_{dis}=0 Ohm, R_{ch}=100kOhm, C=1nF
- R_{dis}=0 Ohm, R_{ch}=0 Ohm, C=1nF
- R_{dis}=0 Ohm, R_{ch}=100kOhm, C=1nF
- **R_{dis}=0 Ohm, R_{ch}=100kOhm, C=1.94nF**

V_{max}=4kV
Flow=3L/min

x-axis: Particle Electrical Mobility Diameter [nm]
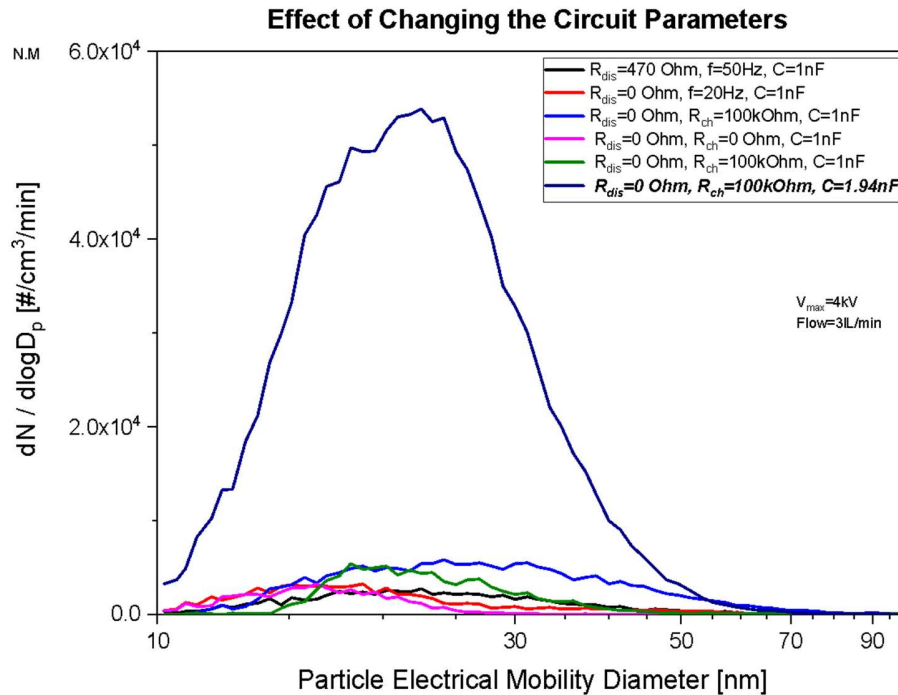y-axis: dN / dlogD$_p$ [#/cm^3/min]

Figure 25. SMPS data of how electrical parameters affect the particle production efficiency (Cu electrodes were used).

Varying these parameters during the everyday operation of a NP generator is not realistic in our setup. The parameters that are more easily tuned so that we modify the SRR (f) and spark energy, referred now on as control parameters, are the distance between the electrodes, the carrier gas (N$_2$) flow rate [105] and the input voltage (V_{in}).

4.1.1 EFFECT OF CONTROL PARAMETERS

After the optimum electrical parameters of the circuit were found (and remain permanently as fixed values for the rest of this thesis work), experiments were performed with copper electrodes to see how the variable control parameters (electrode distance, input voltage and carrier gas flow rate) could affect particle production. From previous works [104], [106] it is already known that copper is oxidized and CuO type i and type ii particles are produced, while type III are in their larger part Cu particles (with a thin CuO on the surface) (Figure 26). The oxidation of copper occurs because there are always remains of the atmospheric O2 in the spark chamber. Another source of O2 could be the fact that industrial N_2 is used as carrier gas (purity 99,99%, water vapor ≤25 ppm, oxygen ≤ 10ppm) instead of extra pure. Then, the electrodes are replaced with gold, platinum and palladium, with which respective measurements are repeated. The aim is to make a comparison between the materials and to understand whether the changes in these parameters affect the production of particles in the same way.
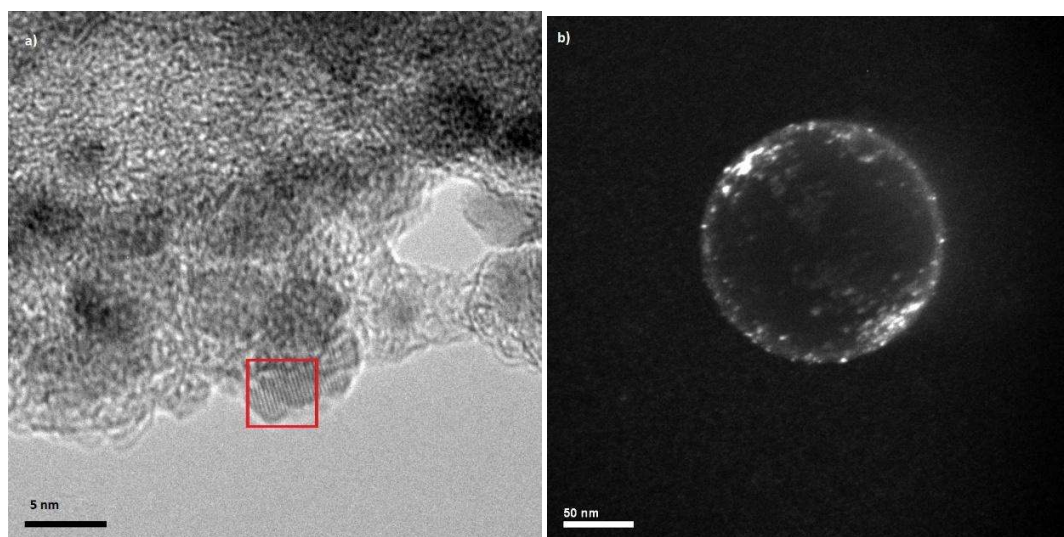

Figure 26. a) TEM High resolution image of lattice planes with a distance of 2.52 Å, corresponding to the CuO tenorite phase (Cu102) and b) dark field TEM image of type iii spherical CuNP decorated with type i CuO NPs.

4.1.1.1 Effect of Electrode Distance

As was seen in previous work [103], [104] and mentioned also above, there is not much influence of the control parameters in the nature of the primary (type i) particles. Therefore, the main aim becomes finding the optimum parameters for maximum NPs production, i.e., control their concentration in the produced aerosols in order to tune the size of type ii particles (clusters), for their successful use in applications. One of the main parameters that can be tuned is the electrode distance. While keeping the other parameters stable, SMPS measurements were performed with the four different electrode materials (Cu, Au, Pd, Pt). As seen in Figure 27, there is not a general rule that one has to follow in order to reach maximum particle numbers; the various electrodes are reaching their maximum particle production under different, yet repeatable, parameters; it can be seen that the maximum number of particles for Cu is

$3.8 \times 10^6 \ cm^{-2}min^{-1}$ ($f = 352 \ Hz$, $d_m = 22 \ nm$), for Au is $1.8 \times 10^6 \ cm^{-2}min^{-1}$ ($f = 32 \ Hz$, $d_m = 32 \ nm$), for Pd is $1.4 \times 10^7 \ cm^{-2}min^{-1}$ ($f = 40 \ Hz$, $d_m = 14 \ nm$) and for Pt is $8.0 \times 10^6 \ cm^{-2}min^{-1}$ ($f = 125 \ Hz$, $d_m = 18 \ nm$).

From these graphs we can get some very clear signs of what is happening during the particle formation. As the distance between the electrodes increases, the SRR drops, affecting the energy of the spark and therefore particle generation. This is happening because higher electrode distances produce sparks in higher V_{dis}, and therefore the capacitor needs more time for recharging, in qualitative agreement with Paschen's law (Equation 1). It is also observed, that for larger type ii (clustered particle) concentration, there is a shift towards larger cluster sizes; this can be explained by the fact that the denser particles there are in the aerosol, the larger is the possibility to collide with each other and stick, creating larger clusters. In the case of copper, the concentration of the generated particles decreases as the electrode distance increases, as predicted by Lehtinen's et al. (2002) model [107]. However, gold seems to have the opposite behavior. This phenomenon is depicted in Figure 28 for copper and gold electrodes. Palladium and platinum do not appear to have unambiguous behaviors. More details and comparison of how the electrode distance affects the particle production in different electrode materials are given in Appendix A.

In further analysis, it is observed that, for smaller numbers of produced particles, more noise appears on the distributions; this has to do with the sensitivity of the measurement technique. In the case of copper, distributions are substantially noisier than those of other materials, for similar particle concentrations and sizes. This may be caused by the formation of oxides on the electrodes, which result in a structural and also electrical inhomogeneity, as CuO is less conductive than Cu. Additionally, it can be seen that sparks in palladium and platinum occur in higher V_{dis}, in smaller electrode distances, and distributions seem to be shifted to smaller type ii particle sizes, compared to the other two materials. These are clear effects of the electrode material properties, such as their melting points, their hardness, etc. It is worth noting here that gold melts at 1064 °C, copper at 1085 °C (CuO at 1326 °C), palladium at 1555 °C and platinum at 1768 °C; according to the Mohs Scale of Hardness, gold has a value of 2.5, copper of 3, platinum of 3.5 and palladium rises up to 4.75. The harder materials, with higher melting points, do not produce enough metal vapor in the first few sparks, and therefore there is not enough conductance in the channel between the electrodes (see also paragraph 4.1); the Vdis has to reach higher values in order to start the normal operation of the charge-discharge circuit and the spark repetition.

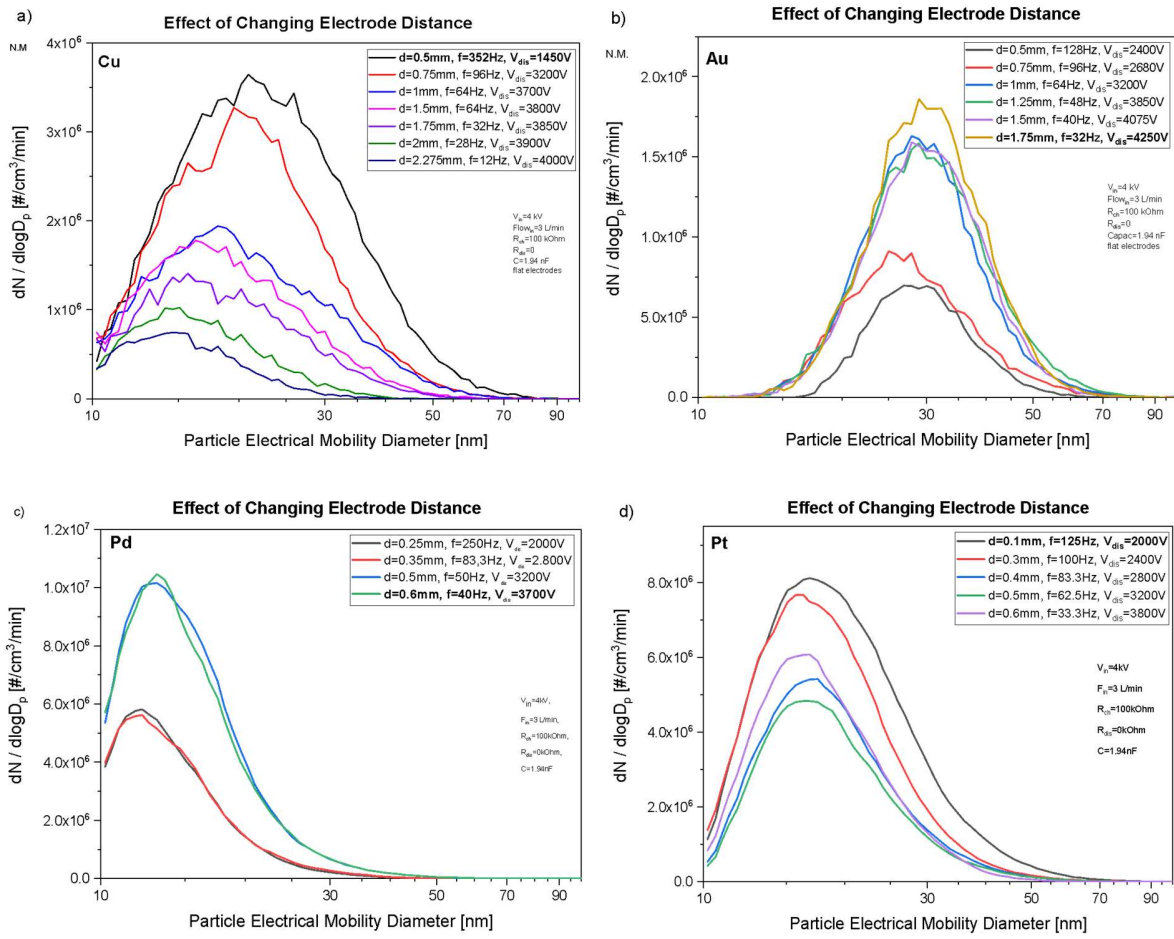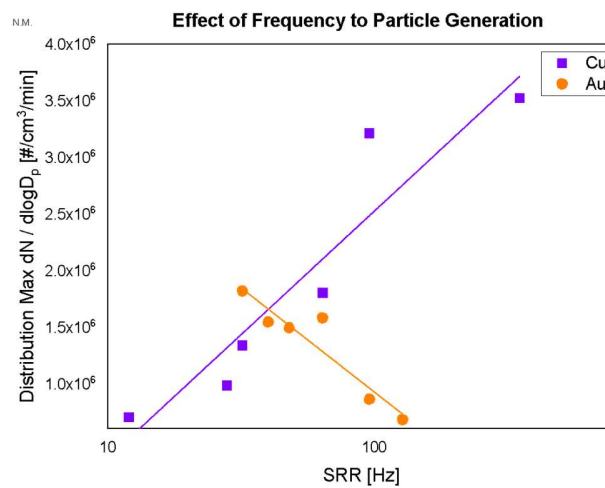**Figure 27. SMPS data of how different electrode distance affects particle production.**

Figure 28. SDG particles produced concentration vs SRR with Cu and Au electrodes, while altering electrode distance.

48

At a constant pressure and electrode geometry (rods with flat surface), the electrode distance is the parameter that predominantly affects the breakdown voltage [43], thus the spark itself, hence it can be used to vary the spark energy according to Equation (3). Figure 29 shows the relationship between the electrode distance and spark power, as well as power per spark, for various electrode materials, based on the SMPS data of Figure 27. Assuming that the overvoltage is small, the breakdown voltage is replaced by the discharge voltage. The spark power increases with the increase of the distance between electrodes both in general and in every single spark.
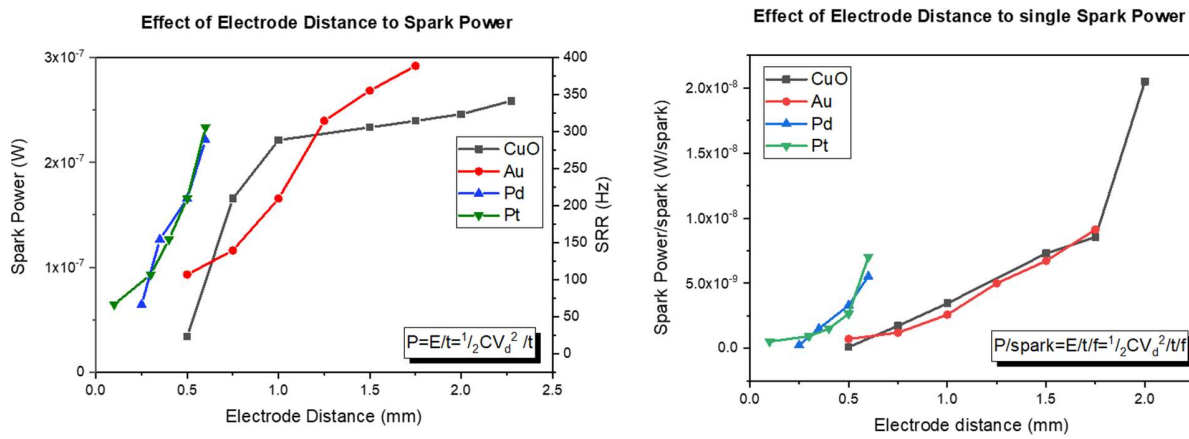

Figure 29. Spark power (left) and power/spark (right) at different electrode distances under N_2 carrier gas.

4.1.1.2 Effect of input voltage

Continuing the experiments, measurements were made during the alteration of the input voltage with all four materials, as shown in the distributions of Figure 30. In all electrode materials, the behavior of spark and particle production seems to be corresponding. By increasing the V_{in}, V_{dis} shows only small changes, while at the same time the density of the produced particles increases according to V_{in}'s increase. It is clear that the more energy is given to the system, the more material is evaporated from the electrodes and the more particles are produced. This effect is clearer in the case of Cu and Au where there is a wider range for parameter tuning, while in the other 2 electrodes, the Vdis reaches a maximum level in relatively small electrode distances.

The main difference, between the various electrodes, observed here is that the density of the gold particles can be four orders of magnitude larger than that of the other three materials; as seen also before, Au is easier to evaporate in these conditions. Moreover, the increase of input voltage causes a right shift of size distributions; in case of Au the shift is stronger due to the larger particle production that causes more agglomeration into clusters, before dilution in the aerosol by the carrier gas.

As it has been confirmed by previous work [106], during the spark with copper electrodes tenorite copper oxide particles (CuO) are produced; the latter condition results in the formation of oxides not only as

separate nanoparticles but also located on the surface of the electrodes thus making them less conductive and preventing the unimpeded production of particles (Cu melting point: 1085 °C, CuO melting point: 1326 °C). The Cu electrode oxidation is studied in detail below, in a separate paragraph. Electrode oxidation may also explain the fact that Cu, although it has a similar melting point and hardness to Au, is producing much less particles.
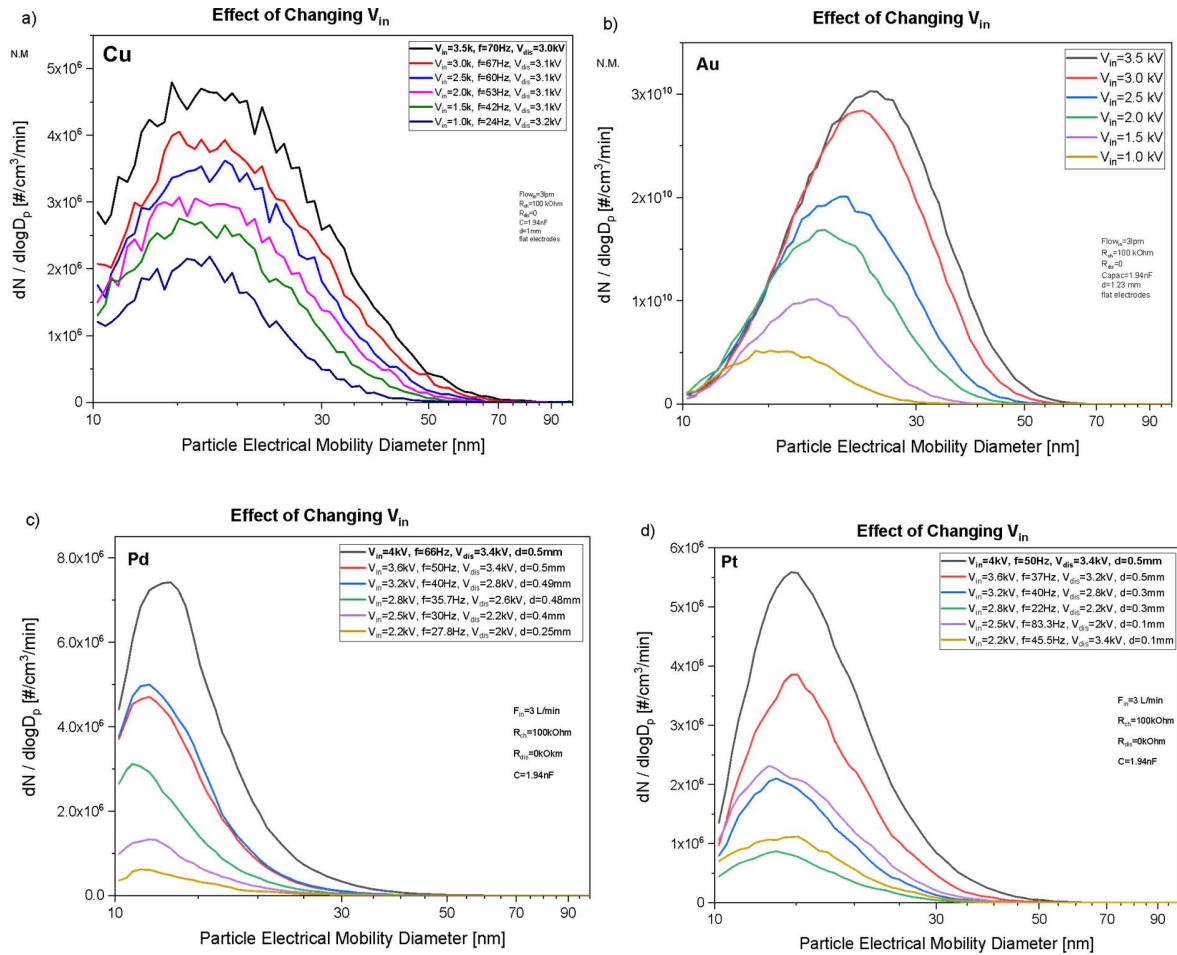

Figure 30. SMPS data of how input voltage affects particle production.

4.1.1.3 Effect of carrier gas flow rate

Last varied control parameter was the carrier gas flow rate. The spark characteristic is highly sensitive to the gas composition [108]. Tabrizi et. al. (2009), after multiple measurements, concluded that nitrogen as a carrier gas is ideal because the results of V_{dis} are almost entirely consistent with the theoretical approach (Paschen's law), in contrast to other gasses such as helium, argon and atmospheric air [43]. In addition, the use of N_2 as a carrier gas allowed the maximum possible production of nanoparticles (or alternatively the maximum erosion of the electrodes) so we chose this for our work.

During the spark, the evaporated electrode material travels into the spark gap in the form of a jet, which is observable via the created plasma [109]. According to Figure 31, SRR seems to decrease while the flow rate increases. This is due to the expansion of the length of arc (Figure 32). This causes the ions to travel longer distances (with the same speed), resulting in less charge transferred per time unit (and therefore reducing the SRR), lowering the probability of aggregation [75]. In this way, coagulation is avoided by fast turbulent dilution of the primary particles in the plasma area [33].
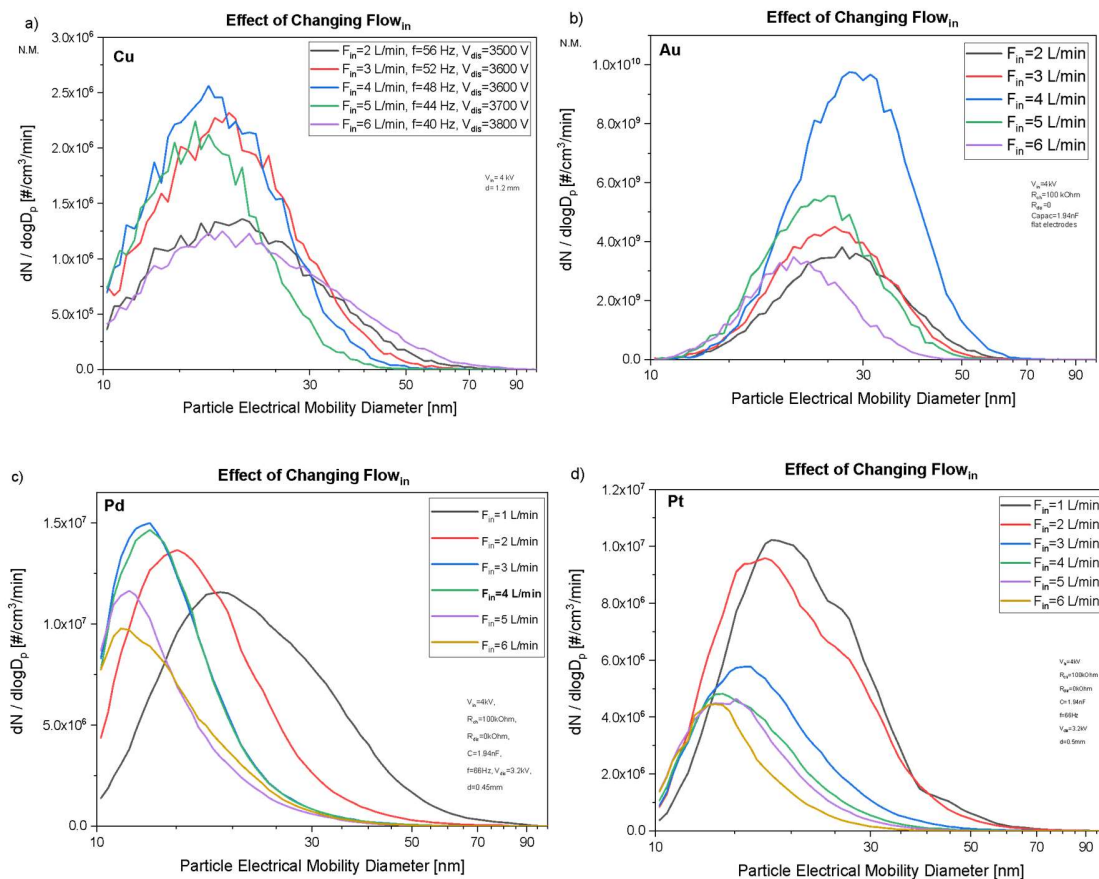

Figure 31. Determination of optimal carrier N_2 gas flow rate (liters per minute) for the best performance of spark (energy and SRR) seen through the difference in concentration and size of copper oxide nanoparticles produced (SMPS Data).

It is worth noting that the alteration of the flow rate does not seem to significantly affect the spark's SRR and V_{dis}, not as significantly as the other control parameters do. While the SRR is inversely proportional to the increase of the flow rate, the discharge voltage appears to behave in proportion to this change [33]. The SMPS data shows that more clusters of all sizes are generated as the flow rate increases up to 4 L/min, and then they eventually decrease (after 5 L/min). Coagulation prevents larger number concentrations and leads to an increase in the size of the agglomerates. As discussed also above, the number of type ii particles (clusters) has to do with how many are the primary particles and how close they are to each other. In principle, more particles are produced with more metal evaporation. This process can be aided by the increase in the carrier gas flow, when we are at a relatively low flow rate, because in this way more

metal vapor escapes from the area between the electrodes. When there is too much carrier gas flow, the electrodes will be cooled by it and their evaporation will be less. These two conflicting results of the increase of the carrier gas flow rate are, as we believe, the reasons for observing a peak near 4 L / min of our SMPS data [43].
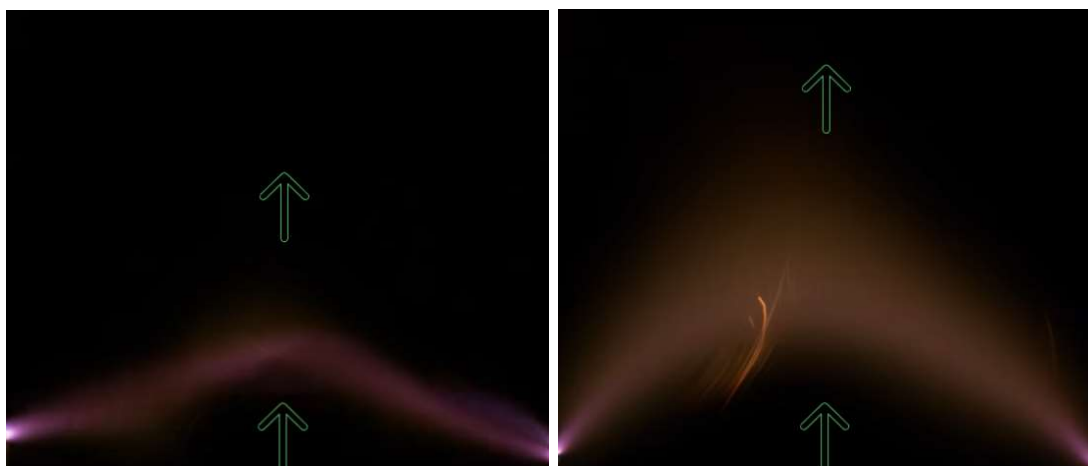

Figure 32. Spark Discharge plasma geometry with 2 L/min (left) and 6 L/min (right) flow rate; flow direction is pointed by the arrows.

More details and comparison of how the control parameters affect the material production in different electrode materials are given in Appendix A.

4.1.2 MORPHOLOGY OF ELECTRODE SURFACE AFTER SPARKING

In order to be able to better understand the particle formation process, one also needs to know what happens to the electrodes during spark and how it affects them. For studying the effect of corrosion on the surface morphology, electrodes were exposed to sparking. The electrodes employed in this investigation were Cu and Au (as representative of noble metals that avoid oxidation) rods, 1 mm in diameter.

The morphology of the electrode surfaces before and after sparking was studied using Scanning Electron Microscope (SEM). As can be seen in Figure 33 the electrode before spark (left) shows to be full of polishing lines; these scratches distributed on the surface were formed during the cutting and wheel polishing procedure.
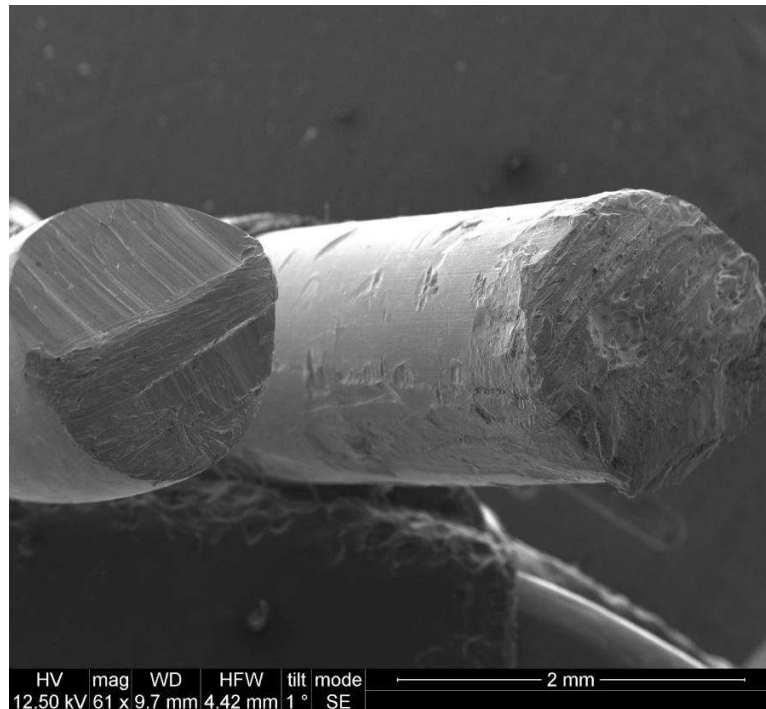
Figure 33. SE SEM image of copper electrodes before (left) and after (right) spark.

4.1.2.1 Before Spark

Before sparking, EDS measurements were performed on the intact electrode (Figure 34) at different magnifications and spots. The electrode seems to be pure copper, clean of contaminations; only a very insignificant amount of carbon seems to exist, which is probably residue of the polisher.

Figure 34. SE SEM image (left) and EDS analysis (right) of polished copper electrode before spark.

4.1.2.2 After Spark

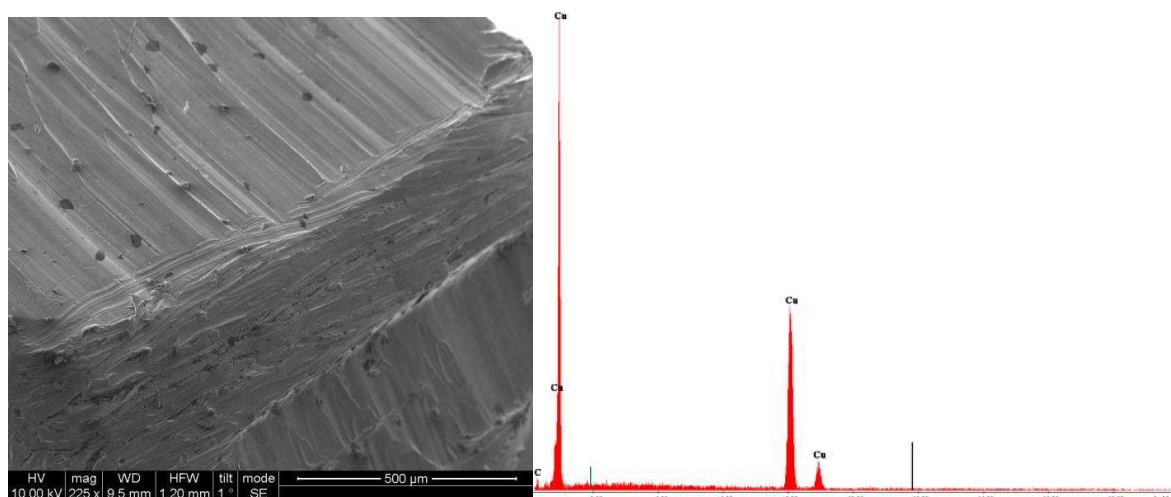After sparking, the electrodes were studied with SEM and EDS. The detailed investigation of the electrode surface exposed to spark reveals three, well distinguishable characteristic parts of the growing microstructures, namely "craters" (a), "undulated areas" (b), and "grainy areas" (c).

4.1.2.2.1 Cu electrode

Low Magnification

Craters

Craters are the most abundant surface feature produced, even by a single spark; even during a single oscillatory discharge, multiple craters are formed on the surface. Craters are characterized by a roughly circular central recess surrounded by a protruding rim of distinctly molten appearance (Figure 35). Micropoints and strands of metal on the rim indicate a fast movement of molten material with subsequent rapid re-solidification. Individual craters often occur in the vicinity of each other, sometimes leading to a cluster of overlapping craters. The latter appearance is more typical for larger craters, while small craters are usually scattered with some distance between them. The depth of the craters is always significantly smaller than their radius, and craters can be described as hemi-ellipsoidal in shape. The appearance of craters does not show polarity dependence, i.e. both anodic and cathodic electrodes exhibit similar morphology.
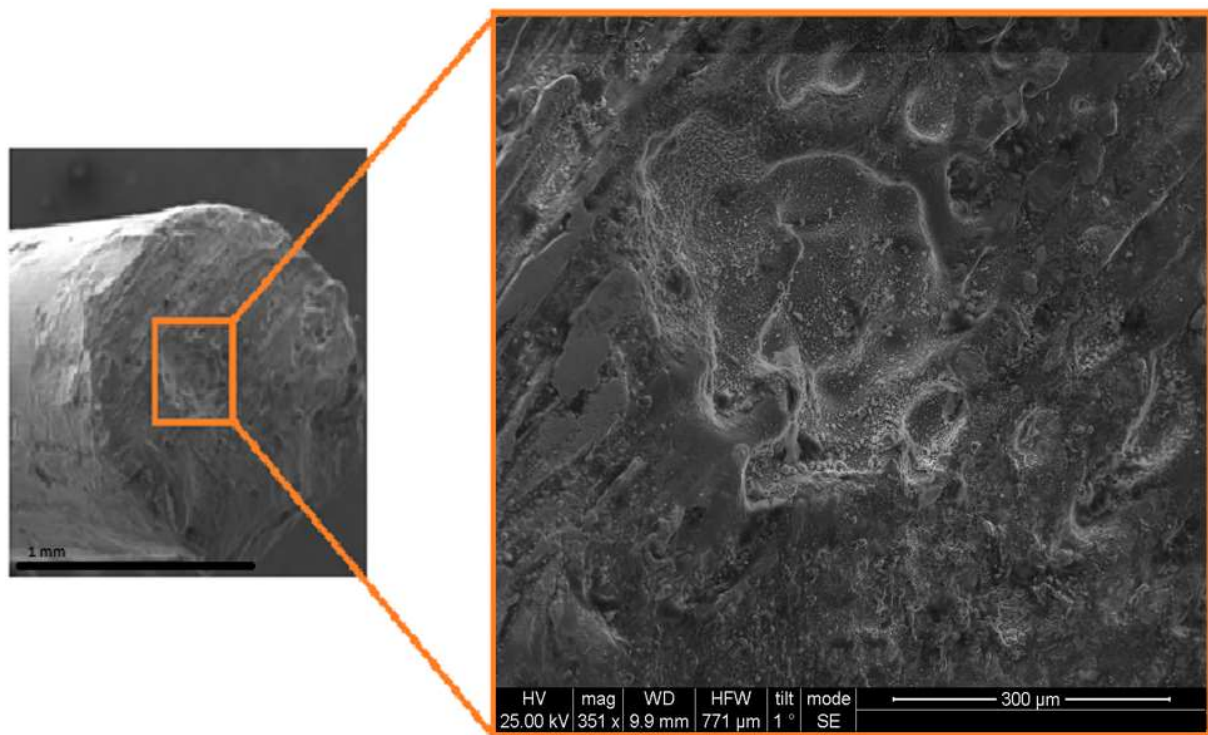

Figure 35. SE SEM image of craters on sparked copper electrodes.

Undulated areas

Undulated areas are formed on the sides of the electrode. This surface feature is characterized by a coherent area of characteristically undulated or wavy appearance, in which pre-existing surface features (e.g., scratches) as well as craters appear to be smoothened (Figure 36). The creation of these undulated areas homogenizes the morphology of the surface they cover, including other features, e.g., scratches and craters. According to the EDS analysis, these areas are located mainly to the sides of the electrode and are eroded, but not oxidized at all.
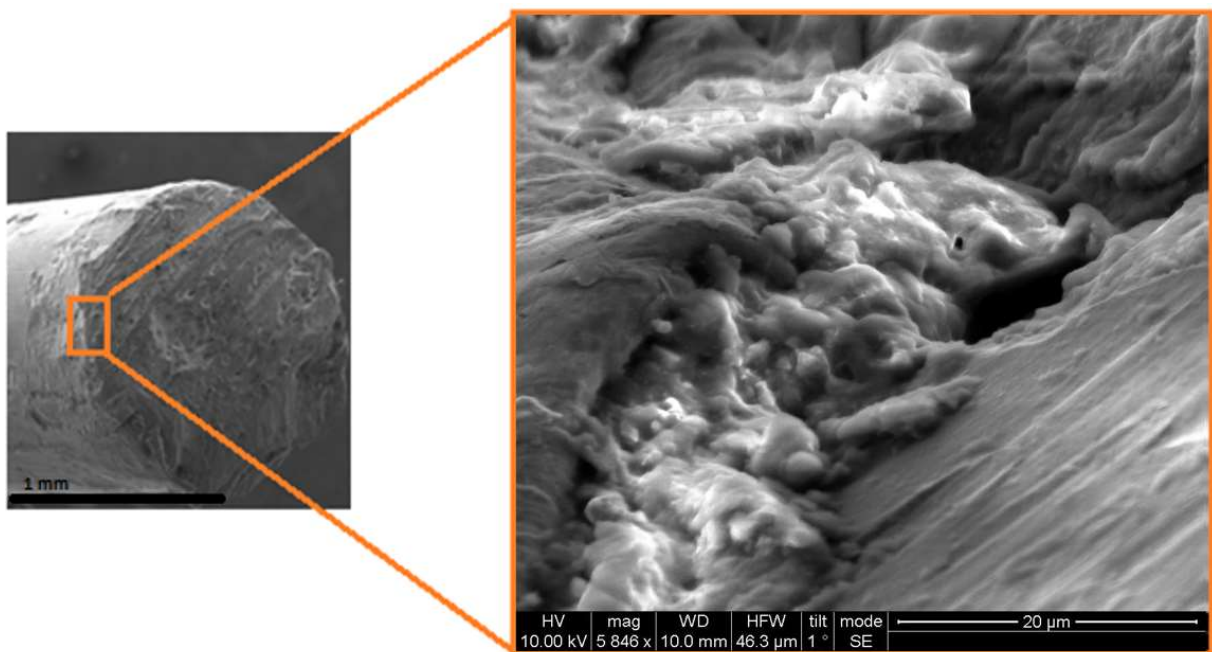
Figure 36. SE SEM image of undulated area on sparked copper electrode.

High Magnification

Grainy areas

When going to higher magnifications in SEM, grainy areas are observed (Figure 37). This morphological feature can be described as a large coherent area within each crater. The small inhomogeneities are stacked on top of each other forming clusters like grains (with a diameter of 50 nm - 1.5 µm). The grainy areas constitute a product of melting and resolidification of the metallic material on the surface of the electrode.
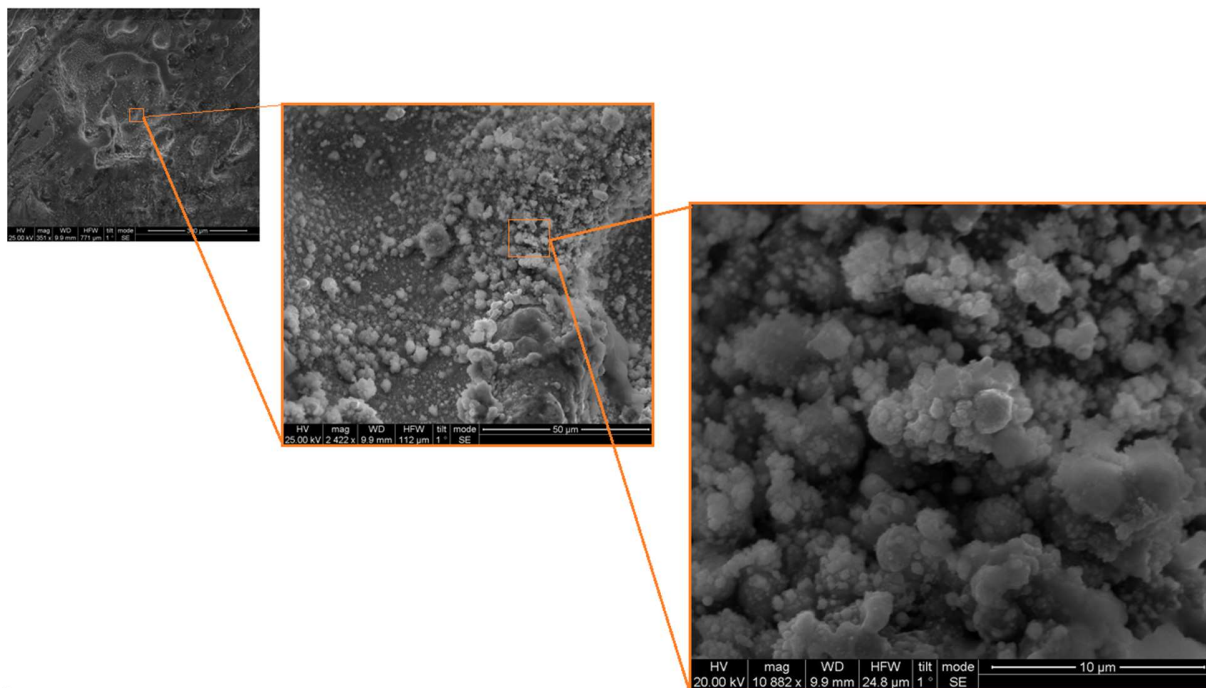
EDS measurements in different spots of grainy areas inside the "craters" of the sparked electrode, showed high concentration of copper oxides, as the presence of oxygen is evident, according to Figure 38 below. This may be one main reason for the decrease of NP generation mentioned in the previous section, as the oxides cover the surface of the electrode. This means that the CuO found in our aerosols most probably originates from this area and that it is not entirely a product of the oxidation of the nanoparticles while they are in the aerosol. Of course, both phenomena may well take place on the same nanoparticle production process. The presence of O in the SDG chamber is not surprising; one of the main reasons for

using vacuum systems for materials depositions is the need to remove as much as O as possible from the processes. Another notable result is that a considerable amount of carbon is also observed.
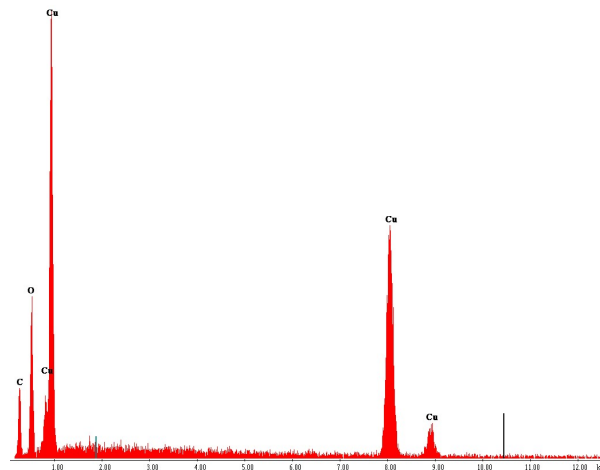
Figure 38. EDS analysis reveals copper oxides on grainy areas of sparked copper electrodes.

Finally, in Figure 39 is shown a flat section of the sparked copper electrode as well. It is observed that the distribution of grainy areas (thus copper oxides) is not uniform throughout the surface but differs significantly from point to point, depending on where the spark has occurred.
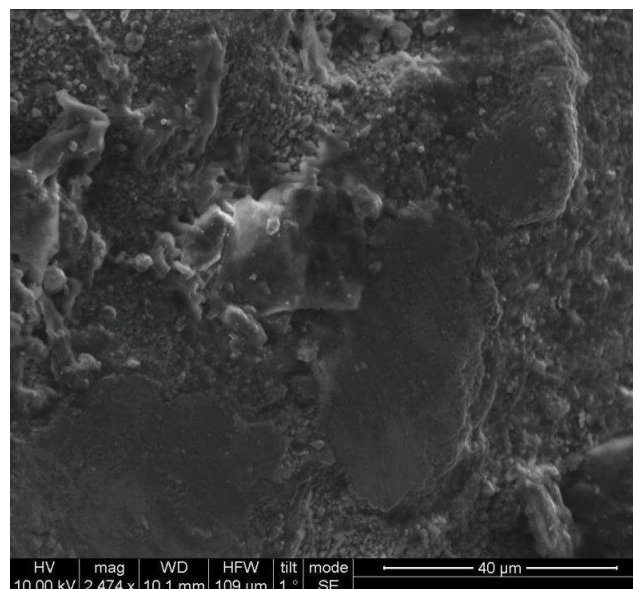
Figure 39. SEM image distribution of dendritic areas with CuO$_x$ on sparked electrodes.

4.1.2.2.2 Au electrode

Corresponding morphology and corrosion are also observed in the gold electrodes. Craters and grainy areas are formed here as well, with the difference that in the latter there is a sudden presence of carbon (Figure 40).
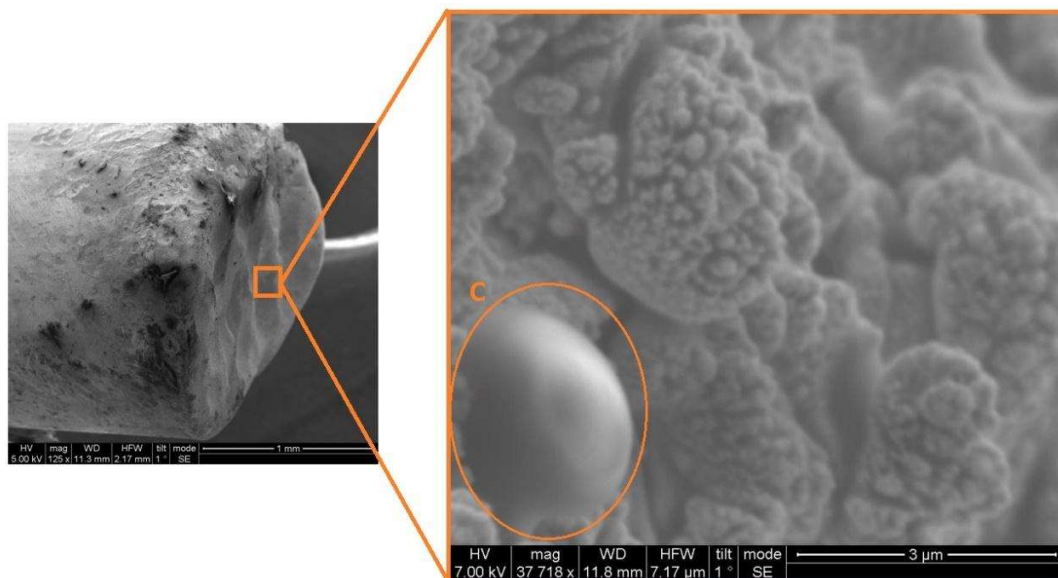
Figure 40. SE SEM images of corroded Au electrodes with craters (left) and grainy areas (right).

It is also worth noting that type ii and type iii particles observed, after the corrosion of the electrode, have a spherical shape with diameter 20 nm – 3 µm, as shown in Figure 41.
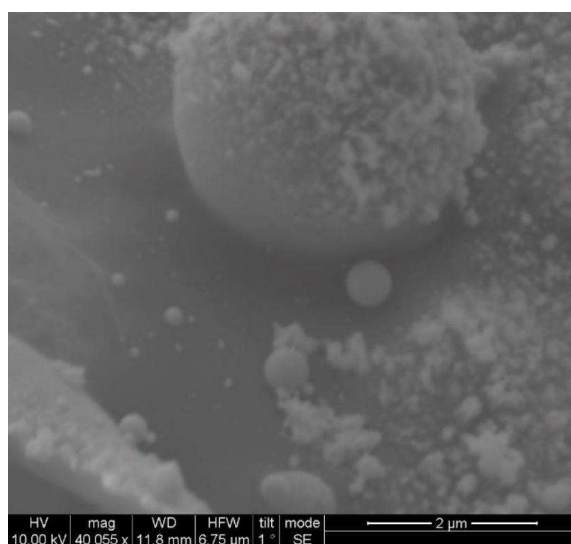
Figure 41. SE SEM image of spherical type ii and type iii particles produced during spark on Au electrode.

4.1.2.2.2.1 Carbon Deposition on Electrodes

The presence of carbon on the electrodes (Figure 42) suggests that the environment of the spark chamber and electrodes is contaminated, resulting in its deposition on the electrode surface. Carbon nanoparticles are regularly produced from graphite electrodes [111] so we can assume that some of the particles that we have measured by the various techniques may consist of C. There is no easy way to find out to what extent this happens; in TEM images and the various spectroscopies used we cannot exclude this, as we deposit in C or C-containing fibers. It is clear however that our metallic and oxide nanoparticles are there and that they present all the properties that you would expect from pure (C free) nanometals and oxides (plasmonic response, CuO EELS peaks etc).

It is worth noting here that in SEM images, small C particles cannot be seen, and that carbon is imaged with a great difficulty, because electrons pass through it, due to its low density (esp. compared to gold), making it impossible to see its surface structure; carbon roughness could be imaged only with the significant reduction of electron beam voltage.

It is reasonable to assume that part of the particles produced and measured with SMPS are C as well. In order to understand this better, we need to perform more experiments that go beyond the scope of this thesis.
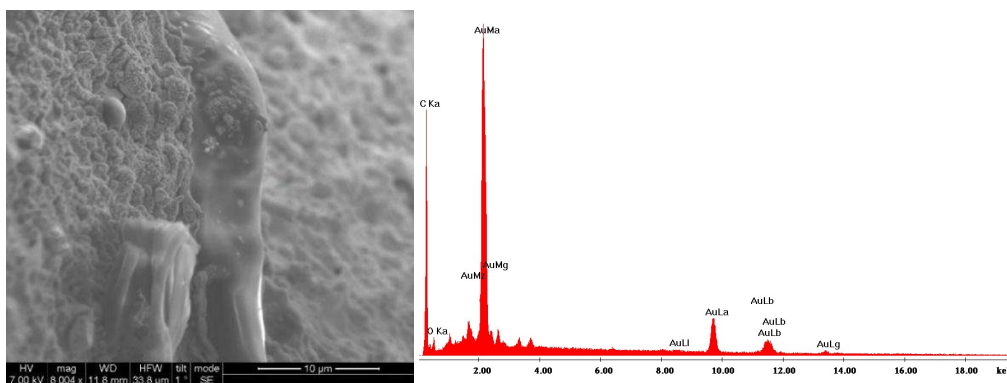
Figure 42. SE SEM image (left) and EDS analysis (right) of carbon findings (smooth surface) on sparked Au electrode.

SUMMARY AND FURTHER DISCUSSION

In the above experiments, SMPS on-line in-situ measurements are performed during the variation of the control parameters with electrodes of Cu, Au, Pd and Pt, in a first attempt to tune the function of the device and also to understand the conditions that affect the particle production in the SDG. The SDG's operation was greatly improved by connecting it to an oscilloscope, for the continuous monitoring of the SRR and the V_{dis}, in order to be able to maintain the repeatability of the experiment without the need of SMPS.

For clarity reasons, only a limited number of SMPS size distributions has been presented here, while many more were recorded during this work. Due to the 1 lt DMA column connected to the SMPS setup, only

particles with size of 10-100 nm could be detected; this size refers to their "electrical mobility diameter", which is a very good approximation of the actual size. According to Vons (2010), even without knowledge of the primary particle size d_{pp}, as a general trend, it is safe to say that information about the quantity and behavior of type i NPs can still be obtained by the SMPS data [82].

By stabilizing the circuit parameters, better control of the experimental spark setup was obtained. Subsequently, by altering the control parameters information was obtained generally on the particle production. The more nanoparticles are produced, the more the size distributions are shifted towards larger particle sizes, as more type ii clusters are created. In a more detailed view of the results produced by the 4 different electrode materials, it seemed that palladium generates in general smaller ii particles than other materials. Moreover, gold generates the most particles. Further study of the Cu and Au electrodes by SEM, showed the morphological changes that take place on the electrode's surface after sparking. CuO is detected on copper electrodes. As a result of the O2 presence, the type i primary particles produced are entirely CuO, while only the type iii particles seem to follow Vons's core cell theory [82]. C is found on both electrodes, and especially on gold.

Eventually, it was observed that the various parameters may affect in a different way the particle production from the various electrode materials. Hence, the attention turns to the investigation of other parameters (capacitor charging current and material properties), in order to see if there is any correlation between them in the different behavior, during the production of the material.

Vons (2010) supports that, in general, increasing current also increases particle production [82]. However, both in his own work and in the present thesis, it seems that this is not unequivocally valid (Appendix B, Table 4). In the case of copper and platinum this is true, but for gold and palladium such a thing does not occur.

Thus, it is finally evident that the material must have the most significant influence on the particle generation process. By calculating the total mass production from each material (Appendix C, Table 5), as Tabrizi predicted, and comparing to the measured results of the present work, results the following Figure 43, Equation (7) correctly reflects the results of the present work, in an approximate sense with respect to heat conduction, boiling temperature and evaporation enthalpy. It can therefore be used to predict the mass production rate for any material at the identical gap distance and spark type.
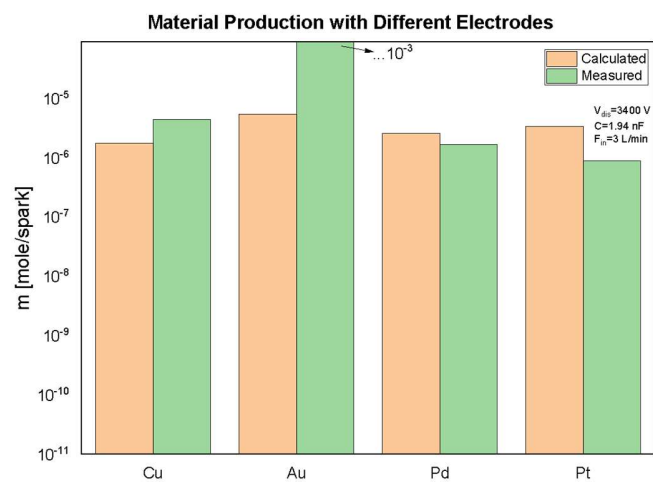
Figure 43. Material production from various electrodes.[3]

---

[3] The measured mass of material produced was found by calculating the space below the corresponding size distribution, because it was not possible to perform measurements of electrode mass loss directly.

4.2 Depositions

After the production of particles reached a good point in terms of understanding and reproducibility, depositions were made and studied on substrates of different materials. Thus, a series of samples were made on activated carbon cloth (ACC), borosilicate filters (BSF) and surgical polypropylene masks (PP Masks). The samples used in the present thesis are only a few out of more than 70 that were totally made and are presented in Appendix E (Table 6). The aim was to study the nature and size of the deposited particles, the purity of the materials, the depth they reach and the distribution they acquire during their deposition, as well as the properties that they can acquire in the context of applications.

A basic condition for a successful deposition, penetration and adsorption of aerosol nanoparticles throughout the depth of the substrate, is its fibrous nature, so that it is possible for the carrier gas to pass between fibers and to maintain the smooth operation of the experimental device (in terms of adequate gas flow etc). The different areas of the substrates that were deposited in the experiments are demonstrated in Figure 44 below; where *A* is the center of deposition area and *B* is the edge of it, while *I*, *II* and *III* are the top, the middle and the bottom part of the filter respectively; the arrows represent the carrier gas flow directions. Only in area A, the gas flow remains straight.
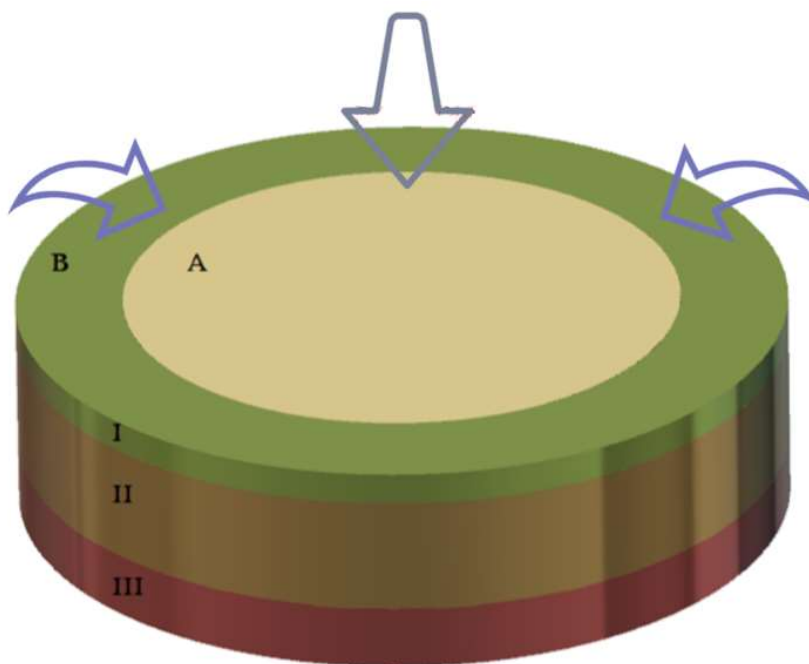
Figure 44. Graphic demonstration of different filter areas.

Prior to the deposition of the above-mentioned filters, the behavior of different types of particles was observed through TEM images, and how they are distributed on fibrous substrates, both in the case of

Cu/CuO (Figure 45) and gold (Figure 46). Figure 45a shows a TEM image of type i and ii CuO NPs diffused[4] on holey carbon fiber [106]. Figure 45b shows a TEM image of particles deposited on holey carbon films; type i and ii particles are captured near the edges of the carbon holes (near the carrier gas flow), while type iii spherical particles are captured further away from the holes, because of their inertial motion, ie. their relative inability to follow fully the gas flow.
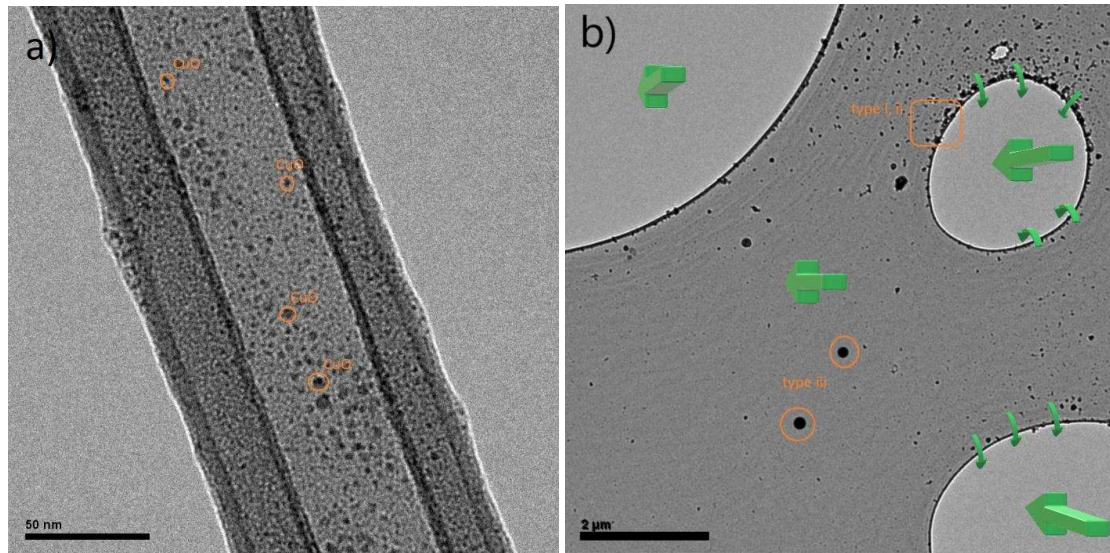
Figure 45. TEM images (a) type i diffused CuO NPs, (b) type ii & type iii Cu/CuO NPs on lacey carbon substrate (green arrows show carrier gas's flow).
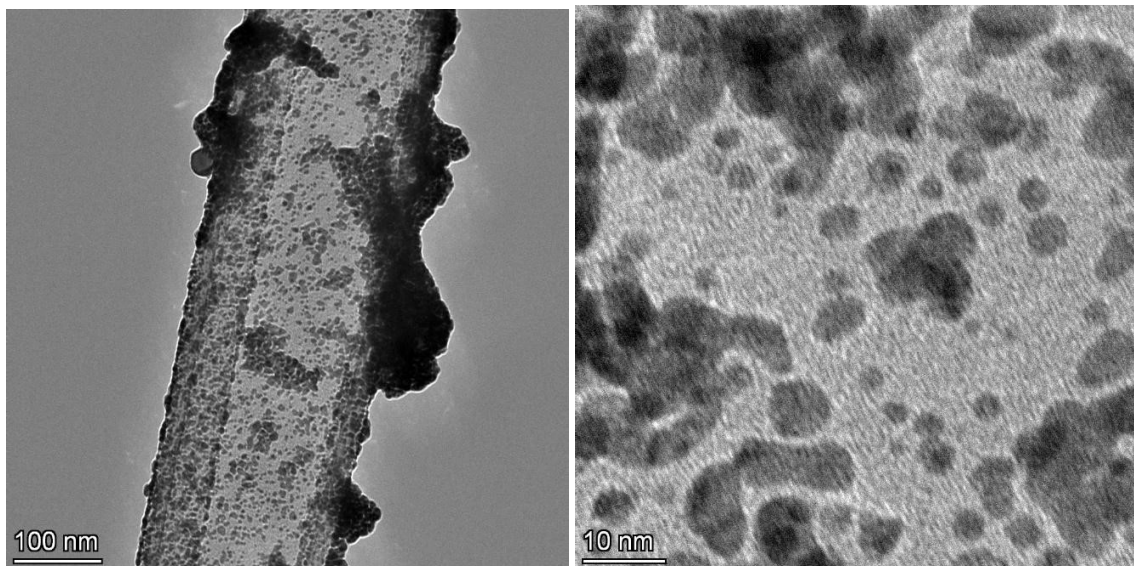
Figure 46. TEM image of primary and clusters AuNPs (left) and diffused AuNPs (right) on carbon fiber on TEM grid.

---

[4] Brownian diffusion of particles in a gas, is a physical mechanism when particles from an aerosol instantly diffuse and adhere on an obstacle (i.e., fiber) when it is placed in the stream [153].

4.2.1 NON-WOVEN ACTIVATED CARBON CLOTH (ACC)

As research has shown, activated carbon cloth can be used in many applications, such as antibacterial patches [116] and hydrogen storage [117]. Both antibacterial activity [116] and hydrogen capacity [118] [119] can be further enhanced by doping the ACCs with metal NPs (Ag and Pt respectively). Inspired by these results, depositions were carried out on the non-woven activated carbon cloth from Evertech Envisafe Ecology Co., ltd. (Thickness : 0.6 mm, Basic Weight : 70 ± 10 g/m^2, BET Surface Area : 1100 m^2/g, ACF Content：100%) with Cu/CuO, Pd and Pt nanoparticles with SDG whose efficiency in hydrogen storage has yet to be studied. The shape and chemical composition of the original ACC fibers show a special texture full of impurities (Figure 47) [120].
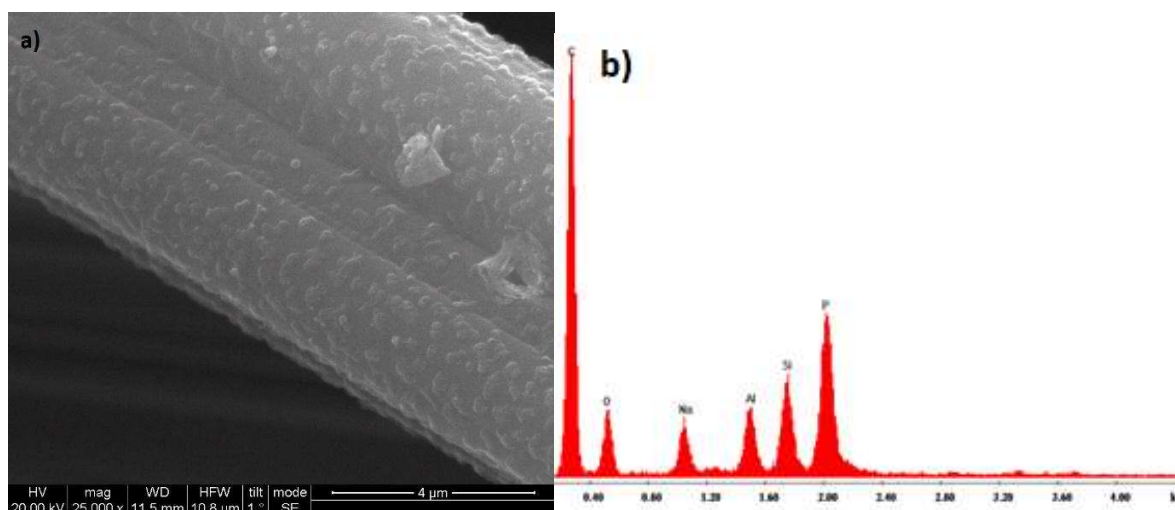
Figure 47. SE SEM image (a) and EDS analysis (b) of non-woven activated carbon cloth's microfibers

Research has shown that the deposition of nanoparticles on activated carbon fibers can be done in many different ways, including spark [121], resulting in large concentrations of nanoparticles of different materials to decorate, and often completely coat the fibers. However, the depositions made in the context of this work, were not aimed at the full coverage of the fibers. According to the SEM images and the subsequent EDS analysis of the Cu/CuO and Pd depositions, only type iii particles are detected (seen as large spheres with SE and as bright spots with BSE), which are extremely sparsely distributed throughout the ACC depth (Figures 48-49). According to studies, the liquid methods of depositing nanoparticles on ACC (vacuum impregnation [122], green reduction [119][120], electrodeposition [124] and Layer-by-Layer (LbL) self-assembly[5] [116]) appear to be extremely effective, resulting in nanoparticles of type ii and iii being distributed evenly on the fibers (concentrations 0.1-100 mg/cm^2).

---

[5] Layer-by-layer (LbL) self-assembly is an approach to develop an ultra-thin film on solid support by alternate exposure to positive and negative species with spontaneous deposition of the oppositely charged ions with wash steps in between [152]

In addition, during the depositions, a large amount of the produced material was observed to escape from the non-woven ACC due to the fact that this material is not made for use in filtering applications (as it is cloth and not filter) and its fibers are not very densely located next to each other [116]; this observation was made visually on paper filters (positioned at the back of the cloths), as no detailed SMPS measurements were made.
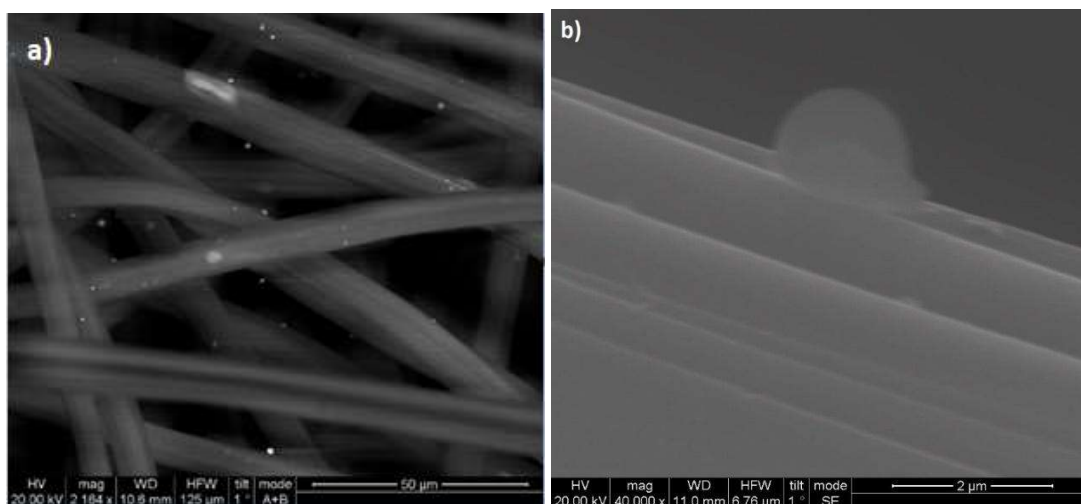
Figure 48. a) BSE SEM image of Cu/CuO type iii NPs distribution in ACC and b) SE SEM image of type iii Cu/CuO NP deposited in *AIII* area (400μm depth) (SDNM_8).
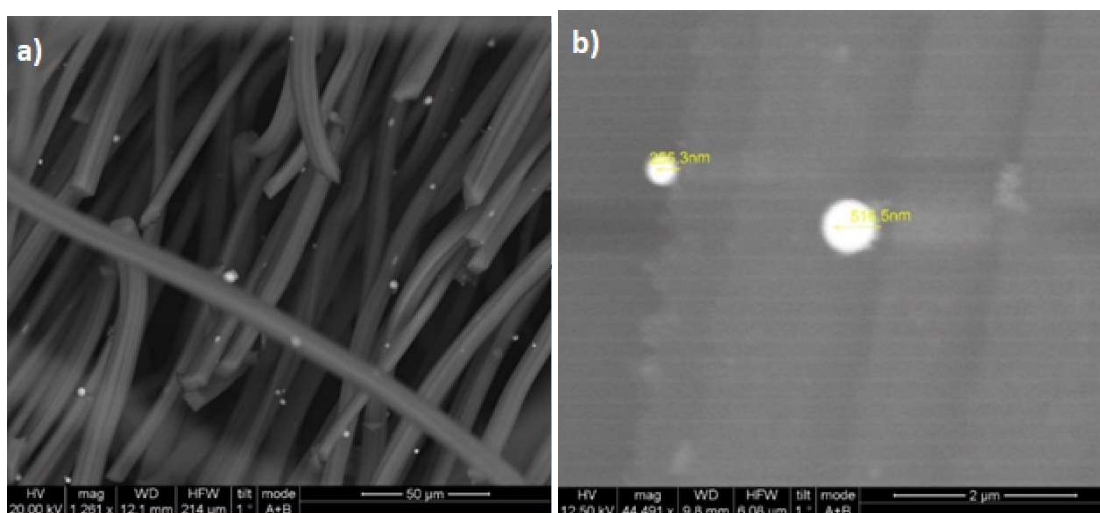
Figure 49. BSE SEM images of a) cs of Pd NPs deposited in ACC and b) the size of type iii particles in *AIII* area (430μm depth) (SDNM_43).

Based on these samples, adsorption and desorption measurements performed at the University of Leoben showed that Cu/CuO decorated ACC is effective, albeit at an early stage, as it retains N_2 in comparison

with the original (untreated) ACC, while gas sorption analysis showed slight reduction of pore size distribution of the decorated cloth (Figure 50).
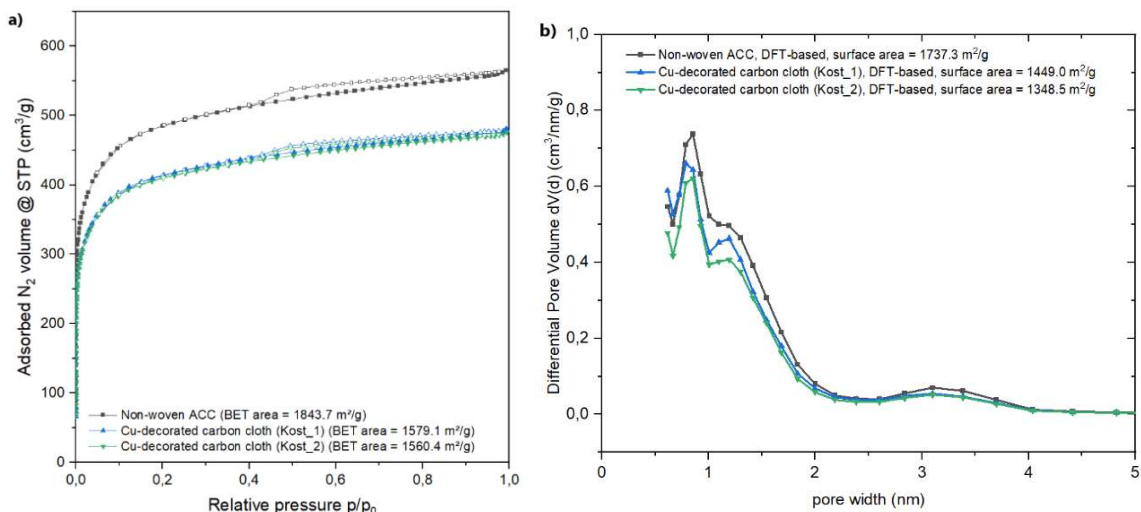
Figure 50. a) Adsorption/Desorption isotherms N2@77K, b) Pore size distribution from Gas Sorption Analysis; Cu/CuO decorated ACC.

More SEM images and EDS analysis of Cu/CuO and Pd type iii NPs depositions in non-woven ACC are presented in Appendix D.

4.2.2 BOROSILICATE MICROFIBER FILTERS (BSF)

Next, attention was focused on borosilicate filters characterized by dense, uniform, continuous and smooth microfibers. Borosilicate filters (Figure 51) are made up of very tiny microfibers of varying diameters (0.4-3.7 μm) and lengths that are mixed and shaped in a precise way to produce a matrix with varying free area sizes. Fibers form a highly tight network with a lot of open areas; this morphology forces the particles in the aerosols to repeatedly shift direction, slowing them down until a large portion of them is trapped by the glass fibers. NP depositions were studied through a series of samples on borosilicate microfiber filters from Whatman (GF/D Glass Microfiber Filters, retention range: 2.7 um, thickness: 0.53 mm, diameter: 5.5 cm).
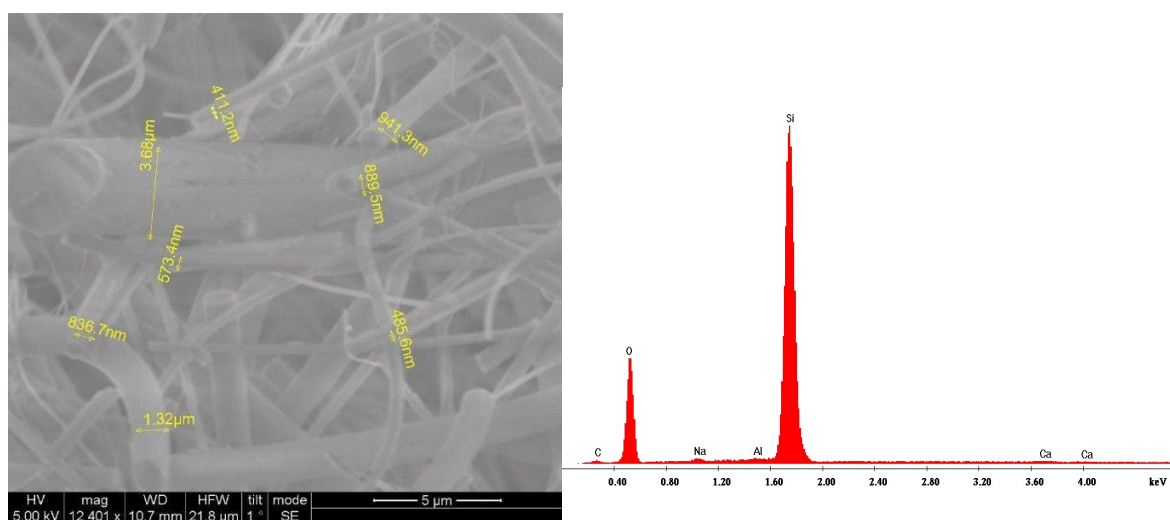
Figure 51. SE SEM image (left) and EDS analysis (right) of BSF's microfibers.

Various reports have shown that fiberglass filters (but not borosilicate filters specifically) are usually used for nanostructured decoration. Research has shown that fiberglass is the most common reinforcement for polymeric matrix nanocomposites deposited through thermolysis [125] and electroless plating [126]–[128]; the latter method is widely used for copper nanoparticle deposition on glass fibers [127], [128]. Additionally, the sonochemical method [129], [130] and the wet lay-up technique [131] are also usually mentioned. In all the above, nanoparticles seem to fully decorate BSF fibers, forming large type ii and type iii particle fractal structures.

In general, it seems that glass fiber filters are preferred for depositions through wet methods. No work seems to have been reported for spark discharge generated aerosol nanoparticles. Thus, the following results cannot be compared with those of the above reports. Herein, a series of Cu/CuO and Au aerosol decorated samples were prepared, and the depositions were studied in detail with SEM.

4.2.2.1 Cu/CuO

As explained in 4.1 section, Cu/CuO particle production exceeds to a huge size range, while type i particles constitute a large percentage of the total produced particle number. As shown in Figure 46a, type i and ii NPs appear to have size of just a few nanometers and are distributed over the fibers in fractal structures (Figure 52a). Furthermore, as can be clearly seen from Figure 50b, type iii particles present the same sparse distributional behavior as it was also observed in ACC fibers.
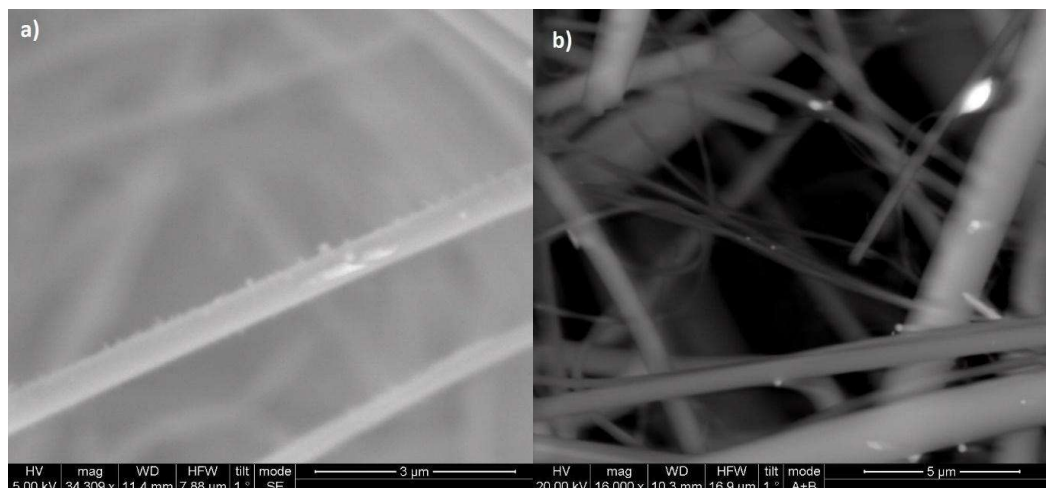
Figure 52. a) SE SEM image of type ii Cu/CuO fractal structures and b) BSE SEM image of type iii particles (SDNM_3).

NPs Escaping from BSFs

The sparse particle distribution observed so far, led to the need to measure particles that escape from BSFs. In this way, information is obtained for the retention of the material on the BSF fibers. While type i particles are diffused instantly onto the fibers (Figure 45a), type ii and type iii particles move inertially in the aerosol due to their mass. Type i and ii particles move according to the carrier gas flow redirections, while type iii tend to deviate from them and move linearly [82] (Figure 45b).

As seen Figure 54, when the carrier gas (N_2) flow rate is ≤ 2 L/min or ≥ 5 L/min, a larger percentage of type ii produced NPs (size 50-100 nm) escapes from BSFs (almost 35% and 20%, respectively). On the contrary, all types are trapped and deposited in greater quantities with flow rates between 3-4 L/min. Additionally, it is shown that at flow rates ≤ 2 L/min, type ii particles < 30 nm escape BSFs up to 5% while for larger flow rates the escape NP percentage is almost negligible. The fact that material loss is nil at ten nanometers demonstrates the effectiveness of borosilicate filters in diffusing type i and type ii (≤ 25 nm) NPs. Thus, by exploring alternative filters for NP depositions, it is possible to accomplish selective retention or non-retention of nanoparticles, depending on the size that is needed.
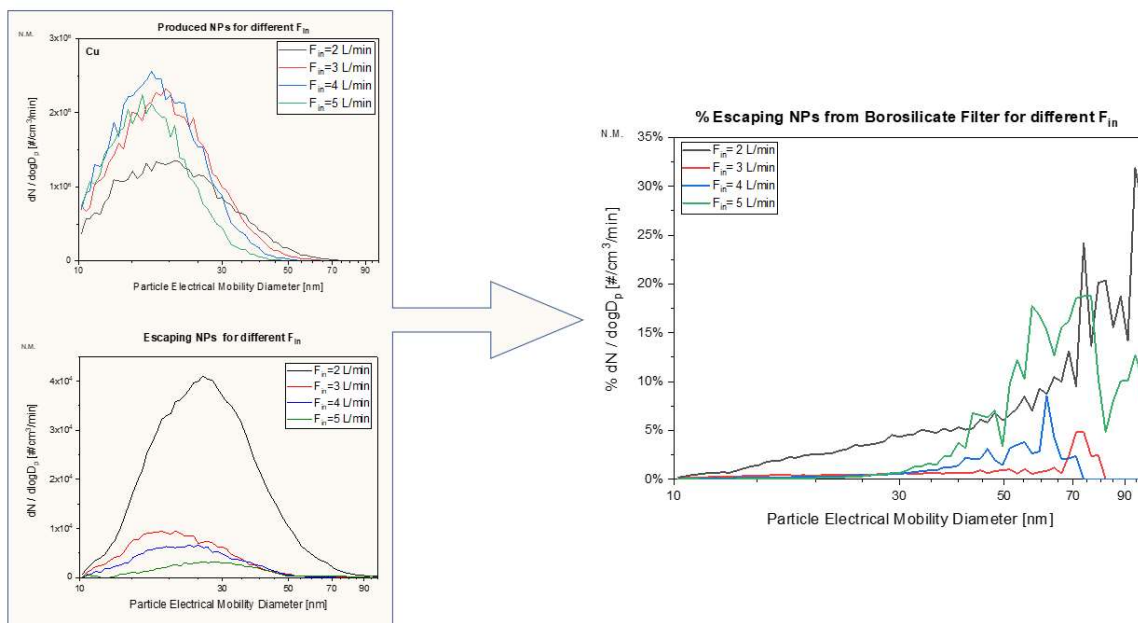
Figure 54. SMPS Data show the concentration of escaping NPs from borosilicate filter as a function to the incoming N₂ flow rate.

4.2.2.2 Au

As shown in Figure 43, Au particle production appears to be four orders of magnitude larger than Cu/CuO. The fact that gold is a heavier metal than copper, means also that Au NPs have better contrast in SEM images, and so particle and distribution study is more efficient. Subsequently, after electrode change in the experimental setup of the SDG, gold depositions were studied. Generally, NPs are trapped and deposited in area I of the BSF. In low magnification cross section SEM image (Figure 55), AuNPs distribution is representative for all material depositions, verifying SMPS measurements of escaping NPs (Figure 54), according to which, sizes >50 nm cross the entire filter relatively easily (i.e. also area II and III). More specifically, it seems that even in area II (depth of 300 μm out of a total of 530 μm) several type iii Au nanoparticles are located; type ii particles adhere to larger ones, thus forming fractals and dendrites.
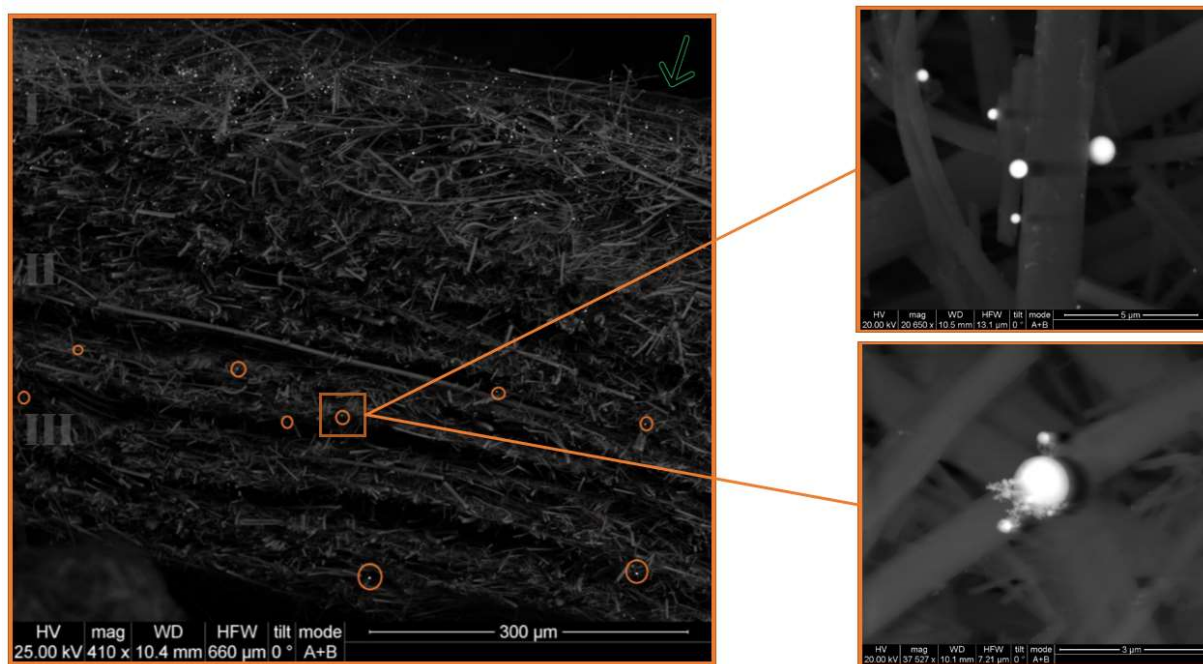
Figure 55. cs BSE SEM image of type iii AuNPs (light dots) deposited on BSF (SDNM_9).

According to Figure 55, most particles seem to be trapped and deposited in area I, while only a few seem to penetrate in greater depths. Indeed, comparing area I (a) with area II (b) and area III (c) of the borosilicate filter, an obvious decrease in concentration is observed while diverging from the deposition surface (Figure 56). In area I, most AuNPs are diffused and aggregated on fibers (Figure 46), while in area II there is a noticeable decrease in uniformity and predominantly fractal structures occur. Finally, in area III of the filter, minimal deposition elements are seen compared to the other two.
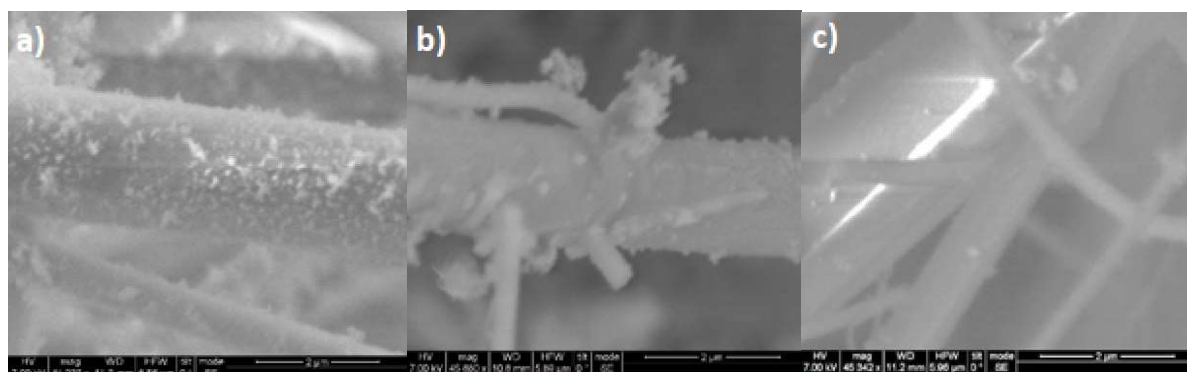
Figure 56. cs SE SEM image of AuNPs distribution in area I (a), area II (b) and area III (c) of BSF (SDNM_19).

This NP behavior in relation to the gas flow (Figure 45b) is also verified in case of AuNPs on a larger scale. The carrier gas arrives in area A linearly, while in area B changes directions (Figure 58). Type i and ii aerosol

AuNPs follow the gas flow deposit everywhere (both A and B areas), while type iii NPs continue their linear motion and remain mainly in area A (Figure 59).
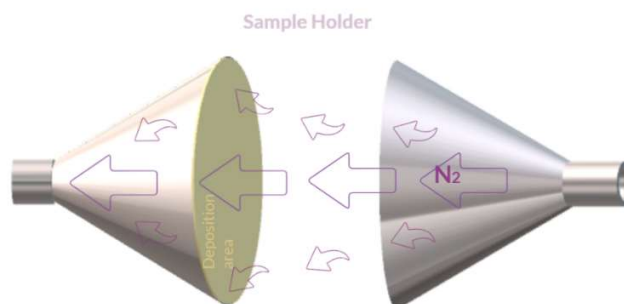
Figure 58. Air flow inside substrate holder of SDG.
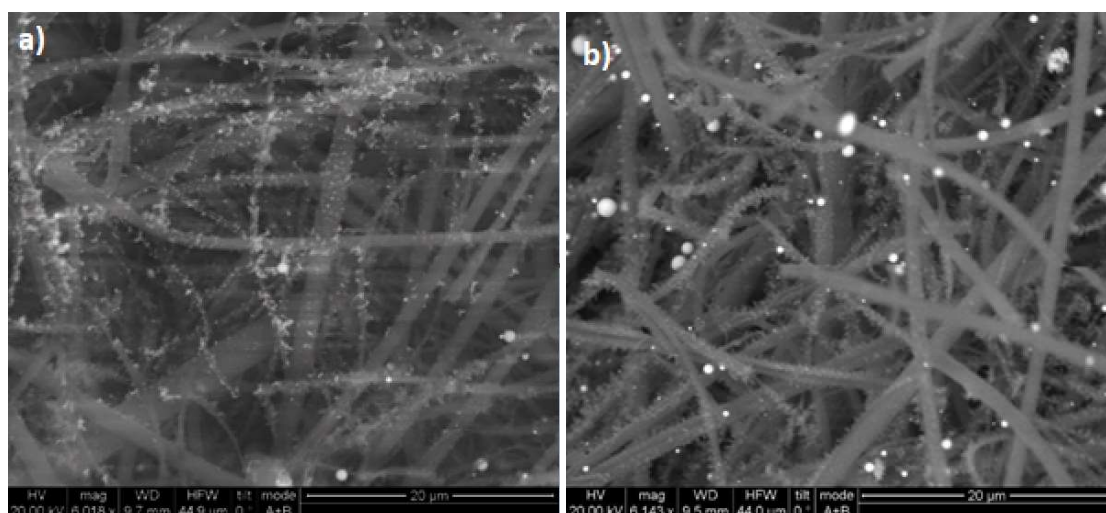
Figure 59. plan view BSE SEM image of AuNPs (a) on area B and (b) on area A on BSF (SDNM_26).

4.2.2.2.1 3D SERS Substrates

Gold nanoparticles are essential in SERS because they act as field-enhancing metallic centers [132]. They have been extensively used in SERS-based sensing for the purpose of amplifying the Raman signal of analytes that would otherwise remain undetectable due to low Raman cross sections or concentration limits [133]–[135].

A first attempt was made for the fabrication of 3D SERS substrates with AuNPs on borosilicate filters. AuNPs were deposited under various conditions and some first attempts were made in order to use them for the detection of Rhodamine with SERS. Rhodamine 6G (R6G, Fluka AG) was prepared in concentrations of 10^{-3}, 10^{-4} and 10^{-5} M and 10 μL were dropped on the substrates and left to dry for 10 minutes. Only at the high concentration of 1mM was it possible for the scans to find spots where a Raman signal (785 nm laser) could be caught (Figure 60).
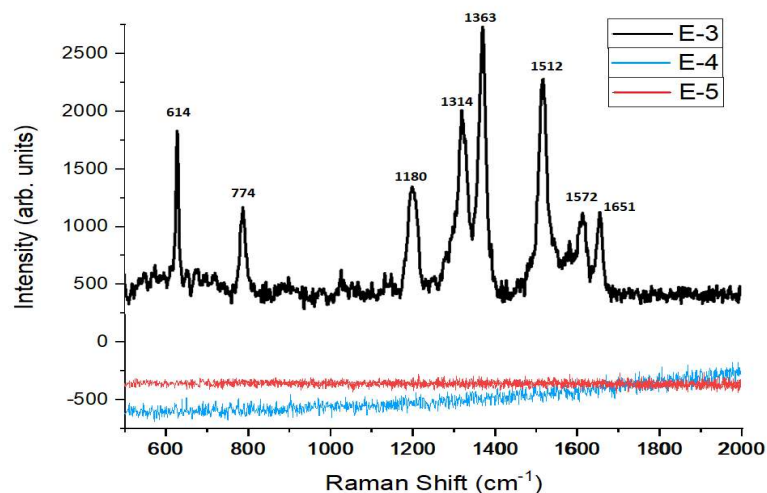
As the signal was found only in certain locations, the suspicion that it may come from areas where R6g had dried and therefore was denser, led to the need of SEM performance of the R6g deposited samples. From the SEM images obtained, large pieces of R6g were found resolidificated at specific points (Figure 61). Thus, the signal received from Raman may have arisen simply because the laser beam fell directly onto a R6g piece. In order to increase the plasmonic signal, it must be ensured that the total amount of rhodamine in the solution dispers more on the substrate, in order to avoid large concentrations at specific points. Another way of depositing rhodamine on the substrates probably needs to be found, or more hydrophilic substrates may need to be used.
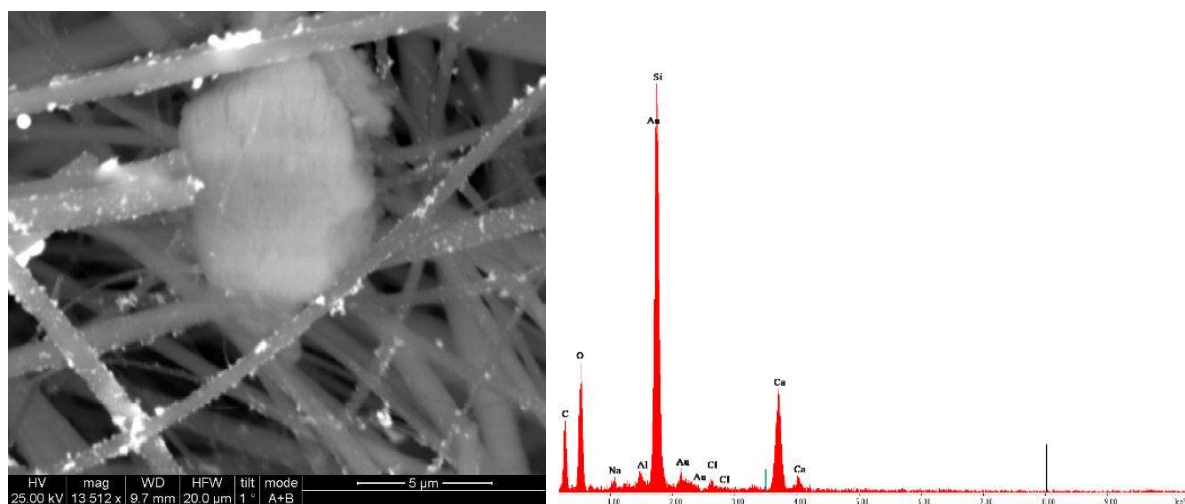
72

Kohut et. al. also performed SERS on glass microfiber filters loaded with varying composition SDG Au/Ag NPs. NPs were generated with C=8 nF, SRR=100Hz, using Ar carrier gas with F_{in}= 5 L/min (3-18 min depositions). 10µL of 1mM R6g aqueous solution were dropped on substrates, and Raman measurements were obtained by 785 nm laser. It was shown that even pure Au depositions provide signal enhancement and that the signal enhancement can be tuned by changing the Au/Ag composition of NPs [136]. These results indicate that possibly also the results presented in this thesis show indeed SERS signals, but unfortunately, we were not able to make further measurements. We have nevertheless a strong indication that we are moving in the right direction.

4.2.3 SURGICAL FACE MASKS

The next substrates employed for nanoparticle deposition (Cu/CuO) were the polypropylene (PP) surgical masks of the firm Plastics Thrace (single use surgical mask PLF .20 – type II according to ELOT EN 14683 + AC, BFE ≥ 98% bacterial filtration efficiency). These masks consist of three fiber sheets ("layers") (Figure 62). The outer layer has a mean fiber diameter of 20μm and is responsible for waterproofing the mask. The inner layer has the same mean fiber diameter and is responsible to give comfort in touch with the skin of the face. The middle layer has fibers < 5 μm and is responsible for filtering and retaining any pathogen.

Inside Layer   **Middle Layer**   **Outside Layer**
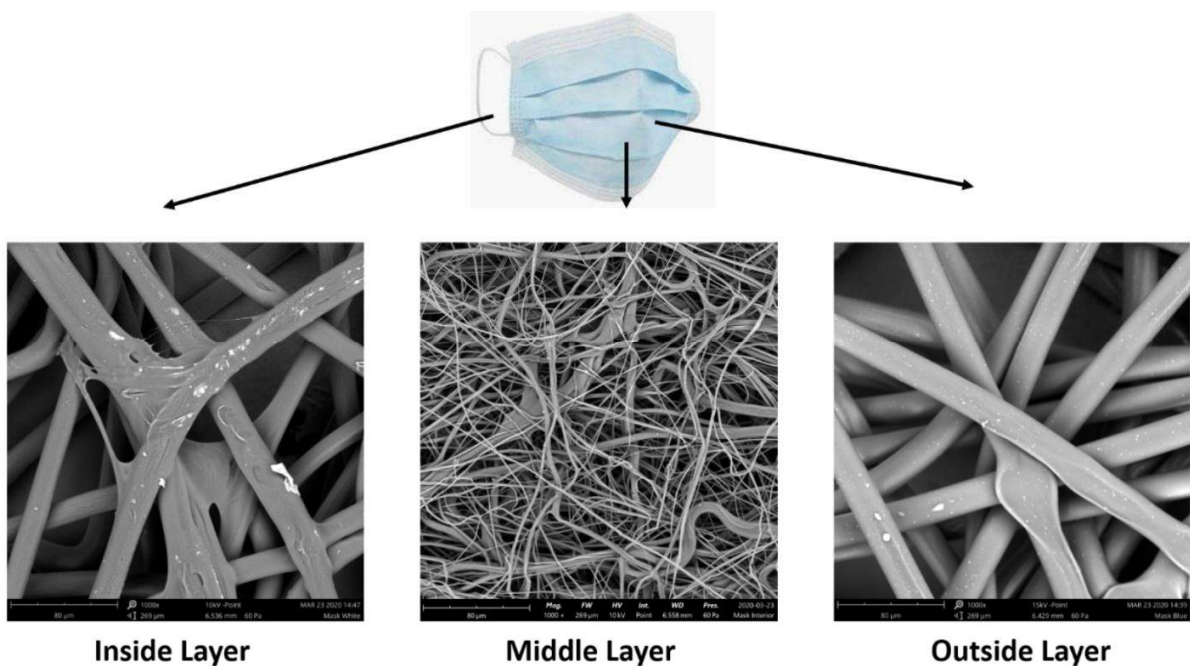
Figure 62. SE SEM images showing the fiber structure of different layers of surgical mask [137]**.**

Examining copper oxide depositions in all three layers of the masks, it is observed that indeed, the majority of the Cu/CuO NPs penetrate the outer layer and are deposited on the fibers of the middle, leaving the third and inner layer almost intact (Figure 63). They form fractal structures with sizes of hundreds of nanometers along the PP microfibers (Figure 64).
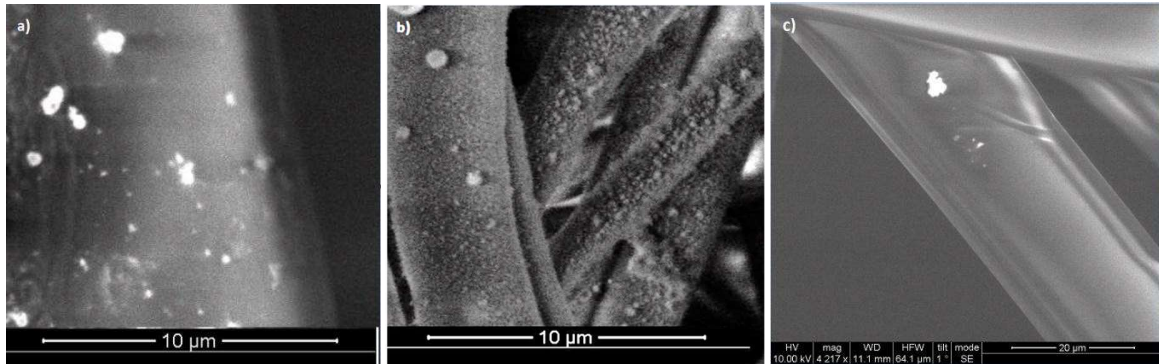
Figure 63. cs SE SEM image of Cu/CuO NPs on outer (A), on the middle (B) and on the inner layer (C) of surgical mask.
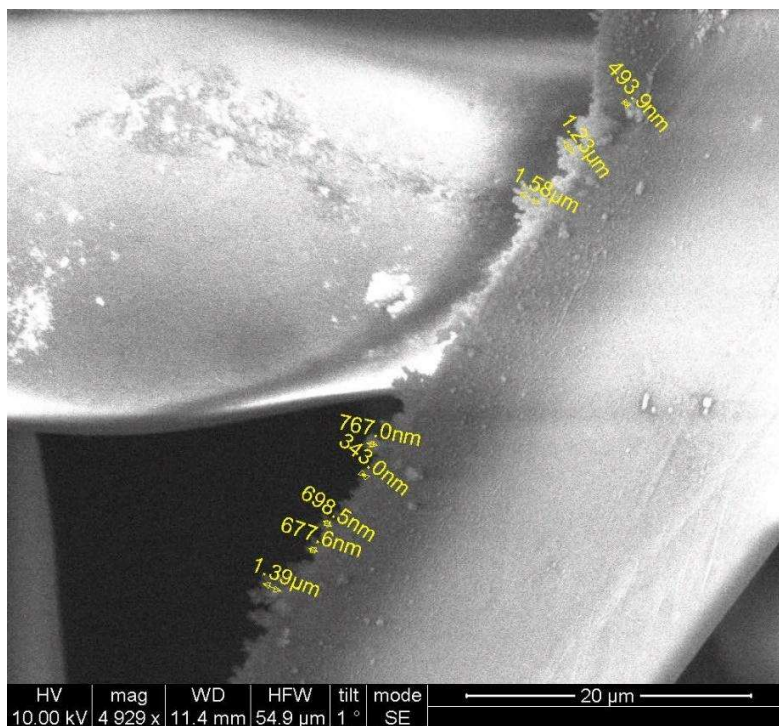
Figure 64. SEM image of secondary electron detector showing plan view of CuO NP distribution on outer mask layer, as well as NP dendrite sizes.

4.2.3.1 Antibacterial and Antiviral Application

As of February 2022, more than 5.7 million people have perished due to the COVID-19 pandemic, and the virus's spread continues to accelerate [138], [139]. This virus is transmitted via the air by coughing or vocalizing, and the transmission of viral infection in indoor air has been frequently observed [140]. Wearing a face mask is an efficient strategy to prevent SARS-CoV-2 infection since aerosols carrying viruses enter the human body via the nose or mouth. Since the outbreak of the pandemic, the demand for face masks has skyrocketed, resulting in a global shortage of personal protective equipment (or else referred as PPE) [141]. As a result of this scarcity, medical workers in hospitals have been forced to reuse masks that may have been infected with the virus while treating patients with the suspected or confirmed

75

infection of COVID-19 [142]. Even in nations where mask shortages have been alleviated, there are still certain areas where supplies are low [143]. While disposable masks generate micro-plastic waste, the development of reusable PPE might overcome these problems [144].

When used in a clinical area, surgical-grade masks may successfully limit the transmission of airborne droplets. Even with its several non-woven layers, three-layer surgical masks are susceptible to contamination by droplets, which might allow the virus and bacteria to potentially get past the protective layers [145]. As a result, it may not be the best choice for community usage. It is possible for the hands to get infected with virus and bacteria during the process of handling masks, which may then be transmitted to the face via direct contact. SARS-CoV-2 aerosolized droplet protection is not possible with traditional surgical masks. In order to reduce the possibility of viral transmission via contaminated surfaces, face masks should be improved. The antiviral and antibacterial effects of face masks [145] were improved by embedding organic and inorganic components with nonwoven or fabric materials in previous efforts [145]. This reduced exposure to SARS-CoV-2 to below the typical person's minimum infectious dose. Copper, silver, and gold have all been shown to have significant inactivation levels for SARS-CoV-2 and bacteria when used in the mask production process [146]. Copper has long been recognized for its antiviral properties [147], [148], as Copper cations are excellent in capturing and penetrating bacteria and viruses that are negatively charged.

Using Cu as an antibacterial and antiviral ingredient in the production of SARS-CoV-2 protective masks is a promising approach. During this work, Cu/CuO loaded masks were tested against the SARS-CoV-2 virus and E-Coli bacteria. Using a three-layer construction of rough exterior layer, thick interwoven fabric material middle layer, and fine interwoven material inner layer, the mask build was intended to maximize the entrapment efficiency of the mask. The outer and middle layers include fibers coated or impregnated with Cu/CuO, whereas the inner layer is totally devoid of NPs. Cu/CuO particles are used to inactivate virus particles by trapping aerosolized droplets in the middle layer.

A series of Cu/CuO decorated mask samples were prepared and tested for antibacterial activity against Escherichia Coli (E. Coli) bacteria[6], whose characteristics are presented in Table 2. Comparing to the control (reference substrates without NPs) fiber surfaces of masks, the Cu/CuO-decorated fiber air filters exhibited higher antibacterial activity. More precisely, Mask_5 demonstrated a 100% decrease in cell viability (***$p \leq 0.001$), and Mask_6 demonstrated a 99% decrease in cell viability with a p-value[7] of (****$p \leq 0.0001$) [106], as illustrated in Figure 65.

---

[6] E. Coli is a bacterium that occurs naturally in the intestines of people and animals and is widely used for various types of research since 1927, as it is harmless and divides rapidly [154].
[7] It is a statistical value that shows the possibility of cell viability under a specific hypothesis.

Table 2. Cu/CuO spark deposited surgical masks' SDG specs and antibacterial performances against E-Coli.

Sample Name	Layers deposited	Deposition time (h)	V_{dis} (kV)	f (Hz)	Particles/ cm^2 [8]	Cell Viability (%)
Control_5	3 layers	-	-	-	-	100
Control_6	Middle Layer	-	-	-	-	100
Mask_5	3 layers	21	2.9	128	4×10^9	0
Mask_6	Middle layer	9.5	2.9	128	2×10^9	1
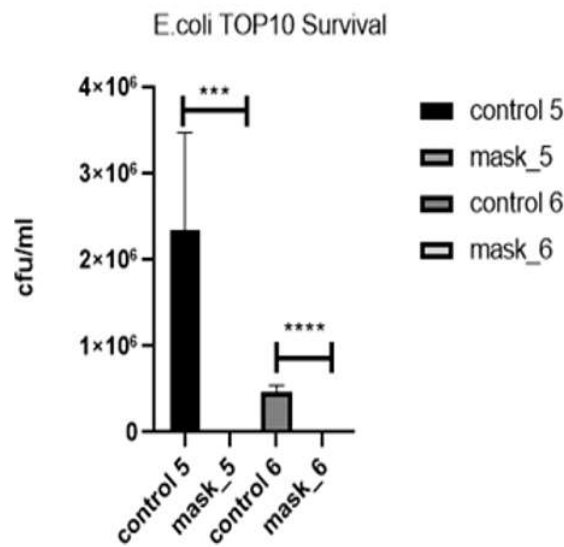
Figure 65. Cell viability of E. coli on Cu/CuO NP decorated masks in comparison to control PP masks; statistical significance was performed using t-test [106].

After exhibiting excellent antibacterial behavior, a second batch of the same samples were tested unsuccessfully for antiviral properties. Subsequently, another two samples were prepared and tested against SARS-CoV-2, whose characteristics and antibacterial activity are shown in Table 2 below. These mask layers were deposited for longer durations, therefore they contained larger numbers of Cu/CuO nanoparticles. The number of infectious virus particles is quantified by using the Median Tissue Culture Infectious Dose ($TCID_{50}$)/ml assay. In comparison with their control (reference) fiber surfaces of masks, Mask_8 showed 90% efficiency after 15 minutes of virus stay on the mask, whilst Mask_10 showed an efficiency of only 43.8% virus neutralization (Figure 66). This diminished antiviral effect of Mask_10 was expected, as the majority of nanoparticles penetrate the outer layer and are deposited on the fibers of the middle, whereas the virus droplets are very likely to be retained also by the outer layer, avoiding contact with copper oxide particles in the middle layer and thus remaining unneutralized (Table 3).

---

[8] Assuming 100% particle deposition.

Sample Name	Layer deposited	Deposition time (h)	V_{dis} (kV)	f (Hz)	Particles/ cm^2 [9]	$TCID_{50}$/ml
Control_8	-	-	-	-	-	1780
Control_10	-	-	-	-	-	562
Mask_8	Middle layer	4.5	2.7	110	8×10^8	178
Mask_10	3 layers	13	4	80	2×10^9	316
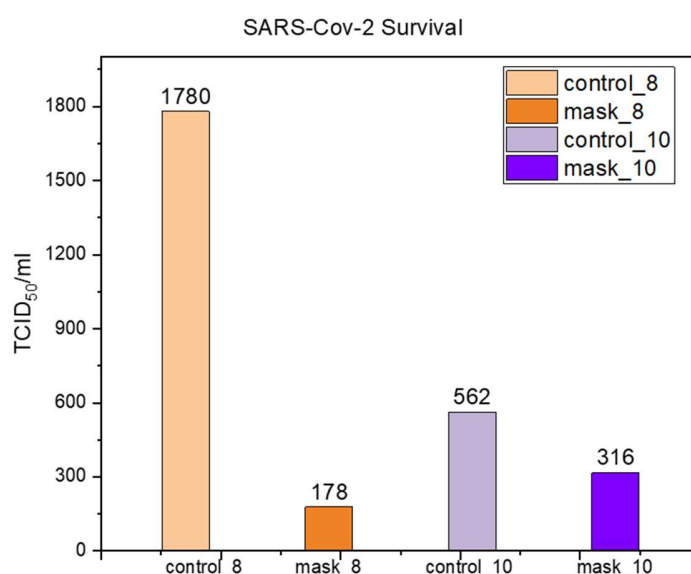
Figure 66. viability of SARS-CoV-2 on Cu/CuO NP decorated masks in comparison to control PP masks.

Discussion

In the context of the present thesis, nanoparticles were deposited on ACC, BSFs and PP surgical masks. With SEM it was possible to detect type ii clusters and type iii spherical particles that are larger than type i and are therefore more easily detected, and which can reach sizes in the order of µm.

SEM revealed a general difficulty in detecting type i NPs deposited in ACCs and BSFs. However, the absence of observation does not indicate the lack of their existence. For the Cu / CuO depositions on BSFs, it was measured that the particles that escape from the filters are two orders of magnitude less in concentration. Other approaches, particularly microscopic ones with a better resolution, may be required for their better detection. Besides, AuNP depositions allowed one to obtain information on how the particles are deposited and distributed within the BSFs. Herein, aerosol science is not delved in, but is used as a tool to focus on materials science. Their presence is primarily established in this study through

---

[9] Assuming 100% particle deposition.

the functioning of the total depositions within the applications (porosimetry, SERS, antibacterial and antiviral tests).

This was a first approach for the use of the SDG technique in applications, and results seem to be very promising. It is worth noting again that during the current tight situation (pandemic), antiviral masks loaded with Cu/CuO can be a crucial tool in reducing the transmission of SARS-CoV-2 inside communities [149], [150], [151].

5. CONCLUSIONS

During the present thesis, the synthesis of nanoparticles using a spark discharge generator (SDG) has been researched in detail. The process is noteworthy because it is continuous, clean, very material-independent, and allows for control of the mean particle size. Aerosol nanoparticles were produced from 4 different starting materials/electrodes (Cu, Au, Pd, Pt), and were deposited in a range of fibrous substrates. The aerosol's concentration characterization, the characterization of the nanoparticles themselves, as well as the characterization of their depositions on the substrates gave an insight of their formation process as well as the ways that they can be used to modify fibrous structures. It was confirmed that particles are mostly nanoscale-sized but there is also a clear presence of larger particles that show a different behavior in depositions. The optimum control parameters were found, in order to optimize the concentration of the produced nanoparticles for every electrode material, as each one of them behaves differently, according to its physical characteristics. In this context, the effect of the SDG on the remaining electrode material was also studied.

Although the particles generated in this study have the potential to be used in a wide variety of applications, only specific scenarios were studied For their use in H storage, for 3D SERS substrates and for antiviral/antibacterial protection. In all cases they showed very promising results indicating that this low-cost method has a tremendous exploitation potential.

For future work, different carrier gasses, materials and substrates could be studied, as it would be feasible to manage the creation, deposition, retention, and dumping of certain particle sizes based on the distribution of nanoparticles in the filters. The NP behavior deposited on TEM grids with different gas flows could also be studied. Additionally, the presence of carbon on electrodes and its deposition could be investigated, too.

BIBLIOGRAPHY

[1]   M. Diez-Silva, M. Dao, J. Han, C.-T. Lim, and S. Suresh, "Shape and Biomechanical Characteristics of Human Red Blood Cells in Health and Disease.," *MRS Bull.*, vol. 35, no. 5, pp. 382–388, May 2010, doi: 10.1557/mrs2010.571.

[2]   V. V Rybenkov and A. V Vologodskiĭ, "[Effective diameter of DNA].," *Mol. Biol. (Mosk).*, vol. 26, no. 6, pp. 1433–9.

[3]   D. E. McREE, "COMPUTATIONAL TECHNIQUES," in *Practical Protein Crystallography*, Elsevier, 1999, pp. 91-cp1.

[4]   C. M. Sotomayor Torres *et al.*, "Nanoimprint lithography: an alternative nanofabrication approach," *Mater. Sci. Eng. C*, vol. 23, no. 1–2, Jan. 2003, doi: 10.1016/S0928-4931(02)00221-7.

[5]   D. M. Valenzuela *et al.*, "High-throughput engineering of the mouse genome coupled with high-resolution expression analysis," *Nat. Biotechnol.*, vol. 21, no. 6, Jun. 2003, doi: 10.1038/nbt822.

[6]   G. Chen, L. K. Shrestha, and K. Ariga, "Zero-to-Two Nanoarchitectonics: Fabrication of Two-Dimensional Materials from Zero-Dimensional Fullerene," *Molecules*, vol. 26, no. 15, p. 4636, Jul. 2021, doi: 10.3390/molecules26154636.

[7]   N. Amdursky, M. Molotskii, E. Gazit, and G. Rosenman, "Elementary Building Blocks of Self-Assembled Peptide Nanotubes," *J. Am. Chem. Soc.*, vol. 132, no. 44, pp. 15632–15636, Nov. 2010, doi: 10.1021/ja104373e.

[8]   K. Mori, "Photo-Functionalized Materials Using Nanoparticles: Photocatalysis [Translated]<sup>†</sup>," *KONA Powder Part. J.*, vol. 23, no. 0, 2005, doi: 10.14356/kona.2005023.

[9]   Y. Yang, W. Huang, J. Lu, and J. Chu, "Fabrication of thick Pb(Zr,Ti)O3 (PZT) films by modified sol–gel methods for application in MEMS," *J. Micromechatronics*, vol. 2, no. 3, Dec. 2002, doi: 10.1163/156856304773954250.

[10]   V. Petkov, Y. Peng, G. Williams, B. Huang, D. Tomalia, and Y. Ren, "Structure of gold nanoparticles suspended in water studied by x-ray diffraction and computer simulations," *Phys. Rev. B*, vol. 72, no. 19, Nov. 2005, doi: 10.1103/PhysRevB.72.195402.

[11]   B. Gilbert, F. Huang, H. Zhang, G. A. Waychunas, and J. F. Banfield, "Nanoparticles: Strained and Stiff," *Science (80-.).*, vol. 305, no. 5684, Jul. 2004, doi: 10.1126/science.1098454.

[12]   G. A. Baker, "Nanoparticles: From Theory to Application Edited by Günter Schmid (University of Duisberg-Essen). Wiley-VCH Verlag GmbH & Co. KGaA: Weinheim, Germany. 2004. x + 434 pp. $210.00. ISBN 3-527-30507-6.," *J. Am. Chem. Soc.*, vol. 126, no. 47, Dec. 2004, doi: 10.1021/ja040954f.

[13]   L. Manna, D. J. Milliron, A. Meisel, E. C. Scher, and A. P. Alivisatos, "Controlled growth of tetrapod-branched inorganic nanocrystals," *Nat. Mater.*, vol. 2, no. 6, Jun. 2003, doi: 10.1038/nmat902.

[14]   V. Rotello, *Nanoparticles*. Boston, MA: Springer US, 2004.

[15]   Y. Leconte *et al.*, "Comparative Study of Structural Damage Under Irradiation in SiC

Nanostructured and Conventional Ceramics," *MRS Proc.*, vol. 981, Feb. 2006, doi: 10.1557/PROC-981-0981-JJ07-11.

[16]   K. Ulbrich, K. Holá, V. Šubr, A. Bakandritsos, J. Tuček, and R. Zbořil, "Targeted Drug Delivery with Polymers and Magnetic Nanoparticles: Covalent and Noncovalent Approaches, Release Control, and Clinical Studies," *Chem. Rev.*, vol. 116, no. 9, May 2016, doi: 10.1021/acs.chemrev.5b00589.

[17]   N. Kostoglou *et al.*, "Nanoporous polymer-derived activated carbon for hydrogen adsorption and electrochemical energy storage," *Chem. Eng. J.*, vol. 427, Jan. 2022, doi: 10.1016/j.cej.2021.131730.

[18]   A. K.-T. Lau and D. Hui, "The revolutionary creation of new advanced materials—carbon nanotube composites," *Compos. Part B Eng.*, vol. 33, no. 4, Jun. 2002, doi: 10.1016/S1359-8368(02)00012-4.

[19]   H. Kang, L. Wang, M. O'Donoghue, Y. C. Cao, and W. Tan, "NANOPARTICLES FOR BIOSENSORS," in *Optical Biosensors*, Elsevier, 2008.

[20]   P. D. Rakowska *et al.*, "Antiviral surfaces and coatings and their mechanisms of action," *Commun. Mater.*, vol. 2, no. 1, Dec. 2021, doi: 10.1038/s43246-021-00153-y.

[21]   M. J. Allen, V. C. Tung, and R. B. Kaner, "Honeycomb Carbon: A Review of Graphene," *Chem. Rev.*, vol. 110, no. 1, Jan. 2010, doi: 10.1021/cr900070d.

[22]   M. Heurlin *et al.*, "Continuous gas-phase synthesis of nanowires with tunable properties," *Nature*, vol. 492, no. 7427, Dec. 2012, doi: 10.1038/nature11652.

[23]   V. V. Pokropivny and V. V. Skorokhod, "Classification of nanostructures by dimensionality and concept of surface forms engineering in nanomaterial science," *Mater. Sci. Eng. C*, vol. 27, no. 5–8, Sep. 2007, doi: 10.1016/j.msec.2006.09.023.

[24]   C. Altavilla and E. Ciliberto, "Inorganic Nanoparticles: Synthesis, Applications, and Perspectives," *CRC Press. Boca Rat.*, 2011.

[25]   O. V. Singh, Ed., *Bio-Nanoparticles*. Hoboken, NJ: John Wiley & Sons, Inc, 2015.

[26]   M. Pumera, A. Ambrosi, and E. L. K. Chng, "Impurities in graphenes and carbon nanotubes and their influence on the redox properties," *Chem. Sci.*, vol. 3, no. 12, 2012, doi: 10.1039/c2sc21374e.

[27]   J. Feng, G. Biskos, and A. Schmidt-Ott, "Toward industrial scale synthesis of ultrapure singlet nanoparticles with controllable sizes in a continuous gas-phase process," *Sci. Rep.*, vol. 5, no. 1, Dec. 2015, doi: 10.1038/srep15788.

[28]   K. Wegner and S. E. Pratsinis, "Scale-up of nanoparticle synthesis in diffusion flame reactors," *Chem. Eng. Sci.*, vol. 58, no. 20, Oct. 2003, doi: 10.1016/j.ces.2003.07.010.

[29]   B. O. Meuller *et al.*, "Review of Spark Discharge Generators for Production of Nanoparticle Aerosols," *Aerosol Sci. Technol.*, vol. 46, no. 11, Nov. 2012, doi: 10.1080/02786826.2012.705448.

[30]   M. H. Magnusson, K. Deppert, J.-O. Malm, J.-O. Bovin, and L. Samuelson, "Size-selected gold nanoparticles by aerosol technology," *Nanostructured Mater.*, vol. 12, no. 1–4, Jan. 1999, doi: 10.1016/S0965-9773(99)00063-X.

[31] M. Brust, M. Walker, D. Bethell, D. J. Schiffrin, and R. Whyman, "Synthesis of thiol-derivatised gold nanoparticles in a two-phase Liquid–Liquid system," *J. Chem. Soc., Chem. Commun.*, vol. 0, no. 7, 1994, doi: 10.1039/C39940000801.

[32] M. Kim, S. Osone, T. Kim, H. Higashi, and T. Seto, "Synthesis of Nanoparticles by Laser Ablation: A Review," *KONA Powder Part. J.*, vol. 34, no. 0, 2017, doi: 10.14356/kona.2017009.

[33] S. Schwyn, E. Garwin, and A. Schmidt-Ott, "Aerosol generation by spark discharge," *J. Aerosol Sci.*, vol. 19, no. 5, Oct. 1988, doi: 10.1016/0021-8502(88)90215-7.

[34] D. Nunes *et al.*, "Synthesis, design, and morphology of metal oxide nanostructures," in *Metal Oxide Nanostructures*, Elsevier, 2019.

[35] T. V. Pfeiffer, J. Feng, and A. Schmidt-Ott, "New developments in spark production of nanoparticles," *Adv. Powder Technol.*, vol. 25, no. 1, Jan. 2014, doi: 10.1016/j.apt.2013.12.005.

[36] P. U. Aerosol Research Lab, "Synthesis of aerosol nanoparticles for toxicity tests," *https://www.purdue.edu/hhs/hsci/aerosol/research/research.php*. .

[37] M. E. Messing *et al.*, "Generation of Pd Model Catalyst Nanoparticles by Spark Discharge," *J. Phys. Chem. C*, vol. 114, no. 20, May 2010, doi: 10.1021/jp101390a.

[38] M. Stein, D. Kiesler, and F. E. Kruis, "Effect of carrier gas composition on transferred arc metal nanoparticle synthesis," *J. Nanoparticle Res.*, vol. 15, no. 1, Jan. 2013, doi: 10.1007/s11051-012-1400-9.

[39] T. Pfeiffer, P. Kedia, M. Messing, M. Valvo, and A. Schmidt-Ott, "Precursor-Less Coating of Nanoparticles in the Gas Phase," *Materials (Basel).*, vol. 8, no. 3, Mar. 2015, doi: 10.3390/ma8031027.

[40] Y. Bae, P. V. Pikhitsa, H. Cho, and M. Choi, "Multifurcation Assembly of Charged Aerosols and Its Application to 3D Structured Gas Sensors," *Adv. Mater.*, vol. 29, no. 2, Jan. 2017, doi: 10.1002/adma.201604159.

[41] A. Muntean, M. Wagner, J. Meyer, and M. Seipenbusch, "Generation of copper, nickel, and CuNi alloy nanoparticles by spark discharge," *J. Nanoparticle Res.*, vol. 18, no. 8, Aug. 2016, doi: 10.1007/s11051-016-3547-2.

[42] J. H. Byeon, J. H. Park, K. Y. Yoon, and J. Hwang, "Ambient spark generation to synthesize carbon-encapsulated metal nanoparticles in continuous aerosol manner," *Nanoscale*, vol. 1, no. 3, 2009, doi: 10.1039/b9nr00058e.

[43] N. S. Tabrizi, M. Ullmann, V. A. Vons, U. Lafont, and A. Schmidt-Ott, "Generation of nanoparticles by spark discharge," *J. Nanoparticle Res.*, vol. 11, no. 2, Feb. 2009, doi: 10.1007/s11051-008-9407-y.

[44] P. Karjalainen *et al.*, "Exhaust particles of modern gasoline vehicles: A laboratory and an on-road study," *Atmos. Environ.*, vol. 97, Nov. 2014, doi: 10.1016/j.atmosenv.2014.08.025.

[45] M.-C. O. Chang, J. C. Chow, J. G. Watson, P. K. Hopke, S.-M. Yi, and G. C. England, "Measurement of Ultrafine Particle Size Distributions from Coal-, Oil-, and Gas-Fired Stationary Combustion Sources," *J. Air Waste Manage. Assoc.*, vol. 54, no. 12, Dec. 2004, doi: 10.1080/10473289.2004.10471010.

[46] P. Kumar, L. Pirjola, M. Ketzel, and R. M. Harrison, "Nanoparticle emissions from 11 non-vehicle exhaust sources – A review," *Atmos. Environ.*, vol. 67, Mar. 2013, doi: 10.1016/j.atmosenv.2012.11.011.

[47] A. Hartland, M. S. Andersen, and D. P. Hamilton, "Phosphorus and arsenic distributions in a seasonally stratified, iron- and manganese-rich lake: microbiological and geochemical controls," *Environ. Chem.*, vol. 12, no. 6, 2015, doi: 10.1071/EN14094.

[48] Q. Abbas *et al.*, "Transformation pathways and fate of engineered nanoparticles (ENPs) in distinct interactive environmental compartments: A review," *Environ. Int.*, vol. 138, May 2020, doi: 10.1016/j.envint.2020.105646.

[49] "X. The Bakerian Lecture. —Experimental relations of gold (and other metals) to light," *Philos. Trans. R. Soc. London*, vol. 147, Dec. 1857, doi: 10.1098/rstl.1857.0011.

[50] A. K. Singh, *Engineered Nanoparticles: Structure, Properties and Mechanisms of Toxicity*. San DIego: Elsevier, 2015.

[51] R. S. Rawat, "Dense Plasma Focus - From Alternative Fusion Source to Versatile High Energy Density Plasma Source for Plasma Nanotechnology," *J. Phys. Conf. Ser.*, vol. 591, Mar. 2015, doi: 10.1088/1742-6596/591/1/012021.

[52] I. A. Rahman and V. Padavettan, "Synthesis of Silica Nanoparticles by Sol-Gel: Size-Dependent Properties, Surface Modification, and Applications in Silica-Polymer Nanocomposites—A Review," *J. Nanomater.*, vol. 2012, 2012, doi: 10.1155/2012/132424.

[53] N. Aboualigaledari and M. Rahmani, "A review on the synthesis of the TiO2-based photocatalyst for the environmental purification," *J. Compos. Compd.*, vol. 2, no. 5, Mar. 2021, doi: 10.52547/jcc.3.1.4.

[54] W. Teoh, "A Perspective on the Flame Spray Synthesis of Photocatalyst Nanoparticles," *Materials (Basel).*, vol. 6, no. 8, Jul. 2013, doi: 10.3390/ma6083194.

[55] J. D. Landgrebe and S. E. Pratsinis, "A discrete-sectional model for particulate production by gas-phase chemical reaction and aerosol coagulation in the free-molecular regime," *J. Colloid Interface Sci.*, vol. 139, no. 1, Oct. 1990, doi: 10.1016/0021-9797(90)90445-T.

[56] R. Koirala, S. E. Pratsinis, and A. Baiker, "Synthesis of catalytic materials in flames: opportunities and challenges," *Chem. Soc. Rev.*, vol. 45, no. 11, 2016, doi: 10.1039/C5CS00011D.

[57] S. Salameh, J. Gómez-Hernández, A. Goulas, H. Van Bui, and J. R. van Ommen, "Advances in scalable gas-phase manufacturing and processing of nanostructured solids: A review," *Particuology*, vol. 30, Feb. 2017, doi: 10.1016/j.partic.2016.07.003.

[58] C. Hoffmann, C. Berganza, and J. Zhang, "Cold Atmospheric Plasma: methods of production and application in dentistry and oncology," *Med. Gas Res.*, vol. 3, no. 1, p. 21, 2013, doi: 10.1186/2045-9912-3-21.

[59] J. P. Borra, "Charging of aerosol and nucleation in atmospheric pressure electrical discharges," *Plasma Phys. Control. Fusion*, vol. 50, no. 12, Dec. 2008, doi: 10.1088/0741-3335/50/12/124036.

[60] R. Ye, J.-G. Li, and T. Ishigaki, "Controlled synthesis of alumina nanoparticles using inductively coupled thermal plasma with enhanced quenching," *Thin Solid Films*, vol. 515, no. 9, Mar. 2007,

doi: 10.1016/j.tsf.2006.02.050.

[61]   W. Mahoney and R. P. Andres, "Aerosol synthesis of nanoscale clusters using atmospheric arc evaporation," *Mater. Sci. Eng. A*, vol. 204, no. 1–2, Dec. 1995, doi: 10.1016/0921-5093(95)09953-0.

[62]   Y. P. Raizer, *Gas Discharge Physics*, 1st ed. Springer Berlin Heidelberg, 1991.

[63]   A. Fridman and L. A. Kennedy, *Plasma Physics and Engineering*. CRC Press, 2011.

[64]   E. M. Bazelyan and Y. P. Raizer, *Spark Discharge*. Routledge, 2017.

[65]   M. F. Bragança, G. R. Ribeiro, P. A. R. Rosa, and P. A. F. Martins, "Prototype Machine for Micro-EDM," in *Nontraditional Machining Processes*, London: Springer London, 2013, pp. 153–176.

[66]   S. Nijdam, E. van Veldhuizen, P. Bruggeman, and U. Ebert, "An Introduction to Nonequilibrium Plasmas at Atmospheric Pressure," in *Plasma Chemistry and Catalysis in Gases and Liquids*, Wiley, 2012, pp. 1–44.

[67]   M. Janda, V. Martišovitš, and Z. Machala, "Transient spark: a dc-driven repetitively pulsed discharge and its control by electric circuit parameters," *Plasma Sources Sci. Technol.*, vol. 20, no. 3, Jun. 2011, doi: 10.1088/0963-0252/20/3/035015.

[68]   P. W. J. M. Boumans and F. J. De Boer, "Studies of flame and plasma torch emission for simultaneous multi-element analysis—I," *Spectrochim. Acta Part B At. Spectrosc.*, vol. 27, no. 9, Sep. 1972, doi: 10.1016/0584-8547(72)80038-7.

[69]   G. A. Hemsalech, de Watterville, and M. C. C. R. Herb, *Comptes Rendus Hebdomadaires des Seances de l'Acaedmie des Sciences*, vol. 144. Seance Adacemy Sci., 1907.

[70]   A. L. Yergey, B. L. Bentz, and P. Jane Gale, "The Development of Thermal, Spark Source, and Glow Discharge Ionization," in *The Encyclopedia of Mass Spectrometry*, Elsevier, 2016, pp. 83–86.

[71]   J. Feng, K. Lee, and M. Choi, "Patterned 3D Nanostructure Arrays from Charged Aerosols," in *Spark Ablation*, Jenny Stanford Publishing, 2019, pp. 273–300.

[72]   V. V. Ivanov *et al.*, "High-efficiency synthesis of nanoparticles in a repetitive multigap spark discharge generator," *Tech. Phys. Lett.*, vol. 42, no. 8, Aug. 2016, doi: 10.1134/S106378501608023X.

[73]   B. Ulejczyk, K. Krawczyk, M. Mlotek, L. Nogal, P. Jozwik, and Z. Bojar, "Steam reforming of ethanol in spark discharge generated between electrodes made from a Ni<inf>3</inf>Al alloy," in *2017 International Conference on Optimization of Electrical and Electronic Equipment (OPTIM) & 2017 Intl Aegean Conference on Electrical Machines and Power Electronics (ACEMP)*, May 2017, pp. 1063–1068, doi: 10.1109/OPTIM.2017.7975112.

[74]   K. Han *et al.*, "A study of pin-to-plate type spark discharge generator for producing unagglomerated nanoaerosols," *J. Aerosol Sci.*, vol. 52, Oct. 2012, doi: 10.1016/j.jaerosci.2012.05.002.

[75]   S. Chae, D. Lee, M.-C. Kim, D. S. Kim, and M. Choi, "Wire-in-Hole-Type Spark Discharge Generator for Long-Time Consistent Generation of Unagglomerated Nanoparticles," *Aerosol Sci. Technol.*, vol. 49, no. 7, Jul. 2015, doi: 10.1080/02786826.2015.1045444.

[76] Fasmatech, "Spark Discharge Generator, Theoretical modelling and test performance," 2014.

[77] J. Va'vra, J. A. Maly, and P. M. Va'vra, "Soft X-ray production in spark discharges in hydrogen, nitrogen, air, argon and xenon gases," *Nucl. Instruments Methods Phys. Res. Sect. A Accel. Spectrometers, Detect. Assoc. Equip.*, vol. 418, no. 2–3, Dec. 1998, doi: 10.1016/S0168-9002(98)00926-7.

[78] E. Sher, J. Ben-Yaish, and T. Kravchik, "On the Birth of Spark Channels," in *Combustion and Flame*, vol. 89, 1992, pp. 186–194.

[79] A. Schmidt-Ott, U. Baltensperger, H. . Gäggeler, and D. . Jost, "Scaling behaviour of physical parameters describing agglomerates," *J. Aerosol Sci.*, vol. 21, no. 6, pp. 711–717, Jan. 1990, doi: 10.1016/0021-8502(90)90037-X.

[80] S. K. Friedlander, *Smoke, Dust, and Haze: Fundamentals of Aerosol Dynamics*. New York: Oxford University Press, 2000.

[81] C. Van Gulijk, J. C. M. Marijnissen, M. Makkee, J. A. Moulijn, and A. Schmidt-Ott, "Measuring diesel soot with a scanning mobility particle sizer and an electrical low-pressure impactor: performance assessment with a model for fractal-like agglomerates," *J. Aerosol Sci.*, vol. 35, no. 5, pp. 633–655, May 2004, doi: 10.1016/j.jaerosci.2003.11.004.

[82] V. Vons, "Spark Discharge Generated Nanoparticles for Hydrogen Storage Applications," 2010.

[83] K. Nakaso, M. Shimada, K. Okuyama, and K. Deppert, "Evaluation of the change in the morphology of gold nanoparticles during sintering," *J. Aerosol Sci.*, vol. 33, no. 7, pp. 1061–1074, Jul. 2002, doi: 10.1016/S0021-8502(02)00058-7.

[84] "SMPS Model 3936 TSI."

[85] Y. Zhu, W. C. Hinds, S. Kim, and C. Sioutas, "Concentration and Size Distribution of Ultrafine Particles Near a Major Highway," *J. Air Waste Manage. Assoc.*, vol. 52, no. 9, Sep. 2002, doi: 10.1080/10473289.2002.10470842.

[86] Fuchs, "The mechanics of aerosols. By N. A. Fuchs. Translated by R. E. Daisley and Marina Fuchs; Edited by C. N. Davies. London (Pergamon Press), 1964. Pp. xiv, 408; 82 Figures; 40 Tables. £6," *Q. J. R. Meteorol. Soc.*, vol. 91, no. 388, Apr. 1965, doi: 10.1002/qj.49709138822.

[87] A. Wiedensohler, "An approximation of the bipolar charge distribution for particles in the submicron size range," *J. Aerosol Sci.*, vol. 19, no. 3, Jun. 1988, doi: 10.1016/0021-8502(88)90278-9.

[88] R. Friedlander, E. Jarosch, J. Urban, C. Volkwein, and T. Sommer, "A regulatory link between ER-associated protein degradation and the unfolded-protein response.," *Nat. Cell Biol.*, vol. 2, no. 7, Jul. 2000, doi: 10.1038/35017001.

[89] W. Haaf, "Accurate measurements of aerosol size distribution—I. Theory of a plate condenser for bipolar mobility analysis," *J. Aerosol Sci.*, vol. 11, no. 2, Jan. 1980, doi: 10.1016/0021-8502(80)90034-8.

[90] K.-H. Ahn and B. Y. H. Liu, "Particle activation and droplet growth processes in condensation nucleus counter—I. Theoretical background," *J. Aerosol Sci.*, vol. 21, no. 2, Jan. 1990, doi: 10.1016/0021-8502(90)90008-L.

[91] FEI Company, *The Quanta Inspect SEM*, 1st ed. 2003.

[92] A. Nanakoudis, "SEM: Types of Electrons and the Information They Provide," *ThermoFisher Scientific*, Nov. 21, 2019. .

[93] A. Sandborg, *Energy Dispersive X-Ray Spectrometry -- EDS Instrumentation & SIgnal Detection*. EDAX INTERNATIONAL, INC., 2011.

[94] E. Benis, *Atomic Physics, Notes*. Ioannina, 2013.

[95] AMETEK, "Understanding Characteristic X-Rays." .

[96] W. E. Smith and G. Dent, *Modern Raman Spectroscopy - A Practical Approach*, vol. 2. West Sussex: John Wiley & Sons, 2005.

[97] S. Wartewig, *IR and Raman Spectroscopy: Fundamental Processing*. 2006.

[98] D. Long, *The Raman Effect: A Unified Treatment of the Theory of Raman Scattering by Molecules*. West Sussex: John Wiley & Sons, 2002.

[99] S. L. Trachanas, *Quantum Mechanics II*. 2008.

[100] M. B. Fenn, P. Xanthopoulos, G. Pyrgiotakis, S. R. Grobmyer, P. M. Pardalos, and L. L. Hench, "Raman Spectroscopy for Clinical Oncology," *Adv. Opt. Technol.*, vol. 2011, Oct. 2011, doi: 10.1155/2011/213783.

[101] L. Lan, Y. Gao, X. Fan, M. Li, Q. Hao, and T. Qiu, "The origin of ultrasensitive SERS sensing beyond plasmonics," *Front. Phys.*, vol. 16, no. 4, p. 43300, Aug. 2021, doi: 10.1007/s11467-021-1047-z.

[102] J.-F. Masson, "Portable and field-deployed surface plasmon resonance and plasmonic sensors," *Analyst*, vol. 145, no. 11, pp. 3776–3800, 2020, doi: 10.1039/D0AN00316F.

[103] A. Douzenis, "Production and Characterization of Nanoparticles generated by Spark Discharge," 2021.

[104] C. Karakasis, "Nanoparticle production and characterization of nanoparticles produced by Spark Discharge Generator," 2019.

[105] D. Megyeri, A. Kohut, and Z. Geretovszky, "Effect of flow geometry on the nanoparticle output of a spark discharge generator," *J. Aerosol Sci.*, vol. 154, p. 105758, May 2021, doi: 10.1016/j.jaerosci.2021.105758.

[106] K. Giannakopoulos *et al.*, "Copper Oxide and Copper nanoparticles produced in aerosols: Structural and optical characterization, evaluation of activity against bacteria and the SARS-CoV-2 on face masks," 2022.

[107] K. E. J. Lehtinen and M. R. Zachariah, "Energy accumulation in nanoparticle collision and coalescence processes," *J. Aerosol Sci.*, vol. 33, no. 2, pp. 357–368, Feb. 2002, doi: 10.1016/S0021-8502(01)00177-X.

[108] M. S. Naidu and V. Kamaraju, *High Voltage Engineering*, 2nd ed. Mcgaw Hill, 1995.

[109] C. M. Cundall and J. D. Craggs, *Electrode Vapor Jets in Spark Discharges*, vol. 7. Spectrochimica Acta, 1955.

[110] M. A. Barrufet, M. R. Patel, and P. T. Eubank, *Novel Computations of a Moving Boundary Heat Conduction Problem Applied to EDM Technology*, 8th ed., vol. 15. Computers Chem. Engng, 1991.

[111] M. I. Gini *et al.*, "Characterization of carbon fractal-like aggregates by size distribution measurements and theoretical calculations," *Aerosol Sci. Technol.*, vol. 50, no. 2, pp. 133–147, Feb. 2016, doi: 10.1080/02786826.2015.1134763.

[112] F. A. Soldera, F. T. Mucklich, K. Hrastnik, and T. Kaiser, "Description of the Discharge Process in Spark Plugs and its Correlation With the Electrode Erosion Patterns," *IEEE Trans. Veh. Technol.*, vol. 53, no. 4, pp. 1257–1265, Jul. 2004, doi: 10.1109/TVT.2004.830977.

[113] F. Llewellyn Jones, *Electrode Erosion by Spark Discharges*, vol. 1. British Journal of Applied Physics, 1950, https://doi.org/10.1088/0508-3443/1/3/302.

[114] T. Němec, J. Šonský, J. Gruber, E. de Prado, J. Kupčík, and M. Klementová, "Platinum and platinum oxide nanoparticles generated by unipolar spark discharge," *J. Aerosol Sci.*, vol. 141, p. 105502, Mar. 2020, doi: 10.1016/j.jaerosci.2019.105502.

[115] R. N. Szenete, R. J. Munz, and G. Drouet, "Copper-Niobium and Copper-Tungsten Composites as Plasma Torch Cathodes," *J. Phys. D. Appl. Phys.*, vol. 27, pp. 1443–1447, 1994.

[116] S. A. B. Sharifuddin, S. B. Ismail, I. Abdullah, I. Mohamad, and J. Shaikh Mohammed, "Antibacterial evaluation of activated carbon cloth with Ag $^+$ impregnated with ZnO nanoparticles," *Res. J. Text. Appar.*, vol. 23, no. 3, pp. 232–243, Sep. 2019, doi: 10.1108/RJTA-09-2018-0056.

[117] N. Kostoglou *et al.*, "Nanoporous activated carbon cloth as a versatile material for hydrogen adsorption, selective gas separation and electrochemical energy storage," *Nano Energy*, vol. 40, pp. 49–64, Oct. 2017, doi: 10.1016/j.nanoen.2017.07.056.

[118] I. Rossetti, G. Ramis, A. Gallo, and A. Di Michele, "Hydrogen storage over metal-doped activated carbon," *Int. J. Hydrogen Energy*, vol. 40, no. 24, pp. 7609–7616, Jun. 2015, doi: 10.1016/j.ijhydene.2015.04.064.

[119] N. Kostoglou *et al.*, "Effect of Pt nanoparticle decoration on the H2 storage performance of plasma-derived nanoporous graphene," *Carbon N. Y.*, vol. 171, pp. 294–305, Jan. 2021, doi: 10.1016/j.carbon.2020.08.061.

[120] W. M. Daoush, T. S. Albogmy, M. A. Khamis, and F. Inam, "Syntheses and Step-by-Step Morphological Analysis of Nano-Copper-Decorated Carbon Long Fibers for Aerospace Structural Applications," *Crystals*, vol. 10, no. 12, p. 1090, Nov. 2020, doi: 10.3390/cryst10121090.

[121] G. Seo *et al.*, "Rapid Detection of COVID-19 Causative Virus (SARS-CoV-2) in Human Nasopharyngeal Swab Specimens Using Field-Effect Transistor-Based Biosensor," *ACS Nano*, vol. 14, no. 4, Apr. 2020, doi: 10.1021/acsnano.0c02823.

[122] L. Jiang *et al.*, "Preparation of antimicrobial activated carbon fiber by loading with silver nanoparticles," *Colloids Surfaces A Physicochem. Eng. Asp.*, vol. 633, p. 127868, Jan. 2022, doi: 10.1016/j.colsurfa.2021.127868.

[123] C. Tang, W. Sun, and W. Yan, "Green and facile fabrication of silver nanoparticles loaded activated carbon fibers with long-lasting antibacterial activity," *RSC Adv.*, vol. 4, no. 2, pp. 523–530, 2014, doi: 10.1039/C3RA44799E.

[124] M. Rezaei, S. H. Tabaian, and D. F. Haghshenas, "The Role of Electrodeposited Pd Catalyst Loading on the Mechanisms of Formic Acid Electro-Oxidation," *Electrocatalysis*, vol. 5, no. 2, pp. 193–203, Apr. 2014, doi: 10.1007/s12678-013-0181-y.

[125] F. A. López, M. I. Martín, F. J. Alguacil, J. M. Rincón, T. A. Centeno, and M. Romero, "Thermolysis of fibreglass polyester composite and reutilisation of the glass fibre residue to obtain a glass–ceramic material," *J. Anal. Appl. Pyrolysis*, vol. 93, pp. 104–112, Jan. 2012, doi: 10.1016/j.jaap.2011.10.003.

[126] M. Etcheverry and S. E. Barbosa, "Glass Fiber Reinforced Polypropylene Mechanical Properties Enhancement by Adhesion Improvement," *Materials (Basel).*, vol. 5, no. 12, pp. 1084–1113, Jun. 2012, doi: 10.3390/ma5061084.

[127] C. Xu, G. Liu, H. Chen, R. Zhou, and Y. Liu, "Fabrication of conductive copper-coated glass fibers through electroless plating process," *J. Mater. Sci. Mater. Electron.*, vol. 25, no. 6, pp. 2611–2617, Jun. 2014, doi: 10.1007/s10854-014-1919-x.

[128] H. Chen, Y. Tai, and C. Xu, "Fabrication of copper-coated glass fabric composites through electroless plating process," *J. Mater. Sci. Mater. Electron.*, vol. 28, no. 1, pp. 798–802, Jan. 2017, doi: 10.1007/s10854-016-5592-0.

[129] S. Zeng, M. Shen, S. Chen, L. Yang, F. Lu, and Y. Xue, "Mechanical and thermal properties of carbon nanotube- and graphene-glass fiber fabric-reinforced epoxy composites: A comparative study," *Text. Res. J.*, vol. 89, no. 12, pp. 2353–2363, Jun. 2019, doi: 10.1177/0040517518792750.

[130] A. Gupta, V. Mishra, and R. Srivastava, "Zinc oxide nanoparticles decorated fluorescent and antibacterial glass fiber pre-filter paper," *Nano Express*, vol. 1, no. 1, p. 010048, Jun. 2020, doi: 10.1088/2632-959X/ab976d.

[131] S. Thipperudrappa, A. U. Kini, and A. Hiremath, "An experimental study to evaluate the effect of TiO $_2$ nanoparticles on the strength and stability of unidirectional glass fiber reinforced epoxy composites," *Mater. Res. Express*, vol. 6, no. 11, p. 115347, Nov. 2019, doi: 10.1088/2053-1591/ab5031.

[132] C. L. Haynes, A. D. McFarland, and R. P. Van Duyne, "Surface-Enhanced Raman Spectroscopy," *Anal. Chem.*, vol. 77, no. 17, pp. 338 A-346 A, Sep. 2005, doi: 10.1021/ac053456d.

[133] G. P. Szekeres and J. Kneipp, "SERS Probing of Proteins in Gold Nanoparticle Agglomerates," *Front. Chem.*, vol. 7, Jan. 2019, doi: 10.3389/fchem.2019.00030.

[134] G. P. Szekeres, M. Montes-Bayón, J. Bettmer, and J. Kneipp, "Fragmentation of Proteins in the Corona of Gold Nanoparticles As Observed in Live Cell Surface-Enhanced Raman Scattering," *Anal. Chem.*, vol. 92, no. 12, pp. 8553–8560, Jun. 2020, doi: 10.1021/acs.analchem.0c01404.

[135] L. Fabris, "Gold-based SERS tags for biomedical imaging," *J. Opt.*, vol. 17, no. 11, p. 114002, Nov. 2015, doi: 10.1088/2040-8978/17/11/114002.

[136] A. Kohut *et al.*, "Facile and versatile substrate fabrication for surface enhanced Raman spectroscopy using spark discharge generation of Au/Ag nanoparticles," *Appl. Surf. Sci.*, vol. 531, Nov. 2020, doi: 10.1016/j.apsusc.2020.147268.

[137] V. Devendra, "Effectiveness of Masks: Fast Answers with Automated SEM Analysis," *www.nanoscience.com*. .

[138]   "SARS-COV-2 Dashboard by the Center for Systems Science and Engineering (CSSE) at Johns Hopkins University (JHU)," *https://coronavirus.jhu.edu/map.html*, Feb. 20, 2021. .

[139]   J. Phua *et al.*, "Intensive care management of coronavirus disease 2019 (COVID-19): challenges and recommendations," *Lancet Respir. Med.*, vol. 8, no. 5, pp. 506–517, May 2020, doi: 10.1016/S2213-2600(20)30161-2.

[140]   J. Wang and G. Du, "COVID-19 may transmit through aerosol," *Irish J. Med. Sci. (1971 -)*, vol. 189, no. 4, pp. 1143–1144, Nov. 2020, doi: 10.1007/s11845-020-02218-2.

[141]   M. L. Ranney, V. Griffeth, and A. K. Jha, "Critical Supply Shortages — The Need for Ventilators and Personal Protective Equipment during the Covid-19 Pandemic," *N. Engl. J. Med.*, vol. 382, no. 18, p. e41, Apr. 2020, doi: 10.1056/NEJMp2006141.

[142]   J. Wang, M. Zhou, and F. Liu, "Reasons for healthcare workers becoming infected with novel coronavirus disease 2019 (COVID-19) in China," *J. Hosp. Infect.*, vol. 105, no. 1, pp. 100–101, May 2020, doi: 10.1016/j.jhin.2020.03.002.

[143]   D. E. McMahon, G. A. Peters, L. C. Ivers, and E. E. Freeman, "Global resource shortages during COVID-19: Bad news for low-income countries," *PLoS Negl. Trop. Dis.*, vol. 14, no. 7, p. e0008412, Jul. 2020, doi: 10.1371/journal.pntd.0008412.

[144]   C. D. Zangmeister, J. G. Radney, E. P. Vicenzi, and J. L. Weaver, "Filtration Efficiencies of Nanoscale Aerosol by Cloth Mask Materials Used to Slow the Spread of SARS-CoV-2," *ACS Nano*, vol. 14, no. 7, pp. 9188–9200, Jul. 2020, doi: 10.1021/acsnano.0c05025.

[145]   J. Zhou, Z. Hu, F. Zabihi, Z. Chen, and M. Zhu, "Progress and Perspective of Antiviral Protective Material," *Adv. Fiber Mater.*, vol. 2, no. 3, pp. 123–139, Jun. 2020, doi: 10.1007/s42765-020-00047-7.

[146]   C. Balagna, S. Perero, E. Percivalle, E. V. Nepita, and M. Ferraris, "Virucidal effect against coronavirus SARS-CoV-2 of a silver nanocluster/silica composite sputtered coating," *Open Ceram.*, vol. 1, p. 100006, May 2020, doi: 10.1016/j.oceram.2020.100006.

[147]   M. Minoshima *et al.*, "Comparison of the antiviral effect of solid-state copper and silver compounds," *J. Hazard. Mater.*, vol. 312, pp. 1–7, Jul. 2016, doi: 10.1016/j.jhazmat.2016.03.023.

[148]   D. Sachan, "COVID-19 Pandemic Has Spurred Materials Researchers to Develop Antiviral Masks," *ACS Cent. Sci.*, vol. 6, no. 9, pp. 1469–1472, Sep. 2020, doi: 10.1021/acscentsci.0c01172.

[149]   G. Borkow, S. S. Zhou, T. Page, and J. Gabbay, "A Novel Anti-Influenza Copper Oxide Containing Respiratory Face Mask," *PLoS One*, vol. 5, no. 6, p. e11295, Jun. 2010, doi: 10.1371/journal.pone.0011295.

[150]   S. Jung *et al.*, "Copper-Coated Polypropylene Filter Face Mask with SARS-CoV-2 Antiviral Ability," *Polymers (Basel).*, vol. 13, no. 9, p. 1367, Apr. 2021, doi: 10.3390/polym13091367.

[151]   C. Hewawaduge, A. Senevirathne, V. Jawalagatti, J. W. Kim, and J. H. Lee, "Copper-impregnated three-layer mask efficiently inactivates SARS-CoV2," *Environ. Res.*, vol. 196, p. 110947, May 2021, doi: 10.1016/j.envres.2021.110947.

[152]   M. M. H. Babu, "Layer by Layer (LbL) self-assembly methods," 2018.

[153]   D.-L. Liu, "Particle Deposition onto Enclosure Surfaces," in *Developments in Surface*

Contamination and Cleaning, Elsevier, 2010, pp. 1–56.

[154] "Escherichia coli," *https://www.micropia.nl*. .

APPENDIX A

Effect of SDG Control Parameters in NP Synthesis

In the following experiments, by changing the control parameters (electrode distance, input voltage and carrier gas flow), results were obtained from the concentrations produced for each electrode (copper, gold, platinum and palladium). The following diagrams result from the normalization of the conditions in general with a maximum of 1.0 as the best condition for the respective material (the actual size orders of the generated particle concentrations are not taken into account)

By changing the distance between the electrodes Figure 67, it is observed that each material behaves differently. In the case of gold and palladium, as the distance between the electrodes grows, the spark becomes more efficient and larger particles are produced on average with higher concentrations. In contrast, copper and gold prefer short distances, as the larger the distance, the weaker the spark becomes, the fewer and smaller nanoparticles are produced.
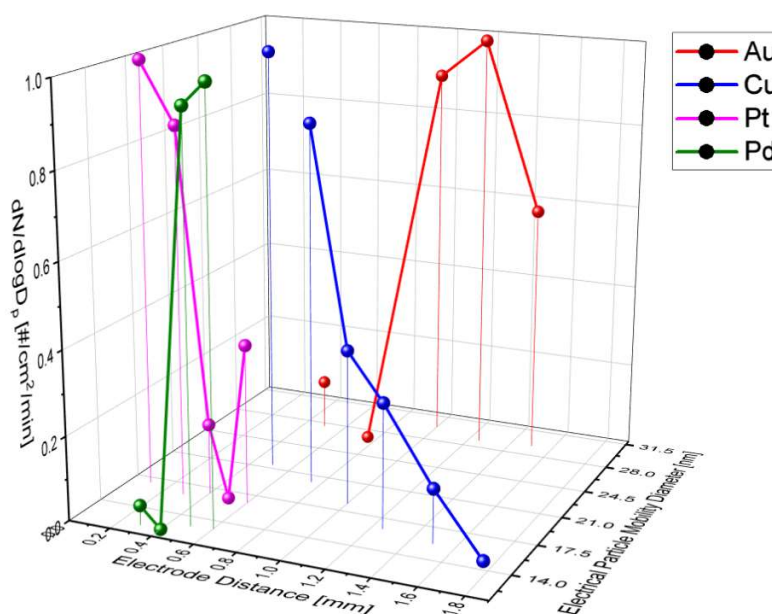

Figure 67. Normalized electrode distance effect on diameter and concentration of produced NPs.

In the case of voltage (Figure 68), it appears that in all four cases the higher the particle concentrations, the higher the particle concentrations produced. However, what is observed is that in the case of gold and copper, with the former predominating, with the increase of the potential, the size of the produced

particles also increases. On the contrary, in the case of platinum and palladium, the sizes seem to remain relatively constant and not be affected by the change.
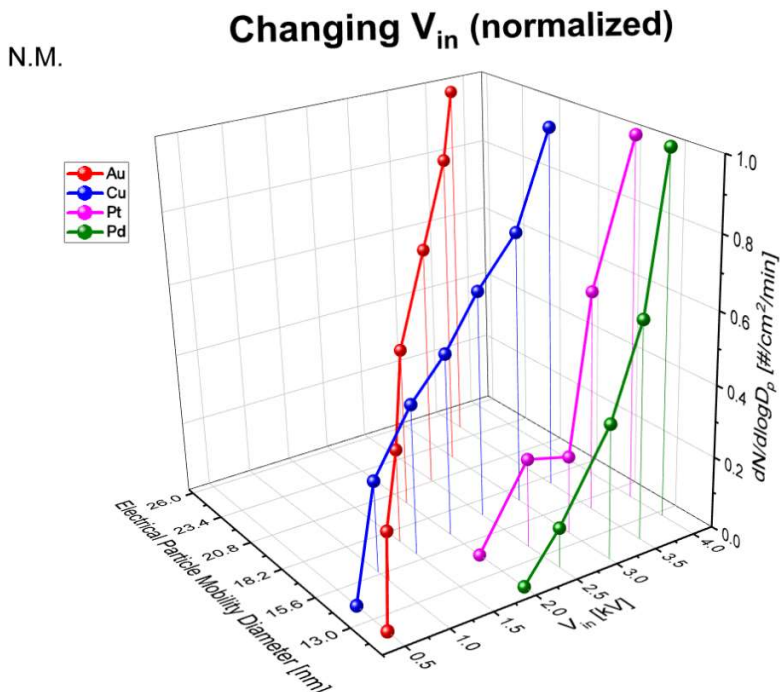

Figure 68. Normalized V$_{in}$ effect on diameter and concentration of produced NPs.

Finally, by changing the flow of nitrogen entering the experiment, it is observed that for each material the behavior follows its own path for small flows (Figure 69). It is observed, however, that for 4 liters per minute all the materials have maximum efficiency which is followed by a sharp drop. The fall logically happens because the carrier gas flow is so large that "spoils" the spark and they do not manage to form the nuclei of the nanoparticles properly.
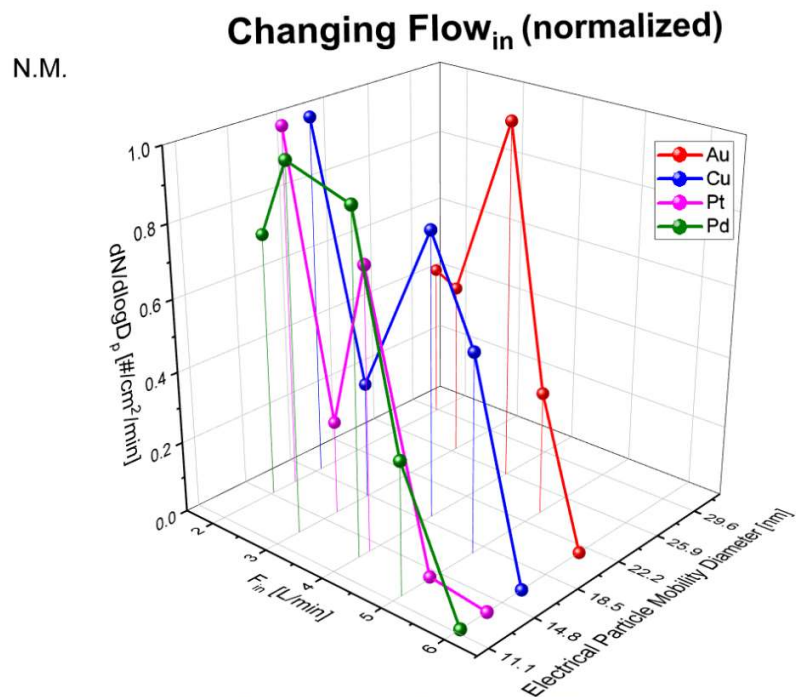
Figure 69. Normalized F_{in} effect on diameter and concentration of the produced NPs.

APPENDIX B

Table 4. Effect of charging current I in particle production (bolded columns).

	Cu						
V_d (V)	**1450**	3200	3700	3800	3850	3900	4000
f (Hz)	**352**	96	64	64	32	28	12
I (mA)	**0.990176**	0.595968	0.459392	0.471808	0.239008	0.211848	0.09312

	Au					
V_d (V)	2400	2680	3200	3850	4075	**4250**
f (Hz)	128	96	64	48	40	**32**
I (mA)	0.595968	0.499123	0.397312	0.358512	0.31622	**0.26384**

	Pd			
V_d (V)	2000	2800	3200	**3700**
f (Hz)	250	83	50	**40**
I (mA)	0.97	0.450856	0.3104	**0.28712**

	Pt				
V_d (V)	**2000**	2400	2800	3200	3800
f (Hz)	**125**	100	83.3	62.5	33.3
I (mA)	**0.485**	0.4656	0.452486	0.388	0.245488

APPENDIX C

Table 5. Characteristics of various electrode materials and their effect in mass production.

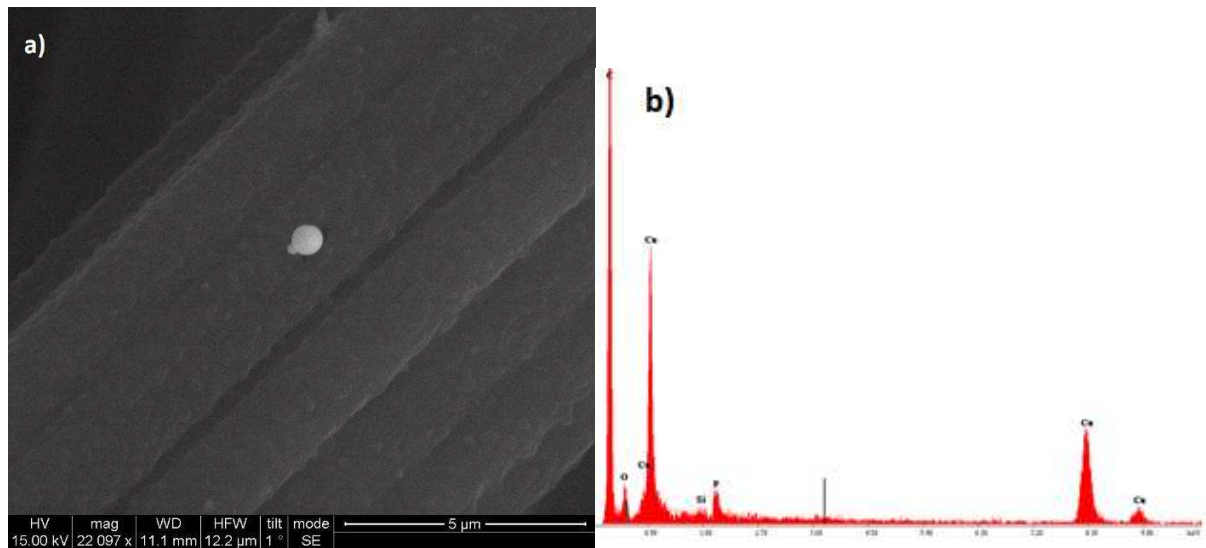| Material	T_b (K)	T_m (K)	c_{ps} ($Jg^{-1}k^{-1}$)	ΔH_m (Jg^{-1})	ΔH_v (Jg^{-1})	m_{calc} (mole/ spark)	m_{meas} (mole/ spark)
CuO	2840	1356.6	0.386	207	5069	1.75876E-06	4.45189E-6
Au	3130	1337.58	0.126	67	1578	5.49387E-06	0.00812
Pd	3240	1825	0.24	165.4135	3355.263	2.6063E-06	1.70019E-6
Pt	4100	2042.1	0.13	100.4665	2614.178	3.44398E-06	9.03741E-7

APPENDIX D

Figure 70. a) SE SEM image of type iii Cu/CuO NP deposited in *AI* area on non woven ACC (SDNM_8) and b) EDS analysis that verifies its Cu/CuO nature.
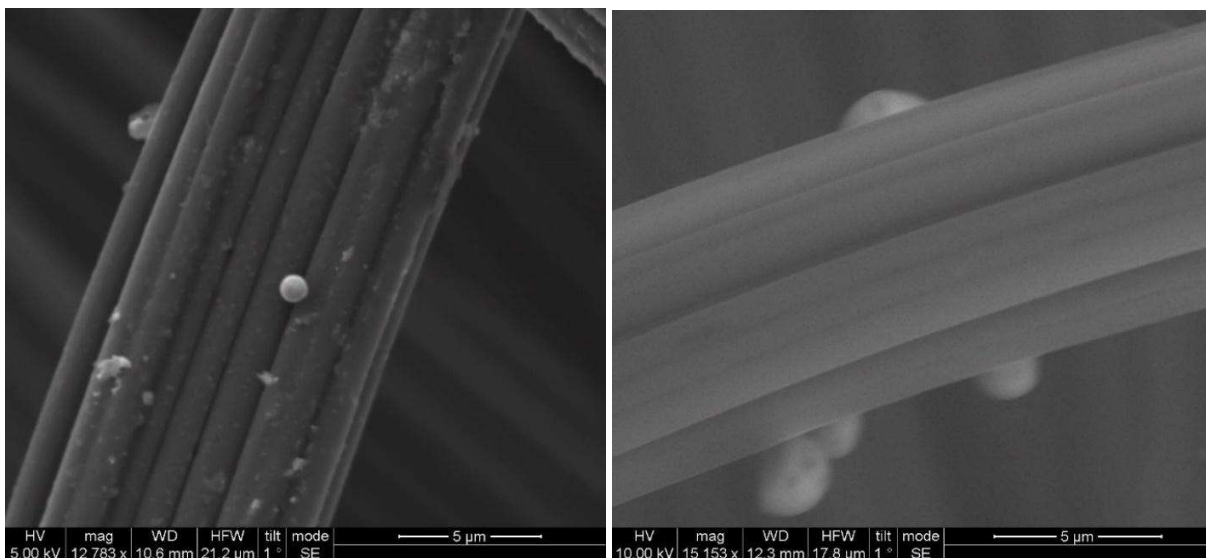

Figure 71. SE SEM image of type iii spherical Pd NPs deposited on non-woven ACC (SDNM_44).

APPENDIX E

Name	Material	Electrodes	F_{in} (L/min)	SRR	V_{dis} (kV)	Time
SDNM_3	BSF	Cu	3	352	1.3	2h
SDNM_8	Non-woven ACC	Cu	5	352	1.3	2h
SDNM_9	BSF	Au	3	128	2.3	1h
SDNM_19	BSF	Au	3	128	2.3	1h
SDNM_26	BSF	Au	2	128	2.6	1h
SDNM_30	BSF	Au	2	112	2.8	20min
SDNM_43	Non-woven ACC	Pd	3	50	3.8	40 min/ side
SDNM_44	Non-woven ACC	Pd	3	55	3.8	20 min/side
Mask_5	PP surgical mask	Cu	5	112	2.8	21h
Mask_6	PP surgical mask	Cu	5	112	2.8	9.5h
Mask_8	PP surgical mask	Cu	3	128	2.6	4.5h
Mask_10	PP surgical mask	Cu	3	80	4	13h